Review of Graphene for the Generation, Manipulation, and Detection of Electromagnetic Fields from Microwave to Terahertz

David A Katzmarek[1,2], Aiswarya Pradeepkumar[1,2], Richard W Ziolkowski[1,3], Francesca Iacopi[1,2,4]
[1] Faculty of Engineering and IT, University of Technology Sydney, Sydney, Australia
[2] Australian Research Council Centre of Excellence on Transformative Meta-Optical Systems, University of Technology Sydney, Sydney, Australia
[3] Department of Electrical and Computer Engineering, University of Arizona, Tucson, USA
[4]ARC Centre of Excellence in Future Low-Energy Electronics Technologies, Australia

Email:
francesca.iacopi@uts.edu.au

Received xxxxxx
Accepted for publication xxxxxx
Published xxxxxx

Abstract

Graphene has attracted considerable attention ever since the discovery of its unprecedented properties, including its extraordinary and tunable electronic and optical properties. In particular, applications within the microwave to terahertz frequency spectrum can benefit from graphene's high electrical conductivity, mechanical flexibility and robustness, transparency, support of surface-plasmon-polaritons, and the possibility of dynamic tunability with direct current to light sources.
This review aims to provide an in-depth analysis of current trends, challenges, and prospects within the research areas of generating, manipulating, and detecting electromagnetic fields using graphene-based devices that operate from microwave to terahertz frequencies. The properties of and models describing graphene are reviewed first, notably those of importance to electromagnetic applications. State-of-the-art graphene-based antennas, such as resonant and leaky-wave antennas, are discussed next. A critical evaluation of the performance and limitations within each particular technology is given. Graphene-based metasurfaces and devices used to manipulate electromagnetic fields, e.g., wavefront engineering, are then examined. Lastly, the state-of-the-art of detecting electromagnetic fields using graphene-based devices is discussed.

Keywords: Antennas, Graphene, Metamaterials, Microwaves, Photodetectors, Terahertz

1. Introduction

Novoselov et al. [1] discovered that electric fields could modulate the electrical conductivity in ultrathin carbon films in 2004. Using the rather simple scotch tape method, they isolated a two-dimensional (2D) layer of carbon from a graphite block, now commonly known as graphene. It was previously considered impossible to isolate a single crystalline layer of carbon atoms because scientists believed it would roll up instead of remaining in the planar form [2]. Graphene was the first documented 2D material, forming naturally thanks to the carbon sp^2 hybridization. Its discovery has triggered a substantial amount of research and also led to the discovery of

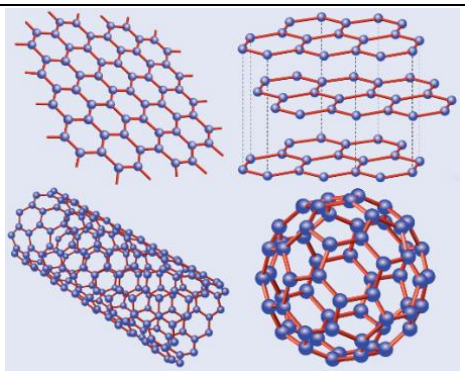

Figure 1. Carbon allotropes. Reprinted with permission from [3]. Copyright 2009 by the American Physical Society.

other 2D materials. It has sparked hopes for a revolution in electronics.

Graphene is a semi-metal, and graphene-based devices are generally not aimed to replace the workhorses of silicon (Si) technology, such as the complementary metal-oxide-semiconductor (CMOS) transistors, as graphene lacks a natural bandgap (BG). Nevertheless, graphene possesses properties not accessible with silicon and holds great promise for electromagnetic (EM) applications- for instance, in the microwave and terahertz (THz) frequency ranges. Metals and semiconductors have been so far the dominant materials employed for generating, manipulating, and detecting EM fields at those frequencies. However, graphene's high electron mobility, dynamic tunability, and the support of surface plasma polaritons (SPPs) make it an ideal candidate to enhance or even replace established technologies. This paper aims to give an overview of the current progress of graphene antennas used to generate EM waves; using graphene to facilitate metasurface-based devices, e.g., for wavefront engineering; and realizing graphene-based EM absorbers and detectors within the microwave and THz frequency ranges.

In this review, Section 2 introduces graphene and its properties, including a brief overview of synthesis procedures with an emphasis on integration capabilities. Section 3 covers the generation, manipulation, and detection of EM fields using graphene devices. Section 3.1 gives an overview of graphene-based antenna applications in the microwave and THz range. There is a substantial amount of experimentally demonstrated flexible, transparent, and integrated antennas in the microwave frequency range. On the other hand, antennas reported in the THz range are mainly based on numerical simulations of resonant or traveling-wave antennas and the dynamic tunability of their properties. Section 3.2 focuses on metasurface-based beamforming applications. Two main structures are reported, reflectarrays and transmitarrays. Their function is briefly explained, and advances enabled by graphene devices are analyzed. Section 3.3 provides an overview of graphene-based absorbers. It will be described how their responses can be dynamically reconfigured in dedicated frequency ranges. Examples of total absorption are given. Section 3.4 focuses on graphene-based EM detection architectures. Their principal operating mechanisms are explained and evaluated. In particular, THz detectors based on graphene field-effect transistor (GFET) will be emphasized since they form an important area of research in the development of measuring EM fields. Section 4 concludes the review and gives an outlook on the future of graphene-based devices in the microwave and THz frequency ranges.

2. Unique Properties of Graphene

Graphene is a 2D allotrope of carbon [2]. It can be seen as the basis for the other 2D allotropes of carbon, including graphite, which is a stack of many graphene layers (typically more than 10 [4]), carbon nanotubes (CNTs, rolled-up sheets of graphene with different chirality), and fullerene molecules (sphere-like structures of wrapped graphene, or C_n) [3], see figure 1.

The 2D nature of carbon is enabled by sp^2 hybridized atoms naturally forming a planar, honeycomb/hexagonal lattice structure. Each atom forms three σ-bonds with neighbouring carbon atoms. They are separated by 1.42 Å [5] and are responsible for the strength of the lattice structure [3]. These orbitals form the completely filled valence band of graphene. P-orbitals are perpendicular to the lattice and form covalent bonds (π-bonds) with neighboring atoms to create a so-called π-band [3]. Pristine graphene has one electron per carbon atom in the π-band, resulting in a half-filled band [3]. These electrons are highly mobile and are responsible for graphene's unique electrical properties.

2.1 Tight Binding Model

The carbon atoms in graphene are arranged in a hexagonal structure, but its lattice can also be seen as triangular, as illustrated in figure 2(a), with the lattice vectors [3]

$$a_1 = \frac{a}{2}(3, \sqrt{3}), a_2 = \frac{a}{2}(3, -\sqrt{3}), \quad (1)$$

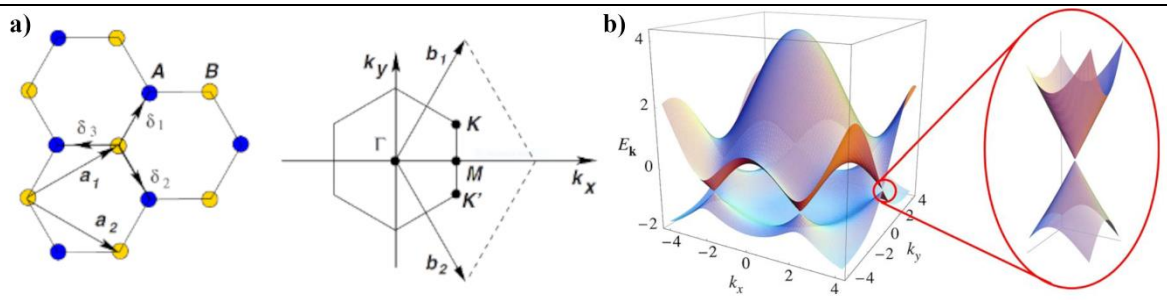

Figure 2. (a) Graphene's hexagonal lattice and its Brillouin zone. (left) Graphene lattice structure which comprises two triangular Bravais lattices, and (right) Brillouin zone with Dirac cones being located at the K and K' points. (b) Electronic dispersion of graphene in a single hexagonal lattice element for $t = 2.7$ eV and $t' = -0.2t$. Reprinted with permission from [3]. Copyright 2009 by the American Physical Society.

and $a \approx 1.42$ Å being the carbon atom separation distance. Accordingly, the reciprocal lattice vectors can be written as [3]

$$b_1 = \frac{2\pi}{3a}(1, \sqrt{3}), b_2 = \frac{2\pi}{3a}(1, -\sqrt{3}). \quad (2)$$

δ_1, δ_2, and δ_3 represent the nearest neighbor vectors and are given by [3]

$$\delta_1 = \frac{a}{2}(1, \sqrt{3}), \delta_2 = \frac{a}{2}(1, -\sqrt{3}), \delta_3 = -a(1,0). \quad (3)$$

The previously discussed Dirac points are positioned at the two K and K' points. They also represent the corners of graphene's Brillouin zone (BZ). Their absolute positions are determined as [3]

$$K = \left(\frac{2\pi}{3a}, \frac{2\pi}{3\sqrt{3}a}\right), K' = \left(\frac{2\pi}{3a}, -\frac{2\pi}{3\sqrt{3}a}\right). \quad (4)$$

Using the tight-binding Hamiltonian for graphene electrons, which considers electron hopping to the nearest and next-nearest-neighbor atoms, Wallace [5] derived the energy bands as [3]

$$E_{\pm}(k) = \pm t\sqrt{3 + f(k)} - t' f(k), \quad (5)$$

$$f(k) = 2\cos(\sqrt{3}k_y a) + 4\cos\left(\frac{\sqrt{3}}{2}k_y a\right)\cos\left(\frac{3}{2}k_x a\right), \quad (6)$$

with k representing a 2D vector from the center of the BZ (see figure 2(a)), t being the nearest-neighbor hopping energy between different sublattices, and t' being the next-nearest-neighbor hopping energy within the same sublattice. Figure 2(b) shows the upper (E_+) and lower (E_-)-band from equation (5) for $t = 2.7$ eV and $t' = -0.2t$. It also visualizes how non-zero values for t' break the electron-hole symmetry [3].

Graphene has a linear energy-momentum diagram with zero bandgap at the Dirac points. Figure 2(b) indicates that its dispersion surfaces form cones, which are often referred to as Dirac cones.

As a result, very high intrinsic carrier mobilities have been demonstrated in graphene. It has been determined to have a theoretical limit of $\sim 2 \times 10^5$ cm^2 V^{-1} s^{-1} [6], for exfoliated and suspended graphene. This value is significantly higher than any metal. The Fermi velocity of graphene is defined as $v_F = 3ta/2$ and has a value of $v_F \cong 1 \times 10^6$ m s^{-1} [3]. Moreover, graphene offers a very high saturation velocity. Dorgan et al. [7] have measured values of $> 3 \times 10^7$ cm s^{-1} for graphene on silicon dioxide (SiO_2). Furthermore, it can withstand significant electrical currents. In fact, a breakdown current density of $> 10^8$ A cm^{-2} has been demonstrated in [1]. These properties make it an outstanding material for electronic and EM applications.

Graphene's electric field effect on carrier concentration was first demonstrated by Novoselov et al. [1]. It characterizes the modulation of the carrier concentration, which leads to a variation of the conductivity of graphene. Their experiment revealed graphene's ambipolar characteristics with electrostatic biasing. Their results showed the charge neutral point (CNP), i.e., biasing voltage at which the conductivity of graphene has a minimum, is shifted towards positive voltages. This is due to the interactions between graphene and the substrate and gate dielectrics and graphene's intrinsic doping. Most manufacturing processes of graphene will result in distinct initial doping. For example, chemical vapor deposition (CVD) graphene is generally p-type, whereas epitaxial graphene (EG) grown on silicon carbide (SiC) is primarily n-doped [8]. Consequently, these graphene samples will have either a hole or electron dominant conduction in their unbiased state. With increasing voltages V$^+$ and decreasing voltages V$^-$ the CNP can be reached, where a mixed hole and electron conduction occurs until the main carrier type finally changes. Ideal graphene has its CNP at $V_g = 0$ V and its conductivity changes symmetrically as the absolute value of biasing increases, as shown in figure 3(a).

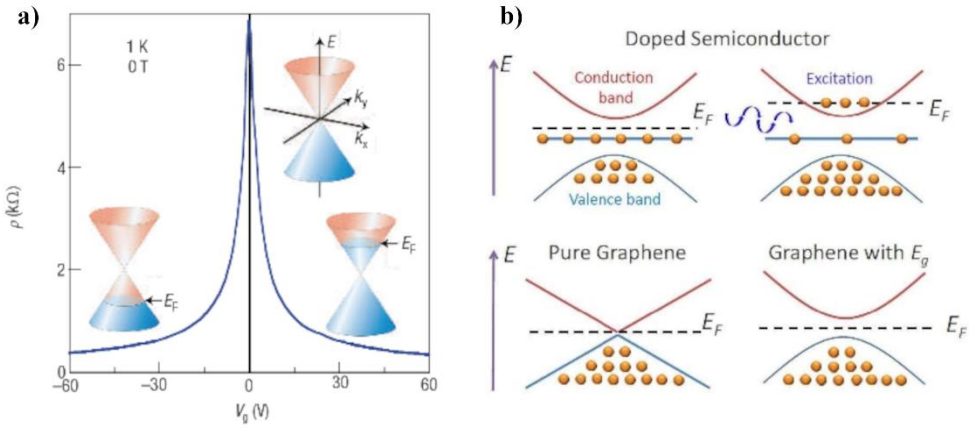

Figure 3. (a) Electrostatic biasing induced electric field effect in single-layer graphene. The graph shows the ambipolar modulation of graphene's resistivity and the Fermi energy change with varying gate voltages. (b) Band structure of graphene for (bottom-left) pristine graphene, (bottom-right) non-ideal graphene with minimal bandgap, (top-left) doped graphene with slightly larger bandgap, and Fermi energy shift, as well as (top-right) doped graphene with electromagnetic biasing. (a) Reprinted by permission from [10]. Copyright 2014 Springer Nature. (b) Reprinted by permission from [9]. Copyright 2007 Springer Nature.

Next to the possibility of EM biasing and graphene's zero BG, the electronic properties of graphene are of high relevance for electronic applications. Like semiconductor applications, graphene can be dynamically tuned using various biasing options and doped to manipulate its material characteristics for optimal adjustment according to the selected application. It should be noted that doping, similar to biasing, will change the Fermi energy E_F. It also introduces a BG within the band structure [9]. Figure 3(b) shows two versions of graphene's band structure. The nonideal one has lost the V-shape of the ideal version and has become parabolic.

2.2 The Conductivity of Graphene

One of graphene's most important properties for its use in electronic and EM applications is its conductivity and tunability. It has therefore been a significant area of research in the early years after graphene's discovery. Knowing the behavior of the conductivity regarding various biasing mechanisms, as well as its temperature and frequency dependence, is crucial for the characterization of graphene and the development of models. These are commonly used in simulations and essential in the research of possible applications.

Graphene is modeled as an infinitesimally thin non-local two-sided sheet whose surface conductivity can be described by a two-dimensional conductivity tensor [11]. In the case of non-local anisotropic graphene, it can be expressed as [11]

$$\bar{\sigma}(\omega, \mu_\mathrm{c}(E_0), \Gamma, T, B_0) = \hat{x}\hat{x}\sigma_{\mathrm{xx}} + \hat{x}\hat{y}\sigma_{\mathrm{xy}} + \hat{y}\hat{x}\sigma_{\mathrm{yx}} + \hat{y}\hat{y}\sigma_{\mathrm{yy}} \quad (7)$$

were σ_{xx} and σ_{yy} represent the diagonal electrical conductivity, σ_{xy} and σ_{yx} the Hall conductivity, ω the angular frequency, μ_c the electrostatic biasing dependent chemical potential, Γ as the phenomenological scattering rate, T the temperature, E_0 the electric and B_0 the magnetic biasing fields normal to the surface.

Considering electrostatic and magnetostatic biasing, three separate cases can be defined [11].

1. Under the consideration of no electrostatic and magnetostatic biasing ($E_0 = B_0 = 0$), the components of the conductivity tensor become non zero operators

$$\sigma_{\mathrm{xx}} = \sigma + \alpha\frac{\mathrm{d}^2}{\mathrm{d}x^2} + \beta\frac{\mathrm{d}^2}{\mathrm{d}y^2}, \quad (8)$$

$$\sigma_{\mathrm{yy}} = \sigma + \beta\frac{\mathrm{d}^2}{\mathrm{d}x^2} + \alpha\frac{\mathrm{d}^2}{\mathrm{d}y^2}, \quad (9)$$

$$\sigma_{\mathrm{xy}} = \sigma_{\mathrm{yx}} = 2\beta\frac{\mathrm{d}^2}{\mathrm{d}x\mathrm{d}y}, \quad (10)$$

where σ, α, and β can be derived from a semi-classical Boltzmann's equation [11] to be

$$\sigma = -\frac{\mathrm{i}2\ln(2)\, e^2 k_B T}{\pi(\omega - \mathrm{i}2\Gamma)\hbar^2}, \quad (11)$$

$$\alpha = \frac{3}{4}\frac{v_\mathrm{F}^2}{\pi(\omega - \mathrm{i}2\Gamma)^2}\sigma, \quad (12)$$

$$\beta = \frac{1}{3}\alpha, \quad (13)$$

and (11) equals (23) for $\mu_\mathrm{c} = 0$.

2. For cases where the electrostatic biasing is non zero whereas there is no magnetostatic biasing nor special

dispersion ($E_0 \neq 0, B_0 = 0$), the conductivity becomes a scalar

$$\sigma_{\mathrm{xx}} = \sigma_{\mathrm{yy}} = \sigma_{\mathrm{d}}\big(\mu_{\mathrm{c}}(E_0)\big), \tag{14}$$
$$\sigma_{\mathrm{xy}} = \sigma_{\mathrm{yx}} = 0, \tag{15}$$

with $\mu_{\mathrm{c}}(E_0)$ being the electrostatic dependent chemical potential and the conductivity σ_d given by (18).

3. Under consideration of magnetostatic and possibility of electrostatic biasing, yet no special dispersion ($B_0 \neq 0$, possibly $E_0 \neq 0$), the components of the conductivity tensor are determined by

$$\sigma_{\mathrm{xx}} = \sigma_{\mathrm{yy}} = \sigma_{\mathrm{d}}(\mu_{\mathrm{c}}(E_0), B_0), \tag{16}$$
$$\sigma_{\mathrm{xy}} = -\sigma_{\mathrm{yx}} = \sigma_0(\mu_{\mathrm{c}}(E_0), B_0), \tag{17}$$

with the conductivities σ_{d} and σ_0 being given by (18) and (19), respectively.

The derivation of graphene's conductivity results from consideration of the Kubo formalism and is given in detail in [12-15]. The explicit expressions for the conductivities σ_{d} and σ_0 are given by [11].

$$\sigma_{\mathrm{d}}(\mu_{\mathrm{c}}(E_0), B_0) = \frac{(e^2 v_{\mathrm{F}}^2 |eB_0|(\omega - \mathrm{i}2\Gamma)\hbar)}{-\mathrm{i}\pi} \times \sum_{n=0}^{\infty} \left\{ \begin{array}{c} \dfrac{f_{\mathrm{d}}(M_n) - f_{\mathrm{d}}(M_{n+1}) + f_{\mathrm{d}}(-M_{n+1}) - f_{\mathrm{d}}(-M_n)}{(M_{n+1} - M_n)^2 - (\omega - \mathrm{i}2\Gamma)^2\hbar^2} \\ \times \left(1 - \dfrac{\Delta^2}{M_n M_{n+1}}\right) \dfrac{1}{M_{n+1} - M_n} \\ + \dfrac{f_{\mathrm{d}}(-M_n) - f_{\mathrm{d}}(M_{n+1}) + f_{\mathrm{d}}(-M_{n+1}) - f_{\mathrm{d}}(M_n)}{(M_{n+1} - M_n)^2 - (\omega - \mathrm{i}2\Gamma)^2\hbar^2} \\ \times \left(1 - \dfrac{\Delta^2}{M_n M_{n+1}}\right) \dfrac{1}{M_{n+1} - M_n} \end{array} \right\}, \tag{18}$$

$$\begin{aligned} \sigma_0(\mu_{\mathrm{c}}(E_0), B_0) = &-\frac{e^2 v_{\mathrm{F}}^2 eB_0}{\pi} \sum_{n=0}^{\infty} \{f_{\mathrm{d}}(M_n) - f_{\mathrm{d}}(M_{n+1}) - f_{\mathrm{d}}(-M_{n+1}) + f_{\mathrm{d}}(-M_n)\} \\ &\times \left\{ \left(1 - \frac{\Delta^2}{M_n M_{n+1}}\right) \frac{1}{(M_{n+1} - M_n)^2 - (\omega - 2\mathrm{i}\Gamma)^2\hbar^2} \right. \\ &\left. + \left(1 + \frac{\Delta^2}{M_n M_{n+1}}\right) \frac{1}{(M_{n+1} - M_n)^2 - (\omega - 2\mathrm{i}\Gamma)^2\hbar^2} \right\}, \end{aligned} \tag{19}$$

with

$$M_n = \sqrt{\Delta^2 + 2n v_{\mathrm{F}}^2 |eB_0| \hbar} \tag{20}$$

where e is the electron charge, $\hbar$ is the reduced Planck's constant, v_{F} being the Fermi velocity, Δ is the excitonic energy gap due to electron interactions with magnetic biasing, i as the imaginary unit, and f_{d} being the Fermi-Dirac distribution. It is given by [16]

$$f_{\mathrm{d}}(\varepsilon) = \left(\mathrm{e}^{\frac{(\varepsilon - \mu_{\mathrm{c}})}{k_{\mathrm{B}} T}} + 1\right)^{-1} \tag{21}$$

where k_{B} is the Boltzmann's constant, and T is the temperature.

Most research regarding electronic device applications of graphene focuses on the electrostatic biasing condition (see case 2. above). Under these circumstances, the conductivity tensor of graphene can be reduced to σ and derived from $\sigma_{\mathrm{d}}(\mu_{\mathrm{c}}(E_0), B_0)$. It is dependent on ω, the angular frequency, μ_{c}, the chemical potential, Γ, as the phenomenological scattering rate, as well as T, the temperature, and can be expressed as [16]

$$\begin{aligned} &\sigma(\omega, \mu_{\mathrm{c}}, \Gamma, T) = \sigma_{\mathrm{d}}\left(\mu_{\mathrm{c}}(E_0)\right) \\ &= \frac{\mathrm{i}e^2(\omega - \mathrm{i}2\Gamma)}{\pi\hbar^2} \left[\frac{1}{(\omega - \mathrm{i}2\Gamma)^2} \int_0^{\infty} \varepsilon \left(\frac{\partial f_{\mathrm{d}}(\varepsilon)}{\partial \varepsilon} \right. \right. \\ &\left. \left. - \frac{\partial f_{\mathrm{d}}(-\varepsilon)}{\partial \varepsilon} \right) d\varepsilon - \int_0^{\infty} \frac{f_{\mathrm{d}}(-\varepsilon) - f_{\mathrm{d}}(\varepsilon)}{(\omega - \mathrm{i}2\Gamma)^2 - 4\left(\frac{\varepsilon}{\hbar}\right)^2} \right]. \end{aligned} \tag{22}$$

Here the first and second terms represent intraband and interband contributions, respectively. This formula is often referred to as the Drude conductivity model of graphene. The individual contributions can be separately evaluated to be [16]

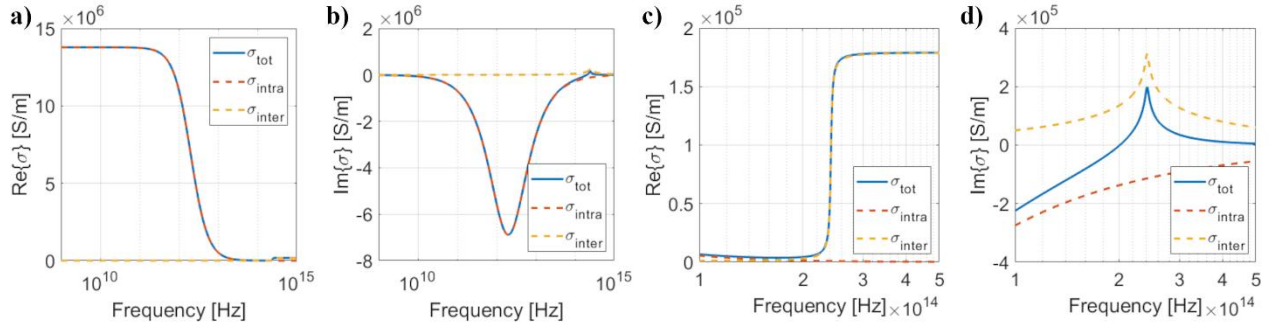

Figure 4. Graphene's conductivity model. (a) Real and (b) imaginary part of graphene conductivity for $\mu_c = 0.5$ eV, $T = 300$ K, and $\tau = 0.5$ ps. (c,d) Enhancement into frequency region of interest.

$$\sigma_{\text{intra}}(\omega, \mu_c, \Gamma, T) = -\mathrm{i}\frac{e^2 k_B T}{\pi\hbar^2(\omega - \mathrm{i}2\Gamma)}\left(\frac{\mu_c}{k_B T} + 2\ln\left(e^{\frac{-\mu_c}{k_B T}} + 1\right)\right) \quad (23)$$

$$\sigma\ (\omega, \mu_c, \Gamma, T) \cong -\frac{\mathrm{i}e^2}{4\pi\hbar}\ln\left(\frac{2|\mu_c| - (\omega - \mathrm{i}2\Gamma)\hbar}{2|\mu_c| + (\omega - \mathrm{i}2\Gamma)\hbar}\right) \quad (24)$$

where the interband conductivity is approximated for $k_B T \ll |\mu_c|, \hbar\omega$. Electrostatic biasing varies the chemical potential and will thus change the conductivity. Generally, an increase in chemical potential leads to an increase in conductivity. Alternatively, this can also be achieved via chemical doping [17] and optical pumping [18, 19]. The latter has shown to result in a negative conductivity of graphene for frequencies in the THz to the mid-IR range at sufficiently strong pumping due to a population inversion around the Dirac point caused by photogenerated electrons and holes [19].

Given the general definition of complex conductivity $\sigma = \sigma' + \mathrm{i}\sigma''$, figure 4 shows the real and imaginary part of graphene's conductivity for $\mu_c = 0.5$ eV, $T = 300$ K, and $\tau = 0.5$ ps, τ being the relaxation time and related to Γ by $\Gamma = 1/2\tau$. In the case of direct current (DC) and for a mobility of $\mu = 10\,000\ \mathrm{cm^2\,V^{-1}\,s^{-1}}$, it can be estimated to be $\tau_{DC} = \mu\hbar\sqrt{n\pi}/ev_F = 0.64$ ps [20], with n as the carrier concentration.

Two significant characteristics can be observed. First, intraband transitions are the primary conduction mechanism in the lower frequency range. They contribute significantly to the imaginary part of the conductivity. As the frequency increases, the interband contribution becomes more dominant. Second, σ_{min} represents the general optical conductivity of graphene. As the frequency is reduced, it becomes slightly less but significantly increases with even lower frequencies and can reach values up to $100\times$ the optical conductivity [21], as illustrated in figure 4.

As analyzed in [16], the propagation of surface waves is dependent on σ''. Transverse magnetic (TM) surface modes can propagate if $\sigma'' < 0$. This is mostly valid as the intraband contribution dominates in many cases. Although an introduction of chemical potential can alter the conductivity, see figure 4. The imaginary part of the conductivity becomes positive since $\sigma'' > 0$. In this case, σ''_{inter} dominates over σ''_{intra}. Therefore, only TE surface wave modes will exist.

In the THz range, interband transitions in graphene are forbidden due to the Pauli exclusion principle [22]. It results in low losses and allows for SPP wave propagation in graphene. SPPs can propagate for frequencies $\hbar\omega < 2\mu_c$ [17].

Researchers have investigated the influence of magnetic biasing on graphene's conductivity as well. Although the findings are exciting, they will not be discussed in detail here as magnetic biasing is rarely used in electronic applications.

Finally, the most striking and unconventional discovery is that graphene has been shown to exhibit an odd integer quantum Hall effect (QHE) [12, 13]. The hall conductivity exhibits a quantization that is given by

$$\sigma_{xy} = -\frac{2e^2}{h}(2n+1),\ \ n = 0,1,\ldots, \quad (25)$$

with e being the electron charge and h as the Planck's constant. In comparison, the Hall conductivity of two-dimensional electron systems takes the form of

$$\sigma_{xy} = -\frac{ve^2}{h} \quad (26)$$

where v is an integer (the integer QHE) or a fractional number (the fractional QHE) [12].

2.3 Surface Plasmon Resonance

Another essential property of graphene, and one of the reasons it is intensively studied within the THz frequency range, is its support of SPPs. This phenomenon is particularly exciting in nanophotonics as it would allow the control of light at dimensions smaller than the wavelength [20, 23]. Still, it also found meaningful application in the design of graphene antennas and other devices.

SPPs are EM waves that travel along the interface of a metal and a dielectric or air. As the name suggests, SPPs are a combination of surface plasmons (SPs), which describe

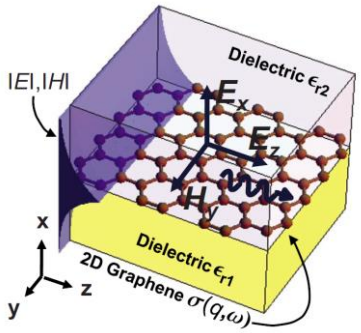

Figure 5. Transverse magnetic plasmon modes in general graphene system. Graphene is sandwiched between two dielectrics with their relative permittivities ϵ_{r1} and ϵ_{r2}. The field profile is the same as for surface plasmons at the metal-dielectric interface. Reprinted with permission from [20] Copyright (2009) by the American Physical Society.

quantized charge oscillations of electrons and holes at the interface, and polaritons, quasiparticles induced by coupling of dipole excitations (e.g., electron-hole pair) and EM waves.

For the existence of SPs, the SP carrying material needs to satisfy the following criteria: the real part of its dielectric constant $\epsilon = \epsilon' + \mathrm{i}\epsilon''$ needs to be negative, i.e. $\epsilon' < 0$, and the imaginary part ϵ'' should be significantly smaller than the negative real part of ϵ, i.e. $\epsilon'' \ll -\epsilon'$ [17, 20].

Their complex wave vector K_{SPP} defines SPP propagation properties. It is defined as [22]

$$K_{\mathrm{SPP}} = \frac{\mathrm{i}(\epsilon_1 + \epsilon_2)\epsilon_0 c}{\sigma} K_0 \tag{27}$$

with K_0 being the free-space wave vector, c the speed of light, σ being the surface conductivity, ϵ_0 representing the vacuum permittivity, and ϵ_1 and ϵ_2 are the relative dielectric permittivities of the material above and the substrate below graphene.

Its real part is related to the SPP wavelength λ_{SPP} by $Re\{K_{\mathrm{SPP}}\} = 2\pi/\lambda_{\mathrm{SPP}}$, which is much smaller than the free-space wavelength λ_0 [17]. On the other hand, the decay and propagation length of the SPPs are related to the imaginary part of K_{SPP} by $Im\{K_{\mathrm{SPP}}\}$ and $1/Im\{K_{\mathrm{SPP}}\}$, respectively. The high inductive conductivity of graphene leads to TM modes [24], see figure 5, with an effective mode index defined by [17]

$$\eta_{\mathrm{eff}} = \sqrt{1 - 4\frac{\mu_0}{\epsilon_0}\frac{1}{\sigma^2}} \tag{28}$$

with μ_0 and ϵ_0 being the permeability and permittivity of free-space, and σ being the surface conductivity of graphene.

In conjunction with metallic materials, graphene supports SPPs at a much lower frequency, namely in the mid-IR range versus near-IR to the optical range for metals [17]. At the same time, graphene exhibits low losses in the frequency regime of interest and is tuneable [20]. The latter has been demonstrated to allow for the dynamic control of the wavelength and amplitude of plasmons in graphene structures [25, 26].

2.4 Other Properties

Although not directly an electronic property, high thermal conductivity is vital for various electronic applications. One of the main problems with integrated circuits is that resistive heat must be dissipated rapidly to maintain device reliability and performance.

Particularly analog high power electronics suffer from substantial heating. The continuing trend of downsizing planar integrated technologies results in densely populated integrated circuits with long interconnects (up to above 1 km in length) and high power consumption [27], further challenging the thermal management. Three-dimensional (3D) die integration reduces the length of interconnects but leads to even higher device and power densities, with heat dissipation becoming a major bottleneck [27].

Pristine graphene has been demonstrated to show superior in-plane thermal conductivity of $\sim 5.3 \times 10^3$ W mK^{-1}. It even exceeds the best bulk crystalline thermal conductivity of diamond, which ranges between $1 \times 10^3 - 2.2 \times 10^3$ W mK^{-1} [28]. Graphene could be used as heat spreaders to aid thermal management in integrated devices [27].

The tight lattice structure of graphene makes it impermeable to even the smallest gas molecules [10]. Combined with graphene's property of compromised electrical properties upon molecular attachment on its surface, which generally is considered a disadvantage, it allows for application as molecular/gas sensors [9].

As previously discussed, graphene's unique lattice structure is the reason for its mechanical strength and elasticity. Electronic applications directly benefit from these characteristics. They result in more robust devices which can withstand significant mechanical stress and allow for new applications such as flexible electronics. Graphene has been shown to have a Young's modulus of 1 TPa and intrinsic strength of 130 GPa [29]. However, the inherently poor

adhesion of graphene to its underlying substrate can still pose an issue for manufacturability and thermo-mechanical reliability, particularly for transferred graphene [30].

A single graphene layer absorbs only about 2.3 % of the incident light, making it an interesting material for coating, or invisible electronic applications, such as optically transparent antennas [31]. A Taylor expansion can be used to estimate the transmittance [9]

$$T = \frac{1}{\left(1 + \frac{\alpha\pi}{2}\right)^2} \approx 1 - \alpha\pi \approx 97.7\ \% \qquad (29)$$

with $\alpha = e^2/c\hbar \approx 1/137$ being the fine structure constant, of which e is the electron charge, and $\hbar$ is the reduced Planck's constant. For multiple layers, this can be extended to $T \approx 1 - N\alpha\pi$, with N representing the number of layers.

The properties discussed up to this point are primarily based on free-standing, single-layer monocrystalline graphene, such as exfoliated graphene [1]. However, the properties are immediately affected if the grain sizes are small [32], several graphene layers are stacked [32, 33], and when graphene is integrated, due to its interaction with the underlying and overlying layers [34, 35], as is typically the case in integrated electronics.

2.5 How is Graphene Produced?

Quite disparate approaches for synthesizing graphene have emerged ever since the development of the scotch tape method, also referred to as mechanical exfoliation, that was used to prepare the first graphene samples [1]. They all have their particular advantages and disadvantages concerning the properties of graphene, scalability, sample size, fabrication complexity, and cost. Ultimately, the particular properties of the produced graphene determine the possible applications. Therefore, only a few of these approaches are viable for use in graphene production and its use for electronics and EM applications.

Several technologies have proven themselves to be useful for the characterization of graphene samples. The most prominent technologies are Raman Spectroscopy, Energy Dispersive X-Ray Spectroscopy (EDX), X-Ray Photoelectron Spectroscopy (XPS), Scanning Electron Microscopy (SEM), Atomic Force Microscopy (AFM), and Transmission Electron Microscopy (TEM).

As electronic and EM applications generally require homogenous and large-area graphene, this review will only focus on the fabrication of graphene via CVD and epitaxial growth on SiC. A summary of alternative manufacturing techniques is also given.

2.5.1 Chemical Vapor Deposition

Graphene layers can be grown on various, often sacrificial, metallic surfaces using CVD. The process has shown to produce large-area uniform polycrystalline graphene films [32] and was first introduced by Li et al. [36]. They grew graphene on copper foils, which were used as a catalyst, in a furnace. This is a multi-step process. First, the furnace needed to be evacuated, filled with hydrogen, and heated to 1 000 °C. During the heating process, a constant hydrogen pressure of 40 mTorr and an influx of 2 sccm needed to be maintained. The second step initialized the growth process by introducing a 35 sccm inflow of methane at a total pressure of 500 mTorr into the furnace. As the gas contacts the copper inside the chamber, a reaction occurs that allows for the formation of graphene on its surface. The growth process takes a specific amount of time, after which the furnace is turned off and cooled down. To make the grown graphene film usable for electronic device fabrication and other applications, it needed to be separated from the copper foil. For this purpose, a transfer process was developed that allowed to separate the graphene from the metal and deposit it on SiO_2/Si wafers. The growth process produces predominately single-layer graphene (SLG), with < 5 % of the area having multiple layers.

Since the introduction of CVD graphene, many variations have been developed using several different metals, carbon-source gasses, and experimental setups. Yet, they are generally based on the same principles. Graphene films of a few square meter areas have been produced, as shown by Kobayashi et al. in [37]. They used a roll-to-roll CVD process to deposit a graphene film on a 100 m long copper foil and transfer it onto a polyethylene terephthalate (PET) film. The transfer process that is used to separate the graphene film from the metal and deposit it onto another material has also been improved significantly. It allows for the transfer of the film onto a large variety of substrates and materials, such as Si, SiO_2, Quartz, PET, and many more. Recently, Xu et al. [38] developed a CVD process for growing single-crystal graphene on copper foils by reducing the synthesis time to 20 minutes. This process can potentially also be scaled to m^2 sized copper foils.

CVD graphene has been demonstrated to have excellent electrical properties. Some samples of CVD graphene transferred to SiO_2, and hexagonal boron nitride (hBN) substrates have been shown to match the properties of mechanically exfoliated graphene on a small scale [32]. They generally offer high homogeneity as well as purity and allow for reasonable control of graphene film properties. Yet, the fabrication process still brings a number of challenges with it. It is relatively labor-intensive and may produce toxic by-products. Further, the transfer process is not trivial as it can damage the graphene films and adds to the complexity. However, some applications do not require the transfer of graphene, such as corrosion protection coatings. It is also prevalent for CVD graphene to have an intrinsic chemical

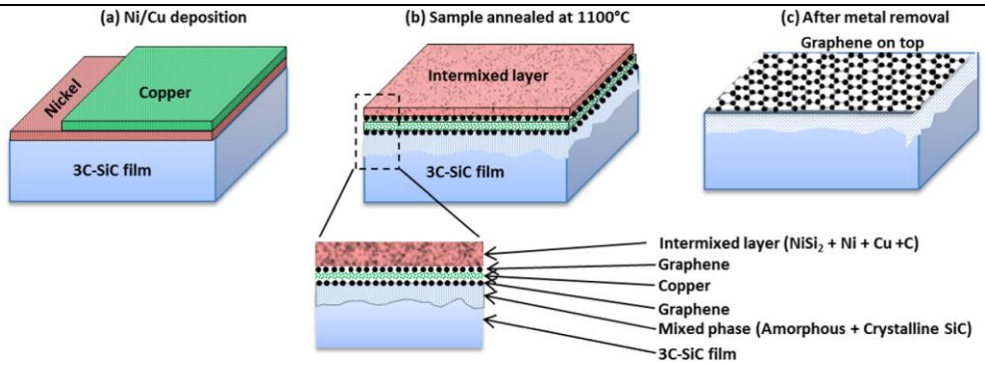

Figure 6. Catalytic alloy graphitization mechanism of SiC/Si substrates. (a) Deposition of nickel and copper catalyst metals, (b) vertical profile after annealing, and (c) vertical profile after Freckle etch. [41] © IOP Publishing. Reproduced with permission. All rights reserved.

doping profile due to the metallic catalyst used. Due to graphene's interactions with its substrate, this effect can be further enhanced with its transfer onto another material, reducing its purity and degrading its electrical and mechanical properties.

2.5.2 Epitaxial Growth on Silicon Carbide

Silicon carbide is a common substrate material used in the design of high-power electronics. Graphene layers can be epitaxially grown on its surface via thermal decomposition due to the sublimation of Si atoms and species on either its silicon or carbon faces. It has first been demonstrated by Forbeaux et al. [39] on silicon terminated 6H-SiC(0001) substrate. The process is relatively straightforward as it only requires the substrate to undergo an annealing process. An annealing temperature of 1 400 ℃ and ultra-high vacuum (UHV) with a pressure of $< 3 \times 10^{-10}$ mbar are required for graphene to form on the surface. Berger et al. [40] further analyzed the process, and they were the first to measure the graphene film's electrical properties. Their fabrication approaches were similar, but Berger et al. introduced several oxidation and de-oxidation steps to improve the surface quality of SiC before graphitization. They found that this growth process results in a stack of randomly oriented graphene layers.

The main drawbacks of this approach are the high temperatures ($1\,300 - 1\,700$ ℃) that are required to realize the graphitization, the cost of SiC wafers, as well as the restriction to small wafer sizes ($d_{\mathrm{SiC}} \approx 150$ mm) available compared to silicon ($d_{\mathrm{Si}} \approx 300 - 450$ mm) [32, 41].

Various groups investigated the use of metal catalysts with the primary goal of reducing the temperature needed for graphitization (≥ 750 ℃) [42]. The higher-quality graphene layer was found to form on the metal surface and would thus require an additional transfer process, similar to CVD-grown graphene [43].

Simultaneously, heteroepitaxial growth of cubic SiC (3C-SiC) films on silicon wafers and the graphitization thereof have been investigated [44-46]. However, the crystallographic orientation, defects, and surface roughness of the 3C-SiC/Si, significantly limit the quality of graphene formed via thermal decomposition of the pseudosubstrates [47]. The Raman spectrum commonly shows a $I_{\mathrm{D}}/I_{\mathrm{G}}$ ratio close to unity, indicative of extremely small and patchy domains [48, 49]. Recently, a catalytic alloy approach using Cu and Ni on epitaxial SiC on Si wafers has shown the capability for wafer-scale uniform graphitization [41, 50], see figure 6. Here, the graphitization takes place at lower temperatures ($900 - 1\,100$ ℃) and in high vacuum (HV) ($\sim 10^{-4}$ mbar) instead of UHV, and makes it compatible with current Silicon processing technologies [43].

The epitaxial graphene grown following this procedure has recently yielded a sheet resistance comparable to that of EG on bulk SiC [51]. The sheet carrier concentration and mobility follow the inverse power-law dependence typical of supported graphene [34]. The transport properties of EG on both bulk SiC and SiC/Si are dominated by the interface between the EG and the substrate [34, 35], which is also the case for CVD graphene. Hence, engineering of the interface needs to be carefully considered when designing integrated graphene-based devices.

In contrast to CVD graphene, epitaxial growth of graphene on SiC/Si can be used to graphitize previously patterned SiC to create three-dimensional graphene-based structures [30, 43]. It further offers much higher adhesion to the substrate, more than $6\ \mathrm{J\,m^{-2}}$, compared to tranfered graphene, $1.5 - 2\ \mathrm{J\,m^{-2}}$ [30].

2.5.3 Other Techniques

Mechanical exfoliation produces graphene samples with the best electrical properties. The samples are prepared by repeatedly exfoliating graphite until left with a single layer of graphene. It is a highly random process and generally produces only tiny flakes of graphene. This makes it only applicable to research in laboratory environments [32].

Another example of an exfoliation technique is liquid-phase exfoliation. In liquid-phase exfoliation, graphite is exposed to an organic solvent. Initial sonication results in the splitting of first graphite pallets from the graphite sample. Further sonication allows for the graphene pallets to break down into graphene flakes [52]. Solution-mediated approaches are widespread, and a large number of graphene flakes can be produced this way. Their major drawback is that deposited layers can only be formed by overlapping the flakes rather than homogenous and conjoined layers. Instead, they are ideal for the fabrication of graphene paints and inks [32].

CNTs were discovered before graphene. They can be seen as rolled-up graphene sheets. Several methods have been developed that allow for the unzipping of CNTs to form graphene nanoribbons [53].

Other graphene fabrication processes are available but will not be discussed here due to the lack of utility towards electronic and EM applications.

2.5.4 Graphene Inks/Graphitic Films

There are various approaches to synthesize conductive graphene ink, each offering different characteristics. Researchers are continuously working on improving their properties, and most importantly, their conductivity. Graphene flakes that are commonly fabricated using liquid-phase exfoliation, see above, are their main ingredient.

Generally, conductive graphene inks can be divided into two categories depending on whether they have been made with or without binders [54, 55]. Binder-free graphene ink only consists of graphene flakes and an organic solvent such as N-Methyl-2-pyrrolidone (NMP), Dimethylformamide (DMF), or Dihydrolevoglucosenone (Cyrene), with the former two being toxic and unsustainable [56]. On the other hand, binder-based inks contain binders such as ethyl cellulose (EC) or cellulose acetate butyrate (CAB). The insulating nature of binders makes them generally unusable for RF applications. However, a compromise in the graphene ink's conductivity can be acceptable in some cases, depending on the application. Even though high-temperature annealing has been shown to improve the conductivity of binder-based graphene inks, this processing step makes them incompatible with heat-sensitive substrates [55]. Other conductive films are often made of metal nanoparticles [57] or conductive polymers [58]. Nevertheless, they have drawbacks such as high cost, the possibility of oxidization, low conductivity, or low thermal and chemical stability [54-56]. Graphene inks offer a cost-effective alternative that could resolve those issues.

Graphene ink has the advantage that it can easily be printed on various substrates, such as PTFE, glass, paper, cardboard, and more, depending on the type of ink used [55, 59]. The ink can be deposited using inkjet printing, doctor-blading [55], or screen printing, each having its specific advantages [56]. However, due to the thickness of the ink films, graphene ink-based devices lose their transparency and can not be considered graphene anymore. Instead, they can be referred to as graphitic films, laminates, or layers.

Graphitic films with metallic-like conductivities of up to $\sim 1.43 \times 10^6$ S m^{-1} [60], which at a 25 µm layer thickness results in a sheet resistance of 29 mΩ □$^{-1}$, have been reported. They lead to lower ohmic-losses and improved antenna performances, making them an excellent alternative to typical metal films in flexible antenna applications.

2.6 Structuring of Graphene

Basic research around the synthesis of graphene mainly focuses on the creation of uniform, high-quality unpatterned graphene. However, most applications require a precise and defect-free structuring of graphene.

Plasma-based dry etching is currently the most common approach to pattern graphene [61]. Generally, oxygen (O_2) gas plasma is used, and graphene is etched via the oxidation of the carbon atoms [62, 63]. A mask, e.g., metal or photoresist, is commonly used to cover the graphene that is not to be etched [62]. Some of these processes may introduce additional defects and damage the graphene [64].

Recently, maskless approaches have been explored. They significantly simplify the structuring process and can reduce the risk of contaminating or damaging the graphene during the deposition of the masking layer. Such approaches include focussed ion beam (FIB) [65, 66] and laser direct writing [67, 68].

In addition, very recent research focuses on atomic layer etching, where individual graphene layers can be removed. These are also optimized to minimize the introduction of defects and contamination to the underlying graphene layers [69].

Alternatively to etching the graphene, the unpatterned layer can be selectively oxidized [61, 70, 71], chemically doped, or biased [72-74] to achieve the effect of a patterned structure. For example, in the former, an ultraviolet (UV)-ozone treatment transforms graphene to graphene oxide (GO), creating local insulating and conducting areas [61], while in the latter, localized biasing creates patches within the same layer of graphene that have different conductivities [74].

Finally, as already discussed in section 2.5, graphene can be patterned by leveraging the unique properties of some of the synthesis processes. For example, EG grown on SiC/Si can be structured by pre-patterning the SiC layer on silicon [30, 43]. On the other hand, graphene-ink films can be patterned using inkjet printing, doctor-blading, or screen printing [56].

3. Generation, Manipulation, and Detection of Microwave and Terahertz Electromagnetic Fields

The microwave (300 MHz to 300 GHz) and THz (often now taken to be 100 GHz to 30 THz) frequency ranges have attracted a lot of interest in recent years. Current wireless

technologies, e.g., mobile communication, broadcasting, etc., use up a large portion of the lower frequency spectrum. The latest technology generation of cellular networks, the so-called fifth-generation (5G), includes frequencies up to 300 GHz. Not only do they overcome the current spectrum sparsity, but higher frequencies also facilitate a significant improvement in data transmission rates and latency. In addition to upgraded communications, the THz frequency range enables medical, sensing, imaging, defense, and other applications [17, 75]. There is currently a lot of focus on the THz frequency range because of them and a lack in the number of available sources and devices to meet them [17].

A variety of metals are used for radio frequency (RF) systems. Their application in the THz range faces significant challenges because they then exhibit a significant degradation in their conductivity and skin depth [17]. Both of these properties result in low radiation efficiencies in antenna applications and reduced transmission and propagation capabilities as interconnects.

THz sources still suffer from limited power levels. Consequently, what energy they do provide needs to be preserved as much as possible. Furthermore, THz waves experience strong attenuation as they propagate through the atmosphere. It is therefore essential to design high directivity and highly efficient devices to overcome these propagation losses [76].

Graphene-based antennas are a highly researched topic. However, the plasmonic properties of graphene do not play a significant role in the microwave frequency range. Its electrical and mechanical properties are of particular interest instead. These include graphene's high conductivity [77], optical transparency [31], flexibility [78], and tunability [79].

In addition, biosensing describes an emerging platform of graphene devices that utilizes, among others, optical and electromagnetic properties of the 2D material. Today, graphene-based biosensors research spans a wide range of health applications, such as for the detection of motion [80], neural signals [81], or biomarkers, which include but are not limited to: DNA (deoxyribonucleic acid), microRNA (micro ribonucleic acid), molecules, and Proteins [82, 83]. RF and plasmonic devices based on graphene have recently been investigated in [80, 83].

Through the presence of SPPs in the THz frequency range, EM fields experience significant confinement in graphene. This feature leads to a significant size advantage compared to the use of metal [24]. Recent research has shown that plasmonic graphene ring structures experience a 20-fold enhancement of the electric field as compared to metallic counterparts [84]. Moreover, the possibility of tuning graphene's electrical properties using various biasing mechanisms allows for dynamic reconfiguration of various properties of antennas, such as their resonance frequencies [24] and radiation patterns [85].

Leaky wave antennas (LWA) rely on waves traveling in guiding structures. EM waves are radiated due to perturbations introduced on those structures, which are typically metallic or dielectric waveguides. One exciting feature of most LWAs is their frequency scanning ability, where the beam direction is scanned by varying the operating frequency of their sources [86]. However, in communication applications, one needs beam scanning at a fixed frequency and the ability to change it [87]. This problem can be mitigated in several ways associated with the physics of periodic structures and intelligent engineering. It is a continuing research area in LWAs. Graphene's tunability can be used for beam scanning LWAs while maintaining the ability to change the operating frequency [86]. Furthermore, LWAs can be extended to planar array designs using metasurfaces [88].

Metamaterials are engineered materials whose properties can be tailored to specific applications. They consist of sub-wavelength 3D structures embedded in a substrate, generally referred to as unit cells or meta-atoms, that are usually assembled in a repeating pattern. The characteristics of any metamaterial are mainly determined by the meta-structures and their couplings rather than the substrates' properties. Metamaterials are convenient for designing devices used, for instance, in beamforming applications because they facilitate the necessary manipulations of the amplitude, phase, and polarization of EM waves exciting them. Historically, metallic metamaterials have dominated their applications. However, strong absorption and complex manufacturability of 3D micro- and nano-structures have hindered them from being employed at THz and higher frequencies [18].

Metasurfaces are the 2D complements of 3D metamaterials. They comprise an array of sub-wavelength planar structures, also generally referred to as unit cells or meta-atoms, and are often made of metals on a dielectric substrate, but more recently as all-dielectric structures. The individual unit cells act as scatterers, and the response of impinging EM waves can be reasonably determined by Snell's law of refraction and reflection [89]. They have the main advantages of being low profile, lightweight, and being easy to manufacture and are commonly used for generating [88], manipulating [90], and absorbing [91] EM fields. They have found and continue to be envisioned for applications in spectroscopy and communications as antennas, antenna arrays, lenses, and absorbers.

Until recently, metasurfaces could not be dynamically reconfigured. Their properties were fixed by their design and specific application [92]. However, dynamic tunability of the metasurface properties and their EM responses is essential for applications such as beam scanning, wavefront manipulation, frequency filtering, and multi-spectral absorbers. In particular, dynamic reconfiguration at THz frequencies and beyond had suffered from the lack of compact tunable elements [93].

Depending on the application, frequency region, metasurfaces can be dynamically reconfigured using various methods[94]. These include, but are not limited to: MEMS [95], liquid crystals [96], phase-change materials such as vanadium dioxide (VO_2) [97] or chalcogenides (e.g. GeSbTe (GST)) [98]; and transparent conductive oxides such as indium tin oxide (ITO) [99]. Tunability is achieved by dynamically changing the geometry of the metasurface or its dielectric permittivity. The particular technology used will significantly influence the response time of the system [92].

The angular frequency dependant permittivity of graphene is related to its surface conductivity via [100]

$$\epsilon_{\mathrm{Gr}}(\omega) = \epsilon_0 + \frac{\mathrm{i}\sigma(\omega)}{\omega\Delta} \tag{30}$$

where ϵ_0 is the permittivity of free-space, ω as the angular frequency, Δ the graphene layer thickness, and $\sigma(\omega)$ as graphene's surface conductivity from (22). Graphene can therefore be used to dynamically reconfigure the EM response of graphene-based metasurfaces and broaden the scope of its applications [93]. Electrostatic biasing using a capacitive gate is the most commonly used approach and is quite well defined [101]. Electrostatic biasing can also be achieved using planar side gating [102], a solid polymer electrolyte [103], or ion gel [104]. Optical pumping [18] and chemical doping [105] have also been explored for tuning graphene's properties. However, much care must be taken when graphene's tunability is used to design the biasing architecture. For example, the biasing network for electrostatic biasing can influence the properties of a graphene-based device.

A wide range of numerical and analytical approaches have been used to characterize the phase response of graphene-based metasurface unit cells. The most common are equivalent circuit models or full-wave simulations [88, 91, 103, 106-108].

Apart from LWAs, graphene-based metasurface structures at THz frequencies are commonly used to design reflectarrays [106], transmitarrays [18], high impedance surfaces [109], and absorbers [91]. Their planar design allows for ease of fabrication using common nanofabrication processes.

Even though GFETs have not managed to match the capabilities of semiconductor-based FETs, they have found application in the area of EM field detection [110-112]. Graphene allows for several detection mechanisms, with the main focus lying in the THz frequency range.

3.1 Antennas

Most antennas are currently realized with a variety of different metals. Metals offer high electrical conductivity, and many are relatively inexpensive, and there are many antenna fabrication processes available. Depending on the specific frequency range of interest, antennas can be fabricated with a variety of processing techniques, including, for example, conduit, milling, printing, or nanofabrication via lithography [87]. Copper is currently the most widely used material for fabricating antennas in the RF and microwave frequency range. However, as noted above, metals suffer from significant conductivity and skin depth degradation in the THz regime, resulting in high ohmic losses [17]. The prominent properties of graphene for antenna applications, i.e., its high electrical conductivity, mechanical flexibility and robustness, transparency, support of SPPs, and the possibility of dynamic tunability, allow for the design of optically transparent antennas [31, 70, 71], flexible antennas for wearable electronics [54, 113], and miniaturized nanoantennas for high-speed data transmission at the nanoscale [114, 115]. Furthermore, graphene's tunability can reconfigure antennas in various ways, such as dynamically changing its radiation pattern [85, 116, 117]; resonance frequency [17, 24, 114, 117] and frequency scanning [86, 118]; and beam scanning at a fixed frequency [86, 101].

3.1.1 Microwave Frequency Range Graphene Antennas

Early near-field characterization of the exposure of CVD graphene patches deposited on metal microstrip lines to electromagnetic fields indicated that graphene is dominated by losses in the X-band ($7.0-11.2$ GHz) due to its high sheet resistance. Comparing the effectiveness of the fields radiated by a few-layer graphene patch to a copper patch of identical dimensions, it has been shown that their radiation efficiencies were on the order of 20.7 % and 80 %, respectively [119]. A later study on the near-field radiation of capacitively coupled CVD graphene-based patches consisting of one to five layers of graphene indicated that no microwave resonance is present for patches with sheet resistances of $> 0.6\,\mathrm{k\Omega}\,\square^{-1}$ and predicted that sheet resistances of $< 10\,\Omega\,\square^{-1}$ are necessary for microwave antenna applications [77]. Regardless, researchers have successfully demonstrated antennas based on graphene with inferior conductivities that still perform sufficiently well depending on the application, e.g., radio frequency identification devices (RFIDs) [55].

Although graphene's most interesting properties will not significantly influence antenna realizations in the microwave frequency range, researchers have investigated graphene antennas' performance, properties, and possibilities in this frequency range. In contrast to antennas in the THz range, graphene-based ones in the microwave range have been experimentally analyzed and, in some cases, compared to metallic antennas. The focus has been mainly in the fabrication of flexible [54-56, 59, 60, 78, 80, 113, 120-123], transparent [31, 70, 71], and tunable antennas [78, 79, 124-129].

3.1.1.1 Microwave Resonant Antennas

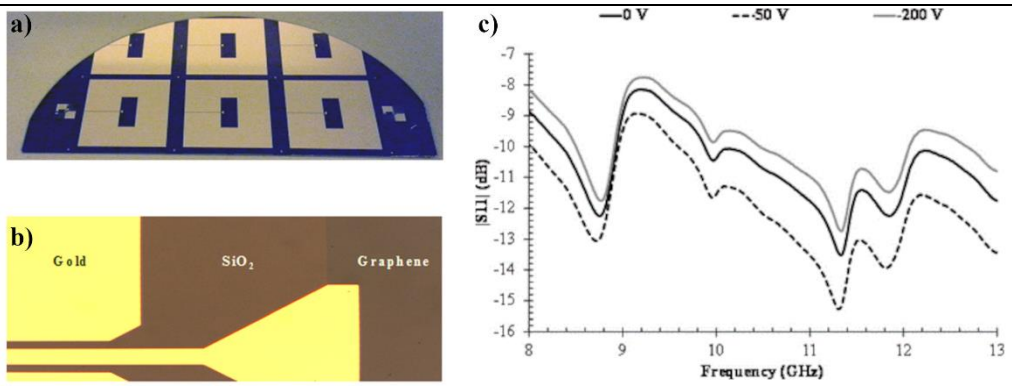

Figure 7. Printed microwave graphene antenna. (a) Fabricated graphene patch antennas on the SiO_2/Si substrate surrounded by a gold ground plane. (b) Magnification of the gold, SiO_2, and graphene interface. (c) Measured $|S_{11}|$ values in the X-band for 0, 50, and 200 V biasing voltage. Reprinted from [124], with the permission of AIP Publishing.

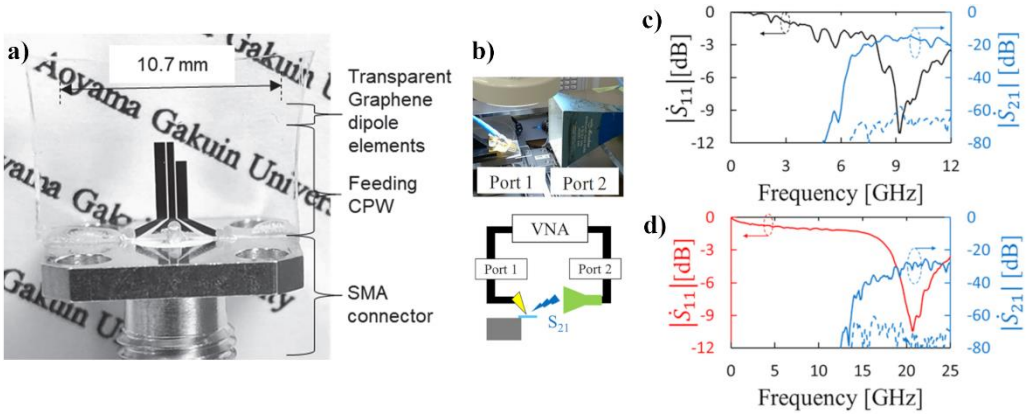

Figure 8. Optically transparent chemical vapor deposited graphene-based dipole antenna. (a) Graphene-based antenna connected to SMA connector. (b) Probe station measurement setup for characterization of the reflection and transmission coefficients. (c,d) S-parameter measurement results for the (c) gold and (d) graphene antennas. (a) © 2018 IEEE. Reprinted, with permission, from [71], (b) Reprinted from [70], with the permission of AIP Publishing.

Resonant antennas get their name from their fundamental operating characteristic. They exhibit resonant current and voltage standing waves arising from internal reflections that occur from their structure, such as from edges or open ends. They are also known as standing wave antennas [130]. Examples of resonant antennas are monopole, dipole, and patch antennas. Their dimensions are directly related to integer multiples of $\lambda/2$, where λ is the wavelength associated with the resonance frequency in the structure.

Dragoman et al. [124] have fabricated antennas from CVD graphene that were transferred onto SiO_2/Si wafers (see figure 7(a)). Raman spectroscopy indicated low defects, and mostly SLG was confirmed. The graphene patch was structured using reactive ion etching (RIE) and used as the main radiating element. It was surrounded by a grounded gold plane and fed by a coplanar waveguide (CPW), both being made of gold. The substrate was mounted on a metal stage that doubled as the back metalization. The reflection parameter $|S_{11}|$ of the antenna is characterized using a vector network analyzer (VNA) and a ground-signal-ground (GSG) probe at $8-13$ GHz. Biasing was applied through the GSG probe (side gated biasing of the radiating graphene patch via the surrounding gold plane). The overall reflection loss was about -9 dB and has two distinct resonances at 8.8 and 11.4 GHz with corresponding reflection coefficients of -12.2 dB and -13.4 dB, respectively. In contrast to the analogous metallic antenna, the graphene antenna had a wide bandwidth. The application of biasing slightly shifted the reflection loss spectrum vertically. The reason for this was the variation of the graphene surface resistance and the improper impedance matching of the antenna to the 50 Ω VNA port [124]. The resulting shifts in the resonances were within 24 MHz, as shown in figure 7(b). Dragoman et al. mentioned that the high resistance of the graphene induces high losses, which would explain the shifts. Moreover, only moderate radiation efficiencies were measured because of it if no biasing was applied. However, no values for the antenna gain or efficiency were specifically given.

Kosuga et al. [70, 71] designed optically transparent dipole antennas made of CVD SLG on quartz and compared their

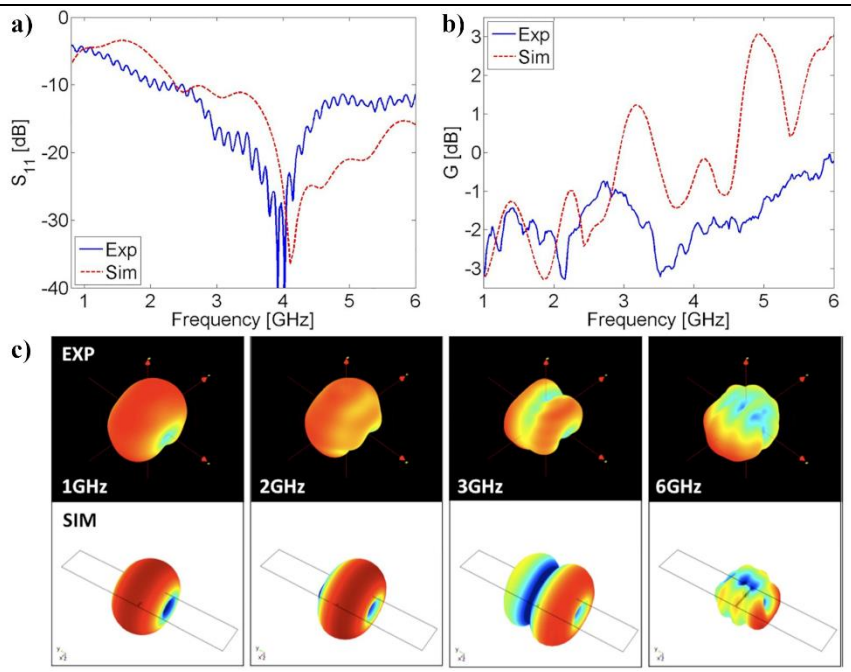

Figure 9. Optically transparent graphene dipole antenna. (a, b) Comparison of experimental and simulated (a) $|S_{11}|$ and (b) gain values. (c) Comparison between experimental and simulated 3D radiation patterns at 1, 2, 3, and 6 GHz. Reprinted from [31], with the permission of AIP Publishing.

performance to dipole antennas made of gold. Structuring of the graphene was done using UV-ozone treatment with gold masks. Removal of the mask exposed the transparent graphene antenna; see figure 8(a). The antennas were characterized in [70] using a VNA and a probe station. The transmitting port is connected to the antenna via a GSG probe, and the receiving port is connected to a horn antenna, as illustrated in figure 8(b). The measurement showed resonances at 20.7 GHz for the graphene and at 9.2 GHz for the gold antenna with similar absorption coefficients of around -10 dB. Considering the resonance shift to a higher frequency, the graphene antenna appears electrically larger, which is not desirable.

The antennas in [71] were fabricated with the same dimensions as in [70] but were fed via a SubMiniature version A (SMA) connector instead of a probe. The CVD graphene was electrically characterized. It had a conductivity of 4.0×10^6 S m^{-1}, which corresponds to a sheet resistivity of 750 Ω □$^{-1}$. The reflection loss was determined with a VNA. Similar resonances were measured, i.e., at 21.6 GHz for the graphene-based antenna and at 9.5 GHz for the gold antenna. Moreover, the absorption coefficients vary significantly with -11 dB for graphene and -20 dB for the gold antenna. The half-power beamwidth characterization shows that the graphene antenna has a higher directivity compared to the Au antenna with 6.2 dBi and 5.2 dBi, respectively. However, the simulations predicted that the gain of the graphene antenna would be 4.2 dB higher. The reduction is associated with the significantly lower conductivity of graphene, and it was suggest that SLG behaves more like a dielectric than a metal [71]. Similarly, it was expected that the resonant frequency of the graphene antenna would be affected by the dielectric constant of graphene, making the antenna appear physically smaller, contrary to the expectations for the THz regime associated with SPP effects.

Grande et al. [31] investigated the dielectric behavior of graphene further, and they suggested using multi-layer graphene (MLG) to reduce the sheet resistance of the graphene film. Additionally, they doped the individual graphene layers using $SOCl_2$. Stacking six of these doped CVD graphene layers on a glass substrate, they achieved a sheet resistance of 18 Ω □$^{-1}$ with a total optical transmittance of 85 %. However, they indicated that stacking individual graphene layers only works for a limited amount of layers. The conductivity saturates with increasing layer count and decreases the conductivity of bulk graphite if further layers are added due to interlayer interactions and impurities [31, 33]. A wide planar antenna design with dimensions of 75 mm × 25 mm was used to provide a wider bandwidth compared to dipole antennas. It provides a -10 dB bandwidth of $>$ 3.5 GHz and an average gain of -1 dBi with an average efficiency of 21 % (see figure 9(a) and 9(b)). Figure 9(c) shows the radiation pattern of the antenna. Its dipole-, quadrupole-, and hexapole-like behavior agree well with simulation results.

The dynamic tunability of graphene's electrical properties only plays a marginal role in the microwave range. Graphene behaves as a variable frequency-independent resistor [124] when subjected to biasing, e.g., electrostatic biasing. Non-

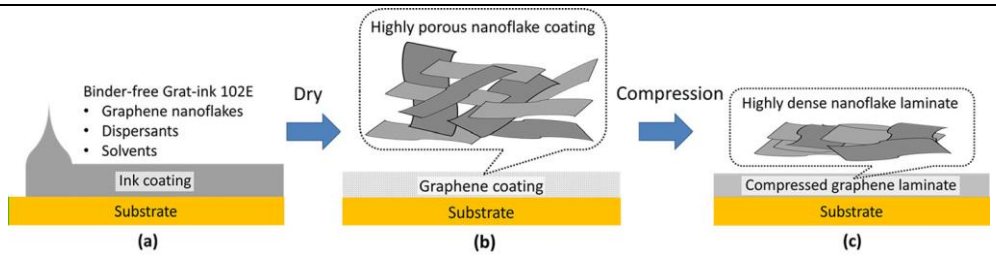

Figure 10. Schematic illustration of fabricating a binder-free conductive compressed graphene laminate (In this review referred to as graphitic film). Reprinted from [55], with the permission of AIP Publishing.

transparent microwave antenna implementations made of metal significantly outperform graphene ones. However, CVD graphene could still be used in transparent applications, e.g., for invisible antennas on screens or glass, if the low radiation efficiency can be tolerated. Current alternatives to CVD graphene are ITO [131, 132], indium-zinc-tin-oxide (IZTO) [133], fluoride-doped tin oxide (FTO) [131], silver-coated thin films (AgHT-4) [134], and metal mesh patches [133, 135]. Each has its distinct advantages and disadvantages concerning transmittance, conductivity, sustainability, manufacturability, and cost [31, 132]. While SLG provides the highest optical transparency, metal mesh layers provide sheet resistivities as little as $0.18\,\Omega\,\square^{-1}$ [133] and result in significantly lower losses and improved antenna performance.

3.1.1.2 Flexible Graphene Ink Antennas

Due to its high elasticity and mechanical robustness, graphene can be used for flexible antenna applications [136]. CVD graphene would be ideal for this purpose as it can be transferred onto flexible films [37]. To our knowledge, no flexible antennas based on CVD graphene or EG grown on bulk SiC or SiC/Si have been realized to date. Nevertheless, these antennas would still suffer from the issues introduced in 3.1.1.1. Instead, conductive graphene inks have established themselves along with metal nanoparticles, conductive polymers, and liquid metals [137] as an alternative for flexible antenna applications [54-56, 59, 60, 78, 80, 113, 120-123].

Huang et al. [55] used commercially available binder-free graphene ink (Gra-ink 102E from BGT Materials Ltd) to fabricate a flexible antenna. Simply depositing and drying the graphene ink resulted in a graphitic film with low conductivity due to its roughness and high contact resistance between the graphene flakes. Applying rolling compression to the film resulted in improved conductivity. At a compression ratio of 19 %, which refers to the thickness of the compressed layer compared to the uncompressed one, the conductivity increased by a factor of $> 50\times$ from $8.3 \times 10^2\ \mathrm{S\,m^{-1}}$ to $4.3 \times 10^4\ \mathrm{S\,m^{-1}}$. Adhesion, which is a general problem for binder-free graphene inks [55], also improved after the compression. Figure 10 shows a schematic representation of creating compressed graphitic films from graphene ink. SEM images confirmed a much smoother and denser surface where individual graphene flakes were barely visible after compression [55].

A half-wavelength dipole antenna was fabricated by depositing a graphitic film on paper using the doctor-blading technique via a stainless steel stencil [55]. The reflection coefficient of the antenna shows a minimum of -11.6 dB at 960 MHz, and the -10 dB bandwidth is from 890 MHz to 1 020 MHz. The authors correctly stressed that the reflection coefficient not only indicates how well the antenna is impedance matched to the source but also how well power is transmitted from the source to the antenna, i.e., propagation losses in the feed lines also impact it. The low conductivity of the graphitic film resulted in high resistive losses. The maximum gain is -0.6 dBi at 962 MHz while an ideal half-wavelength dipole antenna has a theoretical gain of 2.14 dBi. They state that a -1 dBi gain is enough to exceed the 10 m maximum reading range needed for RFID applications [55].

In more recent publications, Huang et al. [54, 120] analyzed the properties of flexible transmission lines and various antenna designs made of graphene ink-based graphitic films. They found that repeated bending of a transmission line had little effect on its transmission properties (see figure 11(g)). Analysis of a CPW fed slot antenna made using the same graphitic film showed that the antenna's gain, resonance frequency, and radiation pattern were not sensitive to various bending angles. They only resulted in slight variations (see figure 11(e, f)). The unbent antenna showed good impedance matching with the reflection coefficient $|S_{11}|$ having two resonances at 1.97 GHz and 3.26 GHz with a -18.7 dB and -19.2 dB reflection loss, respectively [54]. They suggested that flexible graphitic film-based antennas are a viable option for wearable applications.

Song et al. [59] deposited graphene ink on polytetrafluoroethylene (PTFE) substrate to form graphitic films with conductivities as high as $10^6\ \mathrm{S\,m^{-1}}$. They fabricated a flexible microstrip antenna array with it. A comparison of the reflection coefficient between the fabricated graphitic film and a copper antenna array of equal proportions demonstrated that the graphitic film antenna exhibited a slight resonance shift to higher frequencies, i.e., from 2.46 GHz for the graphitic film to 2.44 GHz for the copper antenna. Moreover, it had a significantly lower return loss with -40.28 dB compared to -33 dB at their respective

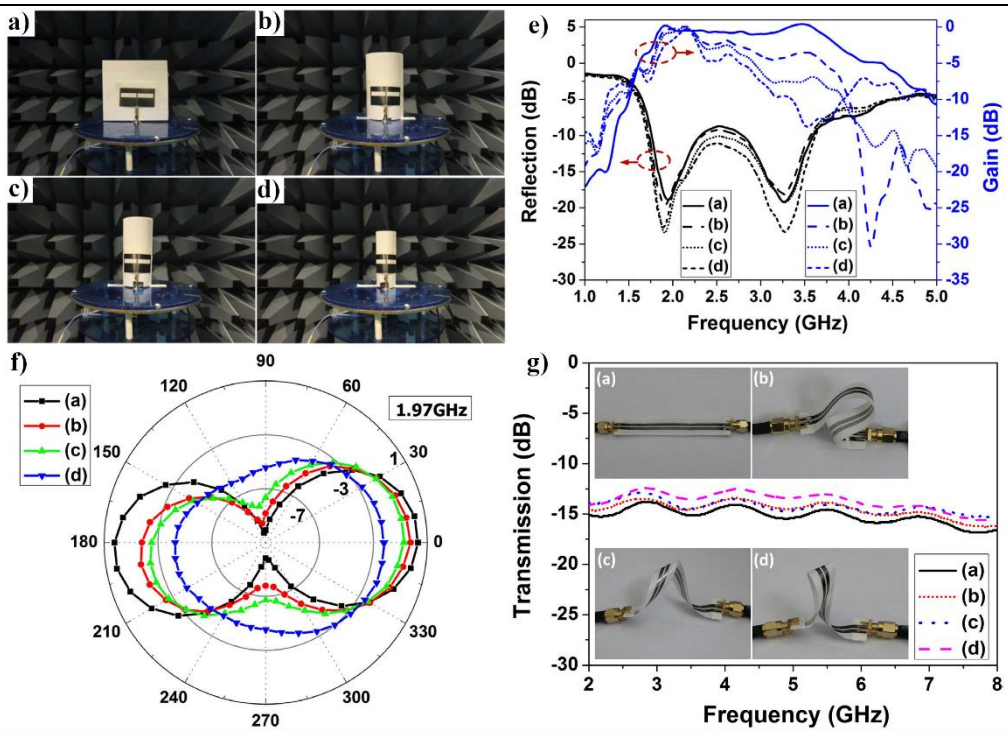

Figure 11. Flexible complementary dipole antenna made of binder-free graphene ink-based graphitic film. (a-d) Antenna under different bending radii: (a) un-bend, (b) bend with 5 cm, (c) 3.5 cm, and (d) 2.5 cm radius. (e, f)) Measurement results of graphitic film antenna for different bend scenarios (a-d) (e) Reflection coefficient and realized gain, (f) 1.97 GHz radiation patterns. (g) Transmission performance of (a) un-bent, (b) bent, and (c,d) twisted transmission line made out of the graphitic film. [54] © 2018, CC BY 4.0. To view a copy of this license, visit http://creativecommons.org/licenses/by/4.0/

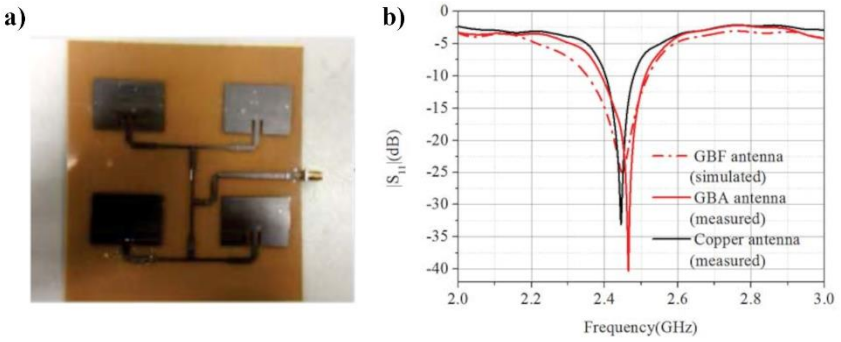

Figure 12. Antenna array made of a graphitic film called graphene-based film (GBF) in the reference. (a) Graphitic film-based patch antenna array on FR-4 PCB material. (b) Comparison of the reflection coefficients of the simulated and measured graphitic film and copper antennas. © 2017 IEEE. Reprinted, with permission, from [59]

resonances. The bandwidth increased from 80 MHz for the copper antenna to 120 MHz for the graphitic film antenna. Both antennas exhibited a similar radiation patterns in the elevation plane with a maximum gain of 6.78 dB for the graphitic film and 7.11 dB for the copper antenna.

Zu et al. [113] developed a circularly polarized antenna for wearable applications based on a highly conductive graphitic film (CGF). It is very similar to the graphitic film introduced in [59] but instead uses flexible polydimethylsiloxane (PDMS) as the substrate. The films have metal-like conductivities as high as 1.13×10^6 S m^{-1}. They stressed that the graphitic film has a density of only 1.8 g cm^{-3}, which is < 25 % of that of copper (8.8 g cm^{-3}). The robustness of the film was demonstrated by exposing a strip of the graphitic film to 1 000 bending cycles and then comparing its performance to that of a copper film. While the resistance of the graphitic film strip remained unchanged, the copper strip broke after 28 cycles.

Their circularly polarized antenna was a monopole patch that was supported by a foam block over a 3×3 artificial magnetic conductor (AMC) array (see figure 13(a)). Right-hand circular polarization (RHCP) was achieved by setting the

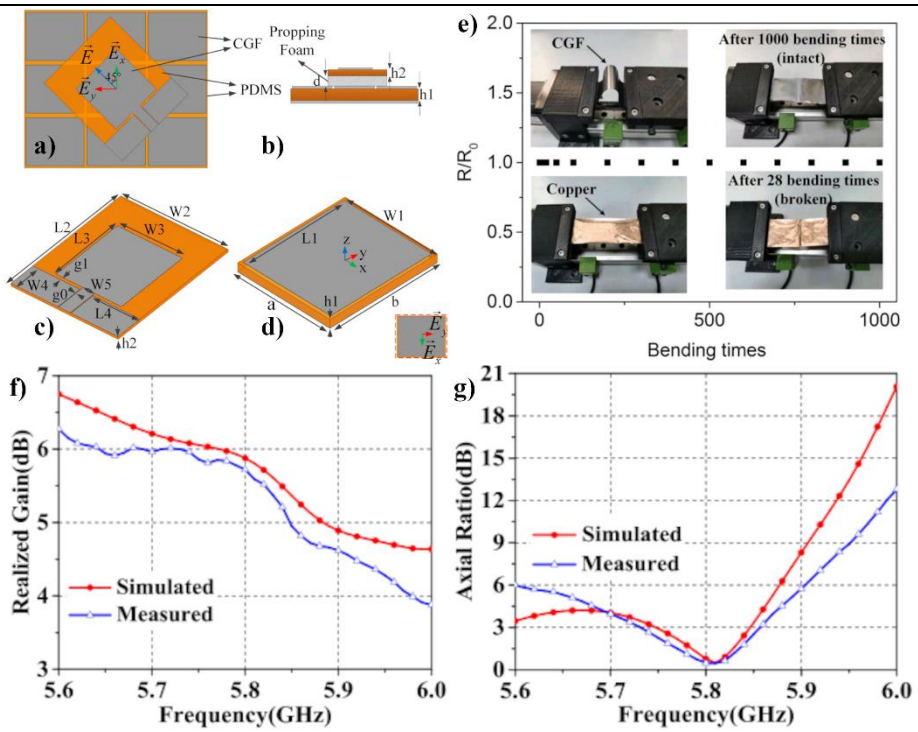

Figure 13. Wearable antenna made of a graphitic film called conductive graphitic film (CGF) in the reference. CGF monopole antenna supported using propping foam over AMC array. (a) Top and (b) side view of the antenna. (c) Dimensions of the monopole patch and (d) the AMC array unit cell. (e) Comparison of the robustness of CGF and copper film using bending test. (f, g) Comparison of simulated and measured realized gain and axial ratio. © 2020 IEEE. Reprinted, with permission, from [113]

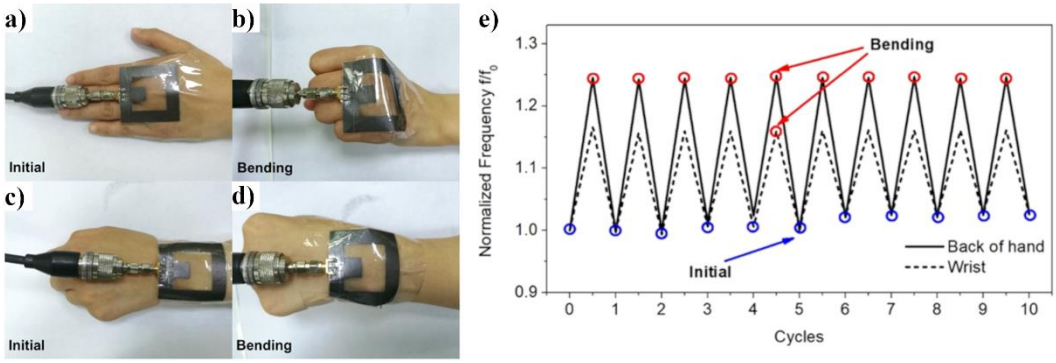

Figure 14. Flexible graphitic film-based antenna for human motion detection. With flexible antenna attached to (a, b) back of the hand, or (c, d) wrist, in either (a, c) relaxed, or (b, d) bent state. (e) Normalized frequency variation comparison for both configurations. Reprinted with permission from [80]. Copyright 2020 American Chemical Society. Further permissions related to the material should be directed to the American Chemical Society.

reflection phases of the AMC array in the x-direction and y-direction to 90 ° and −90 °, respectively. The antenna was designed for an operating frequency of 5.8 GHz. Simulations of the antenna design indicated that the antenna had a radiation efficiency that was greater than 70 % both on and off the body. Furthermore, the specific absorption rate (SAR), which indicates the rate at which a body absorbs EM energy, of the antenna complied with international standards set by the FCC and ICNIRP. Experimental measurements of the antenna agreed with the simulated results quite well. The antenna was well-matched to its source, with the reflection coefficient being < -10 dB within the frequency range of $5.6 - 6$ GHz. The co-pol RHCP gain was 20 dB higher compared to the cross-pol left-hand circular polarisation (LHCP) value. Thus, good polarization isolation was attained. The realized gain of the antenna is $5 - 6.1$ dBic within the frequency range of $5.75 - 5.83$ GHz. Unfortunately, measured radiation efficiency results were not reported.

Table 1. Comparison of microwave antenna implementations

Technology	Design	Operation Frequency [GHz]	Conductivity/ Sheet Resistance	Return Loss [dB]	Gain	Ref.
Copper on acryl	Patch antenna (36 mm × 40 mm)	2.45	$0.02\ \Omega\ \square^{-1}$	-12.5	4.75 dB	[133]
CVD SLG on SiO_2/Si	Tunable folded slot antenna (9.5 mm × 2.9 mm)	8.8, 11.4	-	-12.2, -13.4	-	[124]
Gold on quartz	Dipole antenna (10.7 mm)	9.5	$4.1 \times 10^7\ \text{S m}^{-1}$	-20	5.2 dBi	[71]
Multilayer film IZTO/Ag/IZTO	Transparent patch antenna (36 mm × 40 mm)	2.45	$2.52\ \Omega\ \square^{-1}$	-8.4	-4.23 dB	[133]
Copper mesh on acryl	Transparent patch antenna (36 mm × 40 mm)	2.45	$0.18\ \Omega\ \square^{-1}$	-14.5	2.63 dB	[133]
$SOCl_2$ doped CVD MLG on quartz	Transparent wide planar antenna (75 mm × 25 mm)	4 (3.5 GHz BW)	$18\ \Omega\ \square^{-1}$	-40	-1 dBi (avg.)	[31]
ITO on glass	Transparent patch antenna (12 mm × 8.85 mm) with frequency selective surface	5.725– 5.850	$7\ \Omega\ \square^{-1}$	< -10	-6 dBi	[132]
CVD graphene on quartz	Transparent dipole antenna (10.7 mm)	21.6	$4 \times 10^6\ \text{S m}^{-1}$ ($750\ \Omega\ \square^{-1}$)	-11	6.2 dBi	[71]
Ag-nanoparticle ink on PET	Flexible Z-shaped microstrip patch antenna (34 mm × 25 mm)	0.9, 2.4	-	-16.45, -26	16.74, 16.24 dBi	[138]
Graphene ink on paper	Flexible half-wavelength dipole antenna (68.82 mm)	0.96 (112 MHz BW)	$4.3 \times 10^4\ \text{S m}^{-1}$ ($3.8\ \Omega\ \square^{-1}$)	-11.6	-0.6 dBi	[55]
Copper film on PTFE	Flexible microstrip array antenna (2 × 2)	2.44 (80 MHz BW)	-	-33	7.11 dB	[59]
Graphene ink on PTFE	Flexible microstrip array antenna (2 × 2)	2.46 (120 MHz BW)	$1 \times 10^6\ \text{S m}^{-1}$	-40.28	6.78 dB	[59]
Copper on polyimide	Flexible hybrid shaped patch antenna (30.4mm × 38mm)	3.5, 6.7, 12	-	>1.69	1.69 dBi	[139]
Graphene ink on PDMS	Flexible circularly polarized patch antenna (13.9 mm × 14 mm) over AMC	5.8 (1.4 GHz BW)	$1.13 \times 10^6\ \text{S m}^{-1}$	-37.5	6 dBic	[113]
Copper on RT/Duroid 5880 or Wangling Ltd.	Diode reconfigurable circularly polarized antenna array (1 × 4) over AMC	1.65 (350 MHz BW)	-	< -10	13 dBic	[140]
Copper on Teflon (Graphene assisted)	Tunable slot antenna (25 mm × 15 mm) with graphene ink extension	2.83– 6	-	< -10	-1.7 dBi	[78]
Copper on PCB (Graphene assisted)	Tunable patch antenna with biased graphene ink stub	5.05, 4.5	$< 100 - > 1\ 000\ \Omega\ \square^{-1}$	< -20	2.38 dB	[79]
Copper on PCB (Graphene assisted)	Beam steering (± 16 °) phased array with biased CVD graphene phase shifter	4.5	$580 - 2\ 500\ \Omega\ \square^{-1}$	-20	3.3 dB (V_{bias} = 0.7 V)	[128]
Copper on PCB (Graphene assisted)	Beam steering (90 °, 270°) dual Vivaldi printed antenna with biased graphene nanoplate resistors	30	-	< -10	3.8 dBi	[141]

Tang et al. [122] investigated the sensitivity of graphitic film-based patch antennas and their behavior under bending conditions. Here, the sensitivity is defined as $S = (\Delta f / f_0) / \Delta\xi$, where Δf is the frequency deviation in the bent state from the resonant frequency at rest f_0 and is defined as $\Delta f = f - f_0$ and $\xi = (\pm) h/2r$ is the bending strain, which is dependent on the thickness h of the substrate and the bending radius r. Similar to previous findings, bending the antenna resulted in a shift of the antenna's resonance frequency. The resonance frequency decreased as the bending angle increased. Their experimental results matched their simulations well. More importantly, an evaluation of the antenna's sensitivity showed the designed antenna had a sensitivity of 9.8, which is higher

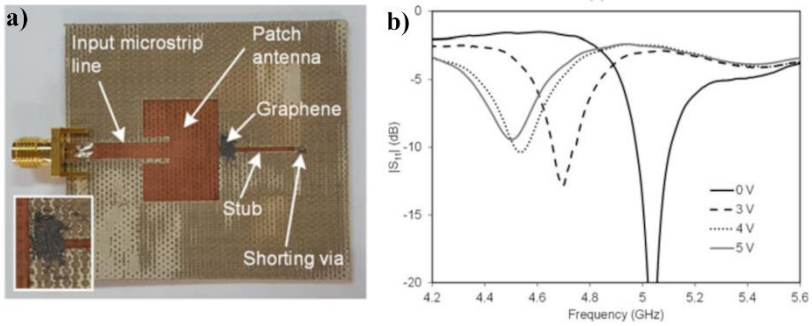

Figure 15. Experimental evaluation of tunable graphene-assisted metal patch antenna. (a) The fabricated copper patch antenna is connected to a stub via a graphene-flake-based patch. (b) Measured reflection coefficient under different graphene patch biasing conditions. © 2017 IEEE. Reprinted, with permission, from [79]

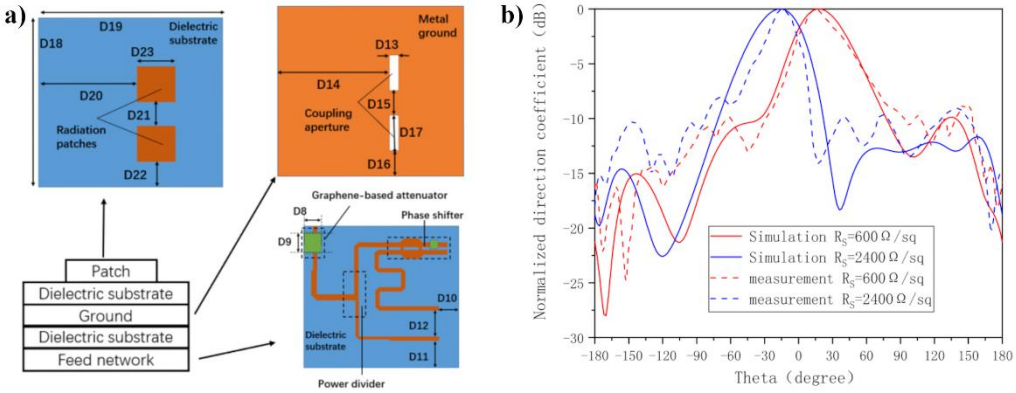

Figure 16. Graphene-assisted antenna design. A graphene-based capacitor coupled phase shifter is used for phase modulation. (a) Schematic representation of the proposed antenna. (b) Comparison of simulated and measured far-field radiation patterns in the azimuth plane of the antenna under (blue) 0.7 V and (red) 5 V biasing and the respective surface resistances of graphene. © 2020 IEEE. Reprinted, with permission, from [128]

than that of a comparable copper antenna with a sensitivity of 5.39.

In a later study, Zhang et al. [80] increased the sensitivity of graphitic film-based antennas to 35.6 using a poly-based substrate and a smaller antenna design. Their results show the possibility for graphitic film-based antenna applications in human health or motion detection, as illustrated in figure 14. Whether the variation of the antenna parameters due to bending is beneficial or not is dependent on the specific application. Nonetheless, there are a number of applications for which a change in performance because of bending is not acceptable. Thus, a separate tuning technique would be required. For example, Chen et al. [78] designed a metal microwave slot antenna tuned using a graphene ink patch simply placed at one end of the metallic slot. The graphene ink was made of a mixture of commercially purchased graphene flakes and GO, where the GO acted as a binder in the ink solution. Application of a DC voltage to the two ends of the graphene ink patch resulted in a reduction of the GO due to the removal of oxygenated functional groups and led to a reduction of the resistance of the graphene ink patch [78]. This change caused a variation of the equivalent length of the slot and, with it, a resonance shift. While the approach was not demonstrated on flexible antennas, the use of GO inks for flexible antennas has been demonstrated previously in [121].

Owning to the possibility of depositing thicker layers of graphene ink, the introduction of rolling compression, and the use of binder-free graphene inks, graphitic films with metal-like conductivities can be fabricated. These techniques could resolve the issue of high impedance dominating EG microwave antennas. Graphitic films are particularly well-suited for lightweight, flexible, wearable antenna applications due to their superior robustness when compared to metallic films. Moreover, they are low-cost and readily available. Further improvements in the composition of graphene ink could further improve the current issues as well as its adhesion properties to various materials.

3.1.1.3 Graphene-Assisted Tunable Antennas

As was introduced in Sec. 3.1.1.2 using the example from [78], metallic antennas can be designed to exhibit dynamic tunability by linking them with graphene or graphene-derived devices. These antenna designs are sometimes called graphene-metal-hybrid antennas. Various metallic antennas

that have been combined with patches made of either graphene flakes [78, 79, 141] or CVD graphene [125], or CVD graphene-based capacitors [127, 129] have been demonstrated.

Yasir et al. [79] connected the metallic patch antenna to a stub using a graphene flake-based patch and varied the current that flowed through it by applying a voltage to the patch. The resonance frequency shifted from 5.05 GHz in the unbiased state to 4.5 GHz with 5 V applied to patch as shown in figure 15.

Wang et al. [128] realized a beam-direction reconfigurable antenna array using a CVD graphene capacitor-based reflective phase-shifter. Phase shifters are commonly employed in phased arrays to steer the beams they radiate. The prototype array consisted of two metallic radiating patches and a planar microstrip feeding network separated by two dielectric layers. A slotted ground plane was sandwiched between the two dielectric layers and was used to exploit an aperture-coupling technique. One microstrip feedline is directly connected to a radiating patch following a power divider, while the other passes through the reflective phase shifter. The graphene-based phase shifter consists of a traditional metallic analog phase shifter linked with a CVD graphene-based capacitor that is placed on one of the termination circuit arms. Application of a bias voltage to the graphene capacitor changes its capacitance, which results in a change in the reactance of the termination circuit of the phase shifter. Consequently, a phase shift in the feeding line occurs. Applying 0.7 V and 5.0 V bias voltages to the graphene-based capacitor changed the main beam direction in the azimuth plane from 16 ° to −16 °, see figure 16.

Phased arrays are a common engineering electromagnetics research area, and they find regular application in numerous communication and defense applications [87]. Ferrite elements are commonly used as phase shifters in the microwave range [87]. The radiation pattern and polarization of microwave antennas are readily reconfigured, for instance, using RF switches such as MEMS [142] or diodes [140, 143]. These approaches have been designed while striving to maintain relatively high radiation efficiencies [143]. A comparison of several graphene and non-graphene-based microwave antennas is given in table 1.

Using graphene ink or graphene-based devices for microwave antenna reconfiguration, e.g., as an RF switch or phase shifter, has not yet received much attention. It would require some extensive research. In particular, their cost, manufacturability, and most importantly, their influence on the radiation efficiency needs to be determined.

The use of metal in conjunction with graphene, e.g., at graphene metal contacts for biasing or feeding the EM wave emitters, has previously shown to result in large contact resistances [144]. This has been identified as an issue, particularly in GFET applications, as it hinders the achievement of significant gain values [145, 146], and reducing the contact resistance can significantly improve their performance [146]. This can be achieved in various ways, with the most prominent one being the use of high work-function metals, i.e., nickel [144, 147] or platinum [146], and the use of edge contacts [144, 147]. Jiang et al. [147] managed to reduce the contact resistance down to $4 - 8\ \Omega\ \mu m$ using nickel and edge contacts.

The effect of metal contacts in antenna applications has not been studied to date. However, they have been previously shown to reduce the transmission properties of graphene-loaded transmission lines [148]. The contact resistance is proportional to the contact dimensions, which could pose an issue in the THz region. However, it is generally not considered.

3.1.2 Terahertz Antennas

Metals used in microwave antennas suffer from a degradation of their conductivity and a reduction of the skin depth in them at frequencies in the THz range. The former can lead to low radiation efficiencies, while the latter causes high propagation losses [17, 149]. Graphene is commonly envisioned to help overcome these challenges and enable wireless communication at the nanoscale.

The EM wavelength reduction associated with SPPs in the THz frequency range permits designing graphene antennas with a significant size advantage compared to metallic ones [24, 150]. This is another main reason why the main focus in graphene research regarding antennas lies in the THz range. Graphene's dynamic tunability can be used to reconfigure several antenna properties. These include the resonance frequency [17, 24, 114], directivity [85, 149], and radiation pattern [85, 116]. All simulation models of THz antennas have been based on the Drude conductivity model introduced in 2.2. Researchers mainly focus on three types of antennas when designing graphene-based antennas to generate THz EM fields: resonant antennas, Yagi-Uda, and leaky wave antennas. Their working principles are quite different and thus need to be considered separately.

3.1.2.1 THz Resonant Antennas

The main graphene-based resonant antenna concepts used by researcher to date have been dipole [24, 33, 115, 151, 152], patch [114, 115, 150, 153-157], and bowtie [158] antennas. They are generally easy to design and fabricate due to their planar designs. Tunability in simulations is achieved by varying the chemical potential within graphene's conductivity model. Given the variations in the actual properties of a realistic graphene component, it is crucial that researchers use conservative values that can realistically be achieved using common biasing concepts. For unbiased graphene, the chemical potential of $\mu_c = 0 - 0.2$ eV and a relaxation time of

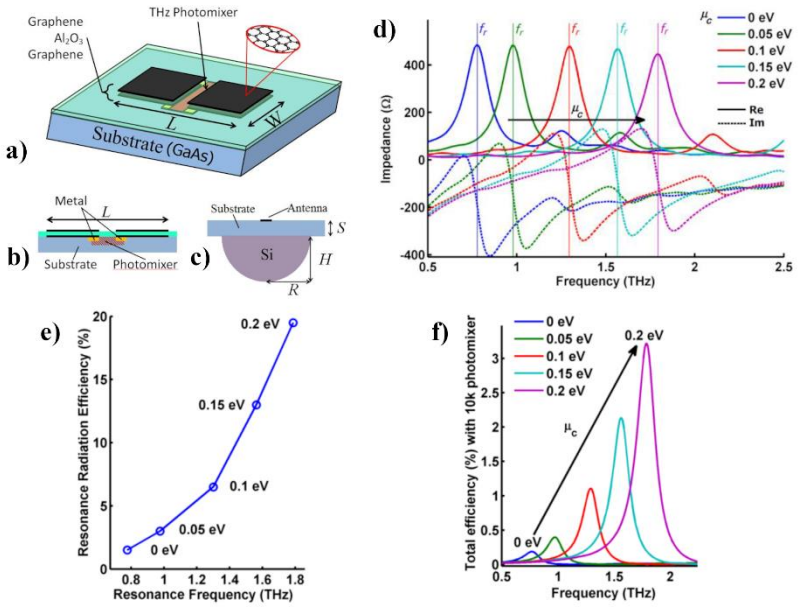

Figure 17. Photomixer-coupled two-layer graphene stack dipole antenna. (a-c) Schematic diagram of the antenna including the photomixer and backside silicon lens. (d) Real and imaginary parts of the graphene antenna's input impedance and its dependence on the chemical potential. (e-f) Simulated (e) resonance radiation efficiency and (f) total antenna efficiency. Reprinted from [24], with the permission of AIP Publishing.

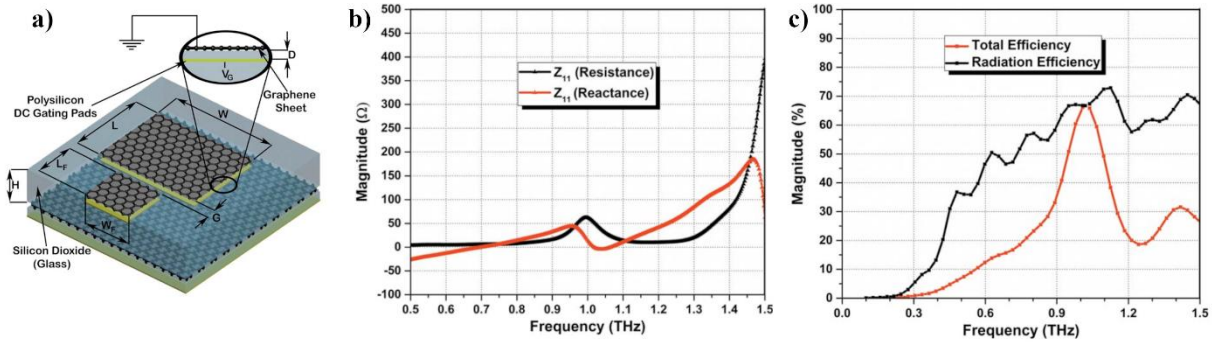

Figure 18. 50 Ω capacitively-coupled graphene patch antenna on a glass substrate. (a) Schematic diagram of the antenna including a polysilicon pad for biasing. (b) Antenna's frequency dependant input impedance. (c) Antenna's radiation and total efficiency. Reprinted with permission from [114]. Copyright 2018 John Wiley and Sons.

$\tau = 0.5 - 1$ ps are often chosen because they give a good representation of real graphene [17, 20, 24].

At the same time, the methods intended for manufacturing and controlling the device, including any biasing structures, must be considered in a realistic design. A critical consideration in designing graphene THz antennas is their high input impedance resulting from their very small thickness. Researchers suggest combining antennas with photomixers to realize Thz emissions [24, 149, 151]. This approach is one of many so-called photoconductive antennas (PCA). A PCA requires a femtosecond laser as its source. The laser beam is directed onto a photoconductive material. The relaxation times of the photo-currents induced in this material and, hence, the conductive regions connected to it occur in the THz regime.

Tamagnone et al. [24] designed a plasmonic dipole antenna using a two-layer graphene stack. Due to the already noted high input impedance of graphene antennas, they can be easily matched to THz photomixers. This was considered in their design shown in figure 17. Although no information about the photomixer implementation was given, it could have been easily fabricated using CVD graphene. It was demonstrated that increasing the chemical potential resulted in a higher conductivity and thus positively affected the radiation efficiency owing to the antennas becoming electrically larger at resonance. The total efficiency, including the photomixer, was $0.25 - 3.2$ %. The authors state that comparable metallic implementations achieve total efficiencies of ~20 % but lack tunability, are generally narrowband, and are roughly $20\times$ larger.

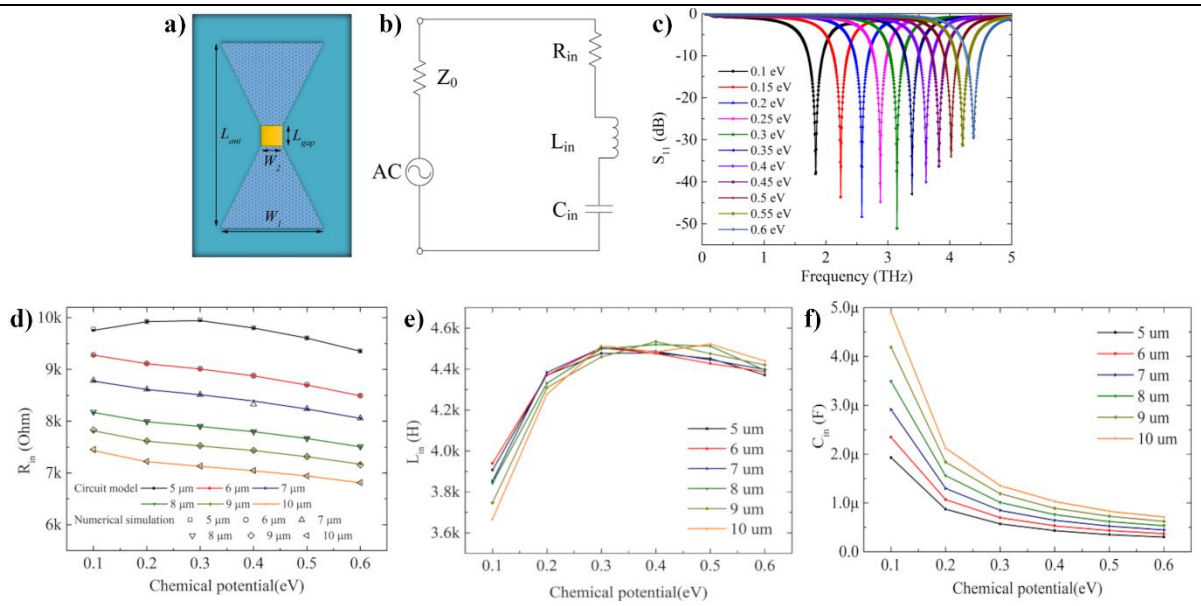

Figure 19. Equivalent circuit modeling of the graphene-based bowtie antenna. (a) Schematic representation of the photomixer-excited bowtie antenna on a quartz substrate. (b) Equivalent circuit of graphene bowtie antenna resulting from the coupled-resonator approach. (c) Dependence of the reflection coefficient on the values of graphene's chemical potential. (d-f) Comparison of the RLC parameters of the circuit model with full-wave simulation results: (d) R_{in}, (e) L_{in}, and (f) C_{in}. [158] © 2018, CC BY 4.0. To view a copy of this license, visit http://creativecommons.org/licenses/by/4.0/

The high input impedance of graphene antennas is often seen as a drawback as many RF sources are currently designed with an output impedance of 50 Ω. Goyal and Vishwakarma [114] designed a graphene-based patch antenna on a SiO_2 substrate that was capacitively coupled to a waveguide via a gap between the graphene patches, as shown in figure 18. By optimizing the gap width G, the patch antenna input impedance was set to 50 Ω. Polysilicon was used to bias the graphene patch and to achieve tunability. Previous simulations had shown that the polysilicon layer does not affect antenna performance characteristics [114]. Because of their specific setup, the antenna was narrowband, i.e., the graphene has an inductive reactance at THz frequencies, and the coupling gap G produced a capacitive reactance. The antenna resonance frequency was tuned within $959.39 - 1028.03$ GHz by variying the chemical potential between $0 - 0.45$ eV. However, the obtained tunability was rather low. The antenna was compared to a copper one with equal dimensions. The graphene antenna resonated at 1.0193 THz; has directivity and gain of 6.82 dB and 5.08 dB, respectively, and radiation efficiency of 66.72 %. The copper antenna resonatees at 1.0541 THz; it had a directivity and gain of 6.92 dB and 6.05 dB, respectively, and a radiation efficiency of 82.67 %. As expected, the graphene antenna resonated at a lower frequency than the copper antenna, although the difference is small. The differences in gain and radiation efficiency were expected and caused by graphene's high reactance.

A similar comparison of the resonance frequency of a graphene and copper antenna was given by Dash and Patnaik in [156]. They designed a circular off-center fed planar graphene antenna on a Si substrate with a metallic backplane. The design was well matched to a 50 Ω input impedance, and biasing was envisioned to be implemented via the backplane. Very high voltages would be needed due to the thickness of the substrate. The graphene antenna design resonated at 0.75 THz with a ultra-wideband (UWB) impedance bandwidth of 370 % (≈ 2.8 THz). The SPP wavelength at resonance was 10 × smaller than the free-space wavelength. A comparable copper antenna resonated at 1.25 THz and is narrowband with a 2 % (≈ 0.2 THz) bandwidth.

Dash and Patnaik [17] also compared the resonance frequencies of graphene, CNT, and copper-based dipole antennas with equal dimensions. The antennas were designed with a length of $L = 71$ μm on top of SiO_2 substrate. The graphene, CNT, and copper antennas had resonance frequencies of 0.81, 1.42, and 1.9 THz, as well as directivities of 4.5, 3.5, and 2.2 dBi, respectively. The difference in resonance frequency of the graphene-based implementation and its metallic counterpart is much larger in [17, 156] when compared to the value in [114]. Nevertheless, all cases verified the possibility of antenna miniaturization

Bowtie antennas are a planar variant of biconical antennas and generally consist of triangular radiating patches that permit wideband operation [87]. Zhang designed a graphene-based bowtie antenna in [158]. Two quasi-triangular graphene patches were placed on a quartz substrate, as illustrated in figure 19(a). It was envisioned to be excited by a photomixer for optimal matching.

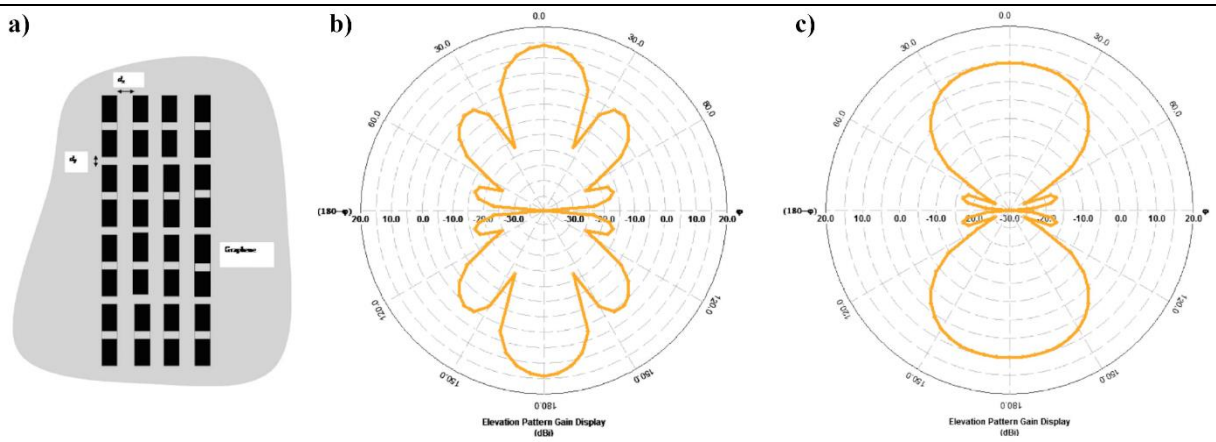

Figure 20. Graphene-metal hybrid antenna. (a) 4×4 antenna array based on gold dipole antennas structured on top of graphene on a SiO_2/Si substrate. (b-c) The radiation pattern of the array if (b) all antennas in the 4×4 array operate in their 'On' states, and (c) the first and fourth row of antennas are in their 'Off' states, and the remaining ones are in their 'On' states. Reprinted from [116], with the permission of AIP Publishing.

The antenna was initially modeled using full-wave simulation tools. Figure 19(c) shows the resonance frequency shifts when the chemical potential of graphene varies. While the bandwidth was not affected, it is clear that the graphene-based bowtie antenna model is narrowband. It had a -10 dB bandwidth of < 10 %. The currents predominantly propagate towards the source owing to the antenna dimensions and the dielectric behavior of graphene at low values of chemical potential [158].

Since the antenna resonates at a single frequency, it can be modeled using an equivalent, simple RLC circuit (see figure 19(b)). The antenna is treated as a coupled-resonator, and its resonance is determined from its unloaded quality factor Q_a and coupled quality factor Q_0. This approach was initially used for superconducting resonators [158]. The calculated values of the RLC equivalent circuit are compared to the extracted ones from full-wave simulations in figures 19(d-f). The results show good impedance matching.

Single element antennas generally offer wide, fixed radiation patterns with low directivity [130]. However, there are many applications that require reconfigurable radiation patterns and high directivity. A simple way to attain these properties is to use an antenna array. The radiation pattern of an antenna array can be controlled by the geometrical layout and spacings of the individual antenna elements, as well as their amplitudes and phases [130].

To the best of our knowledge, one of the first considerations of graphene-based array antennas for radiation pattern reconfiguration was reported by Dragoman et al. in [116]. They evaluated the possibility of manipulating the radiation pattern of a graphene-assisted gold dipole antenna without using graphene as the main radiating body. In their design, graphene covered a SiO_2/Si substrate, and the gold antennas were printed on top of the graphene. By varying the chemical potential of the graphene underneath each dipole antenna, their fields were individually turned 'On' or 'Off'. However, it is not clear how graphene was biased. Instead, typical resistivity values for graphene for the two states were assumed. The 120 µm long dipoles resonated at $f_r = 1.05$ THz and had a directivity of 2.72 dBi in their 'On' states when electrostatic biasing was applied, and $-43\ dBi$ in their 'Off' states when it was not applied. They demonstrated a radiation efficiency of 95.80 % and an antenna efficiency of 89.14 %. Using a 4×4 array of dipole antennas and dynamically changing the 'On' and 'Off' states of individual antennas allowed them to vary the directivity and radiation pattern of the array, as shown in figure 20.

In summary, the dynamic reconfigurability of the resonance frequency and radiation patterns using graphene's tunability has been demonstrated with graphene-based resonant THz antennas. They generally operate with much wider bandwidths in comparison to comparable metallic implementations, and their use of SPP resonances facilitate them being significantly electrically smaller, up to 20 × smaller. However, their radiation efficiencies suffer from SPP dispersion losses. Operating resonant graphene THz antennas outside of the SPP range could improve the antenna performance but at the cost of reconfigurability and size, as suggested in [101]. Moreover, because of the high surface impedance of graphene, the antennas need to be designed carefully to be matched to 50 Ω sources. Alternatively, high impedance photomixers can be used to significantly simplify the matching process. Nevertheless, this further diminishes the total antenna efficiency as THz photomixers still suffer from low conversion efficiencies and low output powers [24, 159].

Table 2 gives an overview of several graphene and non-graphene implementations of THz resonant antennas.

3.1.2.2 Yagi-Uda Antennas

Table 2. Comparison of THz resonant antenna implementations

Technology	Design	Operation Frequency [THz]	Return Loss [dB]	Directivity (Gain)	Radiation Efficiency [%]	Ref.
Metal on various substrate	THz antennas ($r = 100$ μm) on photonic bandgap based crystal polyimide	$0.626 - 0.63$ (BW of $26.47 - 29.79$ GHz)	-28.49 to -59.15 dB	$8.9 - 10.1$ dBi ($8.34 - 9.45$ dB)	$82.6 - 90.6$	[163]
Graphene on polyimide	GNR patch antenna (88.98 μm × 133.2 μm)	0.75	< -35dB	5.71 dBi (5.09 dB)	86.58	[153]
Graphene on Si	Circular planar antenna ($r = 22$ μm)	0.75 (2.8 THz BW)	-28 dB	5 dBi	-	[156]
Graphene on SiO_2	Dipole antenna (71 μm)	0.81	-39 dB	4.5 dBi	-	[17]
Copper on SiO_2	Capacitive coupled patch antenna (60 μm × 100 μm)	1.0541 (77.43 GHz BW)	-	6.92 dBi (6.05 dB)	82.67	[114]
Copper on Si	Circular planar antenna ($r = 22$ μm)	1.25 (0.2 THz BW)	-12.5 dB	-	-	[156]
CNT on SiO_2	Dipole antenna (71 μm)	1.42	-25 dB	3.5 dBi	-	[17]
Copper on SiO_2	Dipole antenna (71 μm)	1.9	-20 dB	2.2 dBi	-	[17]
Gold on graphene on SiO_2/Si	Switchable gold dipole antenna (120 μm) on large area graphene	1.05	-	'On': 2.72 dBi 'Off': -43 dBi	95.8	[116]
Graphene on Al_2O_3 on GaAs	Tunable plasmonic dipole PCA (11 μm × 7 μm)	$0.8 - 1.8$ ($\mu_c = 0 - 0.2$ eV)	-	-	$2 - 20$	[24]
Graphene on SiO_2	Tunable capacitive coupled patch antenna (60 μm × 100 μm)	$0.96 - 1.03$ (~80 GHz BW) ($\mu_c = 0 - 0.45$ eV)	-24 to -39.2 dB	6.82 dBi (5.08 dB)	66.72	[114]
Graphene on quartz	Tunable bowtie PCA (12 μm × 5 μm)	$1.8336 - 4.3825$ ($\mu_c = 0.1 - 0.6$ eV)	-29.5 to -51 dB	-	-	[158]
ITO on glass	Transparent patch antenna (95 μm × 147 μm)	2.15 (2.3 THz BW)	-32 dB	4.97 dBi	79.6	[164]

Yagi-Uda antennas are a type of low-profile traveling wave antenna consisting of an excitor, a reflector, and a director region. A printed PCA version is shown in figure 21. The excitor is generally an exited dipole antenna. Then the reflector and directors are also generally dipole elements. The length of the reflector is slightly larger than the excitor. The director region consists of an array of same-length uniformly spaced dipole elements, their lengths being shorter than the excitor. The coupling between the elements hampers wideband operation [87]. Yagi-Uda antennas are generally used in high directivity/gain applications. In contrast to related frequency-independent log-periodic arrays, the bandwidth is sacrificed to achieve the higher gains.

Graphene-based Yagi-Uda antennas [85, 117, 149, 160-162] are a common research topic for various high-gain applications. The main focus herein lies in the THz frequency range where the plasmonic effects occur, and dynamic tunability is facilitated.

Nissiyah and Madhan [149] designed a graphene-based Yagi-Uda PCA. They initially designed a 1 Thz photomixer-coupled graphene-based dipole antenna and compared the emission intensity to a metallic dipole realized with gold. The improvement of the emission intensity attained by the graphene antenna was expected because of the higher mobility and longer mean free path. The graphene dipole PCA was further extended to a planar Yagi-Uda PCA by introducing the reflector and several director patches shown in figure 21(a). The directivity and gain of the Yagi-Uda PCA were 9.57 dB and 8.64 dBi respectively. Comparing those values with the 6.77 dB directivity and 4.88 dBi gain of the graphene-based PCA highlighted the benefit of using a Yagi-Uga antenna design. The emission spectrum of the Yagi-Uda antenna shifts towards lower frequencies and is narrower, as figure 21(b) indicates.

Hai-Qiang et al. [85] extended the use of Yagi-Uda antennas to an array of them. Three graphene-based director regions with an angular spacing of 60 ° were coupled to one metal radiating patch to form three Yagi-Uda antennas. Biasing each graphene director array changes the director dipoles' conductivity and enables or disables the emission in a particular direction. Figure 22 shows this system and illustrates how individual director arrays or neighboring ones are enabled, resulting in reconfigurable radiation patterns.

Luo et al. [117] used a similar approach and extended it to cover a full 360 °, in 60 ° increments. Six Yagi-Uda arrays were realized in a hexagonal arrangement with six pairs of

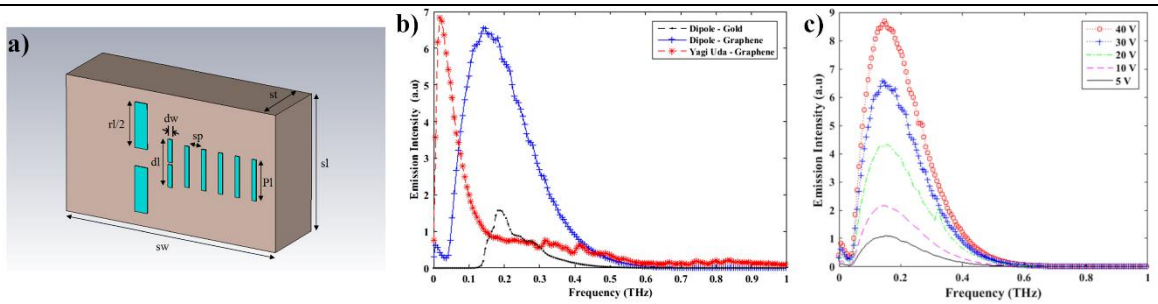

Figure 21. Graphene-based Yagi-Uda photoconductive antenna. (a) Schematic representation of graphene-based Yagi-Uda antenna on a GaAs substrate. (b) Comparison of emission intensity of graphene and gold dipole and the graphene-based Yagi-Uda photoconductive antennas. (c) Comparison of the emission intensities for different biasing conditions (recall that higher voltage results in higher chemical potential). Reprinted by permission from [149]. Copyright 2018 Springer Nature.

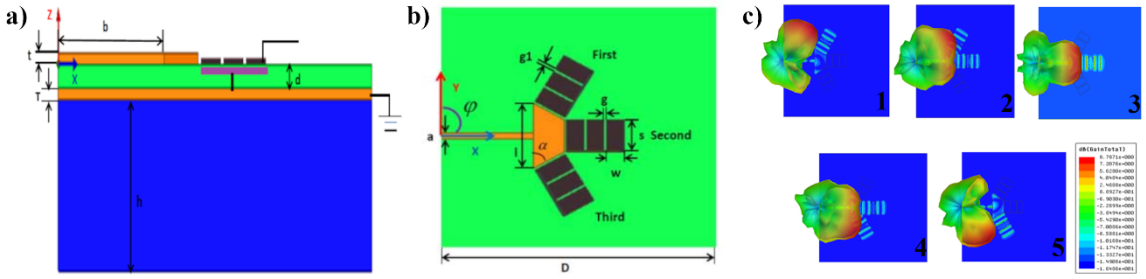

d)

The group which is applied by 15V	First	First Second	Second	Second Third	Third
Minimum return loss(dB)	-35dB	-23dB	-38dB	-23dB	-35dB
-10dB Return Loss Bandwidth	7%	9.2%	7.1%	9.2%	7%
Peak Gain(dB)	6.8	7.79	7.56	7.79	6.8
Deflection Angle (φ)	50°	30°	0°	-30°	-50°
Efficiency	91.2%	92.7%	92.3%	92.7%	91.2%

Figure 22. Graphene-Metal hybrid Yagi-Uda antenna with a reconfigurable radiation pattern. (a) Schematic representation of its vertical profile, including the biasing structure. (b) Top-view of the antenna showing three 60 ° separated graphene-based director patch arrays. (c) 3D radiation patterns for five (1-5) operating states: (1) only top antenna, (2) top and middle antennas, (3) only middle antenna, (4) middle and bottom antennas, and (5) only bottom antenna in operation. (d) Table of antenna parameters for those five (1-5) operation conditions. © 2015 IEEE. Reprinted, with permission, from [85]

reflectors and directors excited by three driven dipole elements arranged symmetrically around the point feed with angular spacings of 60 ° between the arms. The operations of the reflector and director elements were switched by adjusting their chemical potentials.

3.1.2.3 Leaky Wave Antennas

LWAs are a type of traveling wave antenna introduced in 1940 [87]. In contrast to resonant antennas, the EM wave is guided along a specified direction without reflections. Designs have achieved high directivity, narrow beamwidth radiation patterns, and broadband frequency responses [86, 88, 101, 109, 165-168]. As noted previously, they also offer frequency-based and fixed frequency beam scanning capabilities. Their planar versions are generally easy to fabricate, and they do not require complex feeding networks [87].

LWAs are generally classified in terms of their geometric properties or operating principles. Distinctions are made between their uniform or periodic guiding structures, modulating elements, and the number of dimensions of the guiding structure. Thus, the main LWA types are one-dimensional (1D) uniform/quasi-uniform, 1D periodic, 2D uniform/quasi-uniform, and 2D periodic [87].

The most straightforward representation of a 1D LWA is a slotted rectangular waveguide. It is a uniform LWA because the guiding structure, the waveguide, is the same (uniform) at every point along the direction of propagation. The feed point is placed at one extremity of the waveguide and is terminated with a matched load at the other end. Thus, the EM wave propagates in one direction along the structure.

It is a fast-wave system because the EM wave has a phase velocity greater than the speed of light in the waveguide: $v_{\mathrm{ph}} > c_{\mathrm{g}}$. The longitudinal wavenumber $k = \beta - \mathrm{i}\alpha$ of EM

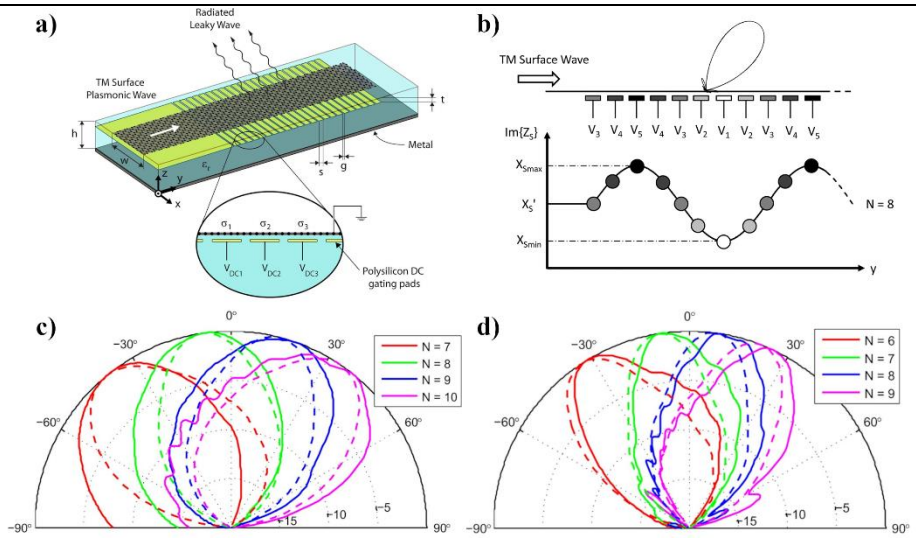

Figure 23. Graphene microstrip-based tunable leaky-wave antenna. The graphene strip is sinusoidally biased to achieve desired reactance profile. (a) Schematic diagram of the leaky-wave antenna. The conductivity of the graphene strip is modulated via electrostatic biasing using polysilicon pads below the graphene strip to achieve the emission of leaky modes. (b) Biasing profile: Dependence of surface reactance on biasing voltage. (c, d) Comparison of the radiation pattern from full-wave simulation (solid lines) and leaky-wave antenna theory (dashed lines) for different relative permittivity substrate: (c) $\epsilon_{\mathrm{r}} = 3.8$ and (d) $\epsilon_{\mathrm{r}} = 1.8$. © 2014 IEEE. Reprinted, with permission, from [118]

waves traveling in a realistic waveguide is complex due to the radiation losses of the leaky modes and the conduction losses in the waveguide walls [87]. The slots in one wall of the waveguide modulate the propagating wave and allow energy to leak out of the waveguide. The combination of the emitted fields have their maximum pointed at an angle in the forward direction in this case, i.e., the direction that the EM wave is propagating in the waveguide. The accumulation of these radiation losses determines a LWA's performance characteristics. They are directly related to the wavenumber of the traveling wave. In particular, the angle of the maximum direction of the emitted fields with respect to the broadside direction ($\theta = 0\,°$), which is perpendicular to the waveguide face containing the slots, is defined as $\sin(\theta_{\mathrm{m}}) = \beta/k_0$, where k_0 is the free-space wavenumber. Variation of the beam angle in the elevation plane can be achieved within $0\,° < \theta_{\mathrm{m}} < 90\,°$, i.e., between the broadside and end-fire directions. It can be varied because the phase constant β is dependent on the frequency [87]. The effect of using the frequency to steer the maximum direction of the emitted fields is referred to as frequency scanning. Variation of the attenuation constant α, on the other hand, directly influences the beamwidth. Large values of α result in wide beams, while small ones yield narrower ones.

Periodic modulations of a uniform slow-wave waveguide ($v_{\mathrm{ph}} < c_{\mathrm{g}}$) also result in a continuously radiating structure creating a fast wave LWA. Because of the periodicity, the modes of the structure can be described with Floquet theory. The wavenumber of those in the direction of propagation is described by $k_n = \beta_n - \mathrm{i}\alpha_n = k_f + 2\pi n/p$, with n being the n-th order space harmonic, p being the period of the modulations, and k_f being the wavenumber of the fundamental Floquet wave [87]. The overall emanation results from the summation of the fields emitted by the individual Floquet waves interacting with the periodic perturbations. A higher-order space harmonic, often $n = -1$, is designed to be a radiating fast wave such that $-k_f < \beta_n < k_f$. The radiation direction can thus be extended into the backward direction as well with the angle of maximum direction reaching $-90\,° < \theta_{\mathrm{m}} < +90\,°$.

Quasi-uniform LWAs operate similar to uniform ones as their fundamental mode is still a fast wave. However, the periodic structures that modulate the waveguide create an infinite set of space harmonics. Their period p is generally chosen so that only the $n = 0$ space harmonic radiates.

The 2D LWAs consist of guided structures that support waves that can propagate in more than one direction. With a proper design of the elements that yield a 2D modulation of one of its 2D surfaces, they can produce pencil or cone-shaped beams in the radial direction away from a source in the guiding structure [87]. A graphene-based 2D LWA example is shown in Fig 25. By varying the periodic nature of the modulations, e.g., by varying the chemical potential to change the period p and, hence, k_n, the main direction of the emitted fields, i.e., the main beam direction, can be scanned at a fixed frequency.

Similar to resonant THz antennas, graphene-based LWAs benefit from graphene's electrical properties at THz frequencies, especially its tunability. In particular, these properties facilitate both frequency scanning of the main beam

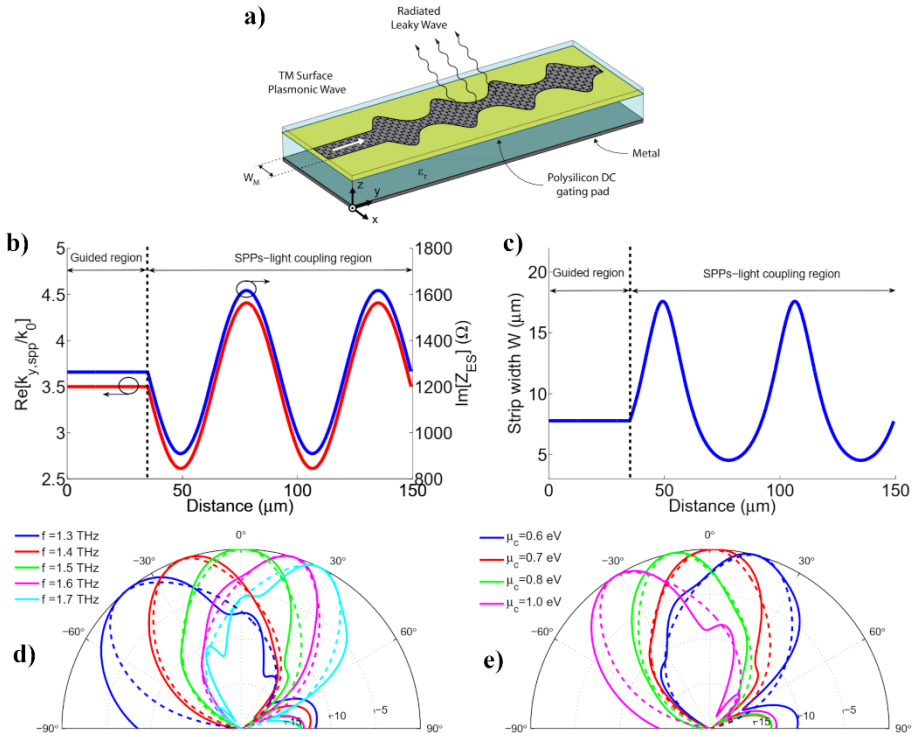

Fig 24. Graphene-based tunable leaky-wave antenna. (a) Schematic diagram of periodically width modulated graphene waveguide for the emission of leaky modes. (b) Normalized phase constant and surface reactance along the y-axis, the long direction of the waveguide. (c) Non-sinusoidal profile of the graphene strip width along the y-axis. (d, e) Comparison of the radiation pattern from full-wave simulation (solid lines) and leaky-wave antenna analytical theory (dashed lines) to visualize scanning capabilities: (d) frequency scanning of the beam and (e) beam scanning at a fixed frequency $f = 1.5$ THz. Reprinted by permission from [86]. © 2013 Optical Society of America.

direction [86, 118] or scanning the main beam (beam scanning) at a fixed frequency [86, 101].

The first graphene-based LWAs were introduced in [86, 118] by the same research group. Esquius-Morote et al. [118] used the principle of a sinusoidally modulated reactance surface for their design, first introduced by Oliner and Hessel in 1959 [165]. The 1D LWA consisted of a periodically arranged set of polysilicon pads that created a grating on a back-metalized SiO_2 substrate. The fabrication process was described in detail. A graphene strip is transferred onto the structure and separated from the polysilicon using the same oxide. The resulting LWA is shown in figure 23(a). Sinusoidal modulation of the reactance is achieved using the tuning ability of graphene's surface conductivity by sinusoidally biasing the graphene using the polysilicon gates, as depicted in figure 23(b). The surface reactance of the graphene strip along the y-axis is given by $X_s = X_s'[1 + M\sin(2\pi y/p)]$, with X_s' being the average surface reactance, M the modulation index, and p the period. The reactance X_s' directly affects the phase constant β while M determines the attenuation constant α. These properties can be used for quasi-independent modulation of the beamwidth and beam angle θ. Tuning the chemical potential of the graphene in a range of $0 - 0.8$ eV was achieved with a biasing voltage of 45 V, and the period of the sinusoidal reactance modulation was changed with the number of polysilicon pads N. Figure 23(c, d) shows how a variation of N results in beam scanning at a fixed frequency. The radiation patterns were calculated using both full-wave simulations and LWA analytical theory [87]. A radiation efficiency of about 11 % was achieved, although increased biasing voltages and improved modulation of the graphene surface conductivity are expected to result in higher radiation efficiencies [118].

Gómez-Díaz et al. [86] also sinusoidally modulated the reactance of a graphene strip to create a LWA. Instead of periodically biasing the graphene, its width was periodically widened and narrowed to modulate the strip's reactance. The relation of surface reactance and strip width is non-linear, and thus the change in width does not follow a sinusoidal relation. Figure 24(a) shows how a single polysilicon layer underneath the graphene is used for electrostatic biasing of the whole graphene strip. Biasing of graphene has a strong influence on the plasmon-light coupling angle, rate, and efficiency. Therefore, beam scanning at a fixed frequency is enabled by dynamically changing the biasing voltage. The LWA also operates at various frequencies and permits frequency scanning, as shown in figures 24(d-e).

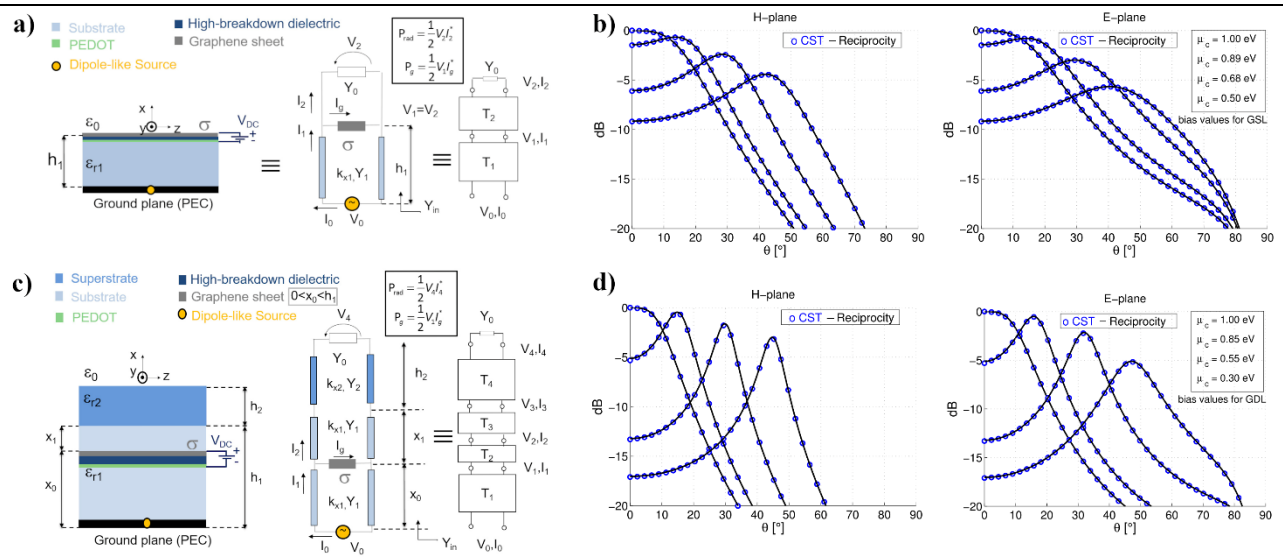

Figure 25. Fabry-Pérot cavity-based graphene leaky-wave antenna. (a) Vertical profile, transverse electric network model, and ABCD-matrix representation of the graphene-based single-layer antenna. (b) Comparison of the radiation patterns calculated with full-wave simulations and the analytical transverse electric network model of graphene-based single-layer. (c) Vertical profile, transverse electric network model, and ABCD-matrix representation of the graphene-based double-layer antenna. (d) Comparison of the radiation patterns calculated with full-wave simulations and the analytical transverse electric network model of the graphene-based double-layer. © 2017 IEEE. Reprinted, with permission, from [101]

Fuscaldo et al. [101] placed a single graphene sheet inside a grounded dielectric multilayer stack to form a Fabry-Pérot cavity (FPC) 2D LWA. The complex wavenumber of the SPPs and their attenuation constant in graphene depend on its conductivity. The dispersion losses thus need to be considered when designing graphene-based tunable structures. It was reported that the losses increase with the frequency, decrease with increasing chemical potential μ_c, and decrease with increasing relaxation time τ. The SPP dispersion losses resulted in low radiation efficiencies. Hence, ordinary (non-plasmonic) propagating leaky modes were excited. Two separate graphene-based 1-THz FPC-LWA were designed – a graphene-based single layer (GSL) and a double layer (GDL) antenna. Here the terms 'single' and 'double' refer to the number of dielectric layers with the graphene layer being placed on top of the dielectric in the GSL antenna and sandwiched between the dielectric layers in the GDL antenna. The top dielectric layer of the GDL acts as a dielectric superstate ($\epsilon_2 \gg \epsilon_1$). Both antenna designs incorporate a polymer sheet, i.e., PEDOT, for biasing. The configurations of the two systems are shown in figure 25. Simulation of the transverse electric (TE) and TM leaky modes in the E-plane and H-plane, respectively, were performed using the reciprocity theorem and transverse electric network (TEN) model [169], as well as full-wave simulations.

Even though the radiation efficiency of the GSL antenna at $f_{\mathrm{r,GSL}} = 0.922$ THz was $RE_{\mathrm{GSL}} \approx 70$ %, it had a low directivity. Comparing figures 25(b, d), the GDL antenna had a significantly improved directivity. However, its radiation efficiency was strongly dependent on the thickness of the lower dielectric; it can be tuned in favor of either a maximum directivity or efficiency, the latter having a theoretical limit of $RE_{\mathrm{GDL}} < 95$ %. Both surpass the upper limits of the SPP-based antenna designs. Further, high efficiencies come at the cost of reconfigurability, and a sensible decision between directivity, efficiency, and tunability must be made [101].

Graphene LWAs based on metasurfaces are commonly considered. These metasurfaces generally are developed with unit cells having graphene patch inclusions. Soleimani and Oraizi [88] proposed the use of complementary graphene patch (CGP) cells instead. The properties of square unit cells made up of a regular graphene patch and a CGP were compared by evaluating the corresponding dispersion relations of the TM modes. They were computed using the transverse resonance equation (TRE) and equivalent circuit models [88, 170]. Figure 26(b) depicts the equivalent circuit model of the CGP shown in figure 26(a). The vertical profiles of the individual unit cells in both cases were identical, with graphene being placed on top of a metal-backed dielectric substrate (SiO_2) and a polysilicon biasing pad within it. The unit cells had the side length D. The variable g in the graphene patch unit cell represents the total gap width between the edges of the unit cell and the graphene patch. In the CGP unit cell, g is the width of the square cut-out in the graphene. Their g/D ratios are directly related to their individual surface impedances. Figures 26(c, d) show the dependence of the imaginary part of the surface impedance on the g/D ratio of each unit cell. As the propagation of TM surface modes requires a positive imaginary impedance, the SPPs within the graphene patch unit cell are only supported within a small

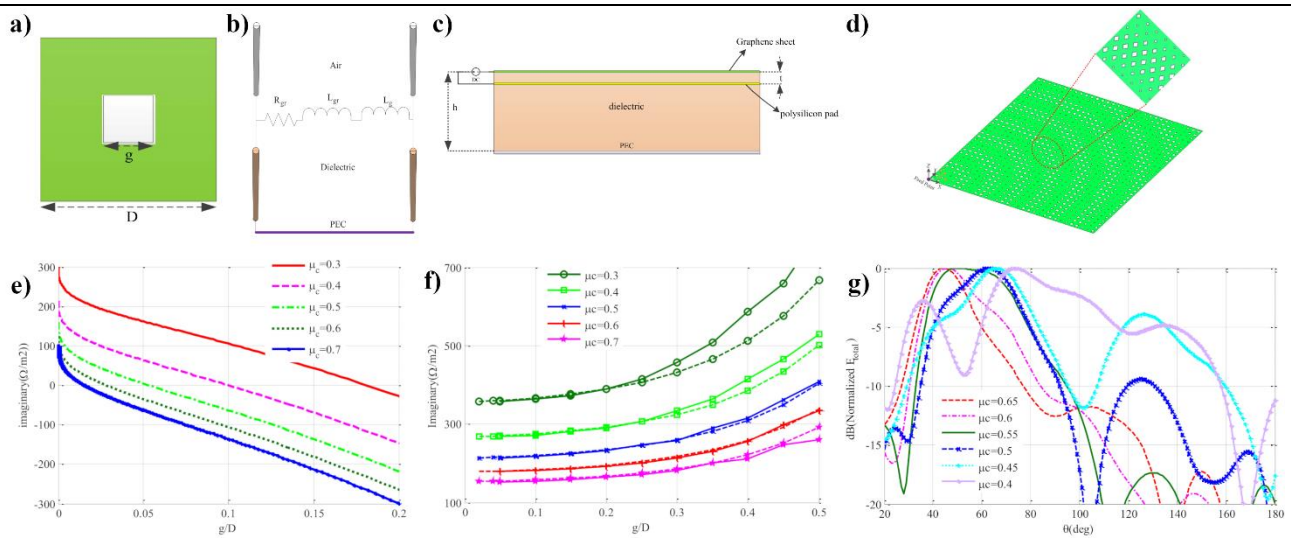

Figure 26. Complementary graphene patch metasurface-based leaky-wave antenna. (a-b) (a) Complementary graphene patch unit cell. (b) Equivalent circuit model. (c) Vertical profile of the unit cell. (d) Metasurface-based leaky-wave antenna with edge feeding. (e) Dependence of the surface reactance of a regular graphene patch-based unit cell on g/D ratio for various chemical potentials between $\mu_c = 0.3 - 0.7$ eV. (f) Dependence of the surface reactance of a complementary graphene patch-based unit cell on the g/D ratio for various chemical potentials between $\mu_c = 0.3 - 0.7$ eV using full-wave numerical simulation (solid line) and the equivalent circuit model (dashed line). (g) Radiation pattern in the $\phi = 45\,°$ direction in the elevation plane depending on the chemical potential between $\mu_c = 0.4 - 0.65$ eV. [88] © IOP Publishing. Reproduced with permission. All rights reserved.

range of g/D that gets even smaller with increasing chemical potential. The CGP unit cell supports TM surface waves regardless of the g/D ratio because the surface impedance is always positive imaginary.

The CGP unit cell was also extended to create a holographic 2D LWA [88]. The antenna was edge fed and designed for an operating frequency of $f_0 = 2$ THz and for the maximum radiation direction $(\theta, \phi) = (45\,°, 45\,°)$. Figure 26(e) shows the final antenna design with individual, differently sized unit cells located periodically away from the feed point. Its simulated patterns indicated the maximum radiation direction was $(\theta, \phi) = (53\,°, 45\,°)$ with a directivity of about 13.5 dBi and a radiation efficiency of 20 %. The high input impedance of the LWA was optimal for matching with a photomixer. Application of a single biasing voltage allowed tuning the chemical potential of the antenna within a range of $0.4 - 0.65$ eV, which enabled beam scanning in the elevation plane within $43\,° < \theta < 73\,°$.

LWAs are highly suitable for CMOS integration [171]. Most non-graphene implementations focus on the microwave frequency range [171-174], with fewer implementations exploring the THz range [171, 174-176]. The main focus has been in the development of highly efficient, high directivity, and wide scan angle implementations for communication applications. As such, much interest has been in the reconfiguration of their polarization [173], beam scanning [172], and multiplexing [175, 176]. RF switches, such as diodes [171] or MEMS [177], are commonly used to achieve reconfigurability.

In summary, the development of graphene-based LWAs has focused on the THz frequency band to take advantage of being able to dynamically tune their properties. Their radiation efficiencies are comparatively low, which has been expected owing to their SPP dispersion losses. Operation outside of the SPP region could increase their efficiencies but would sacrifice their reconfigurability. Alternatively, power recycling approaches could be employed to boost their efficiencies [178]. Reconfiguration is commonly achieved by electrostatic biasing of the graphene. Single voltage biasing architectures have been demonstrated that significantly simplify their manufacturability and design process.

Although graphene has proven to be an excellent material for realizing LWAs, researchers continue to improve on the existing designs and develop new ways of utilizing graphene to its full potential. For example, metal-graphene hybrid LWAs [109] are an excellent example of combining existing implementations with graphene to enhance their operation and achieve tunability. While many non-graphene implementations of LWAs have already been tested and their operation experimentally verified even in the THz frequency range, experimental validation of graphene-based ones is still missing to the best of our knowledge. Table 3 gives an overview of several graphene and non-graphene-based traveling-wave antenna implementations.

Table 3. Comparison of THz traveling-wave antenna implementations

Technology	Design	Operation Frequency [THz]	Steering/ Scanning range	Directivity (Gain)	Radiation Efficiency [%]	Ref.
Metal on GaAs	Yagi-Uda PCA on low temperature grown GaAs	0.636	-	10.8 dBi	80.1	[181]
Graphene on GaAs	Graphene-based Yagi-Uda PCA	1	-	9.57 dBi (8.64 dB)	-	[149]
Au/Ti on glass	Double sided planar quasi Yagi-Uda antenna with complementary dipole excitor	2	-	(4.97 dB)	~95	[182]
Graphene-copper hybrid on SiO_2/Si	Beam steering three armed Yagi-Uda antenna with graphene directors	0.5	± 50 °,± 30 °, 0 °	$(6.8 - 7.79$ dB)	> 91	[85]
Graphene-metal hybrid on polyimide	Beam steering three-layer multi-beam Yagi-Uda antenna with graphene dipoles	$1.136 - 1.220$	360 ° in 60 ° steps	$5.7 - 6.5$ dB	-	[117]
Graphene on SiO_2/poly-Si	Beam scanning LWA through N-periodic modulation of graphene	2	-45.4 ° to 37.5 ° (for $N = 6 - 9$)	-	11	[118]
Graphene on SiO_2/poly-Si	Frequency and beam scanning LWA via width modulated graphene	$1.3 - 1.7$	~ -40 ° to 30 ° for $f_0 = 1.3 - 1.7$ THz ~ -30 ° to 20 ° for $\mu_c = 0.6 - 1$ eV	-	$5 - 20$	[86]
Graphene on SiO_2/poly-Si	Beam steering CGP metasurface 2D LWA with	2	43 ° − 73 ° for $\mu_c = 0.4$– 0.65 eV	13.5 dBi	20	[88]
Metal on indium phosphide/Si	Frequency scanning periodic microstrip line LWA	$0.23 - 0.33$	-46 ° to 42 ° for $f_0 = 0.23 - 0.33$ THz	11 dBi	60	[174]
Dielectric slab RO6010/ RT/duroid 5880 /alumina	Frequency scanning multilayer dielectric slap with periodic metallic discs	$0.1575 - 0.2015$	-23 ° to 38 ° for $f_0 = 0.1575 - 0.2015$ THz	$(10.5 - 15$ dBi)	> 60	[183]

3.1.3 Graphene Antennas on SiC

Graphene antennas have only been experimentally characterized to date using CVD graphene or graphene ink. Similarly, simulations usually only consider quartz, SiO_2, or Si substrates. However, SiC is of particular interest in high-power and high-temperature applications [179] and has recently demonstrated a high level of biocompatibility [180].

Semi-insulating SiC offers a high dielectric constant ($\epsilon_r \cong 9.7$), low conductivity ($\sigma \cong 10^{-5}$ S m^{-1}), and low loss tangent ($\tan(\delta) \cong 10^{-6}$). It has the potential to facilitate achieving high antenna efficiency and miniaturization [179]. The latter is strictly dependent on the relative permittivity and dimensions of a patch antenna which, for example, reduce to $\sim\lambda_0/5$ for a dielectric medium with $\epsilon_r = 10$ [87]. However, this reduction in size comes at the cost of reduced bandwidth [87].

Over 250 polytypes of SiC exist, but their dielectric properties in the upper microwave and THz range are generally not researched due to the lack of available high-quality samples and of actual issues that SiC could resolve [184]. Measurements of the loss tangent of bulk 6H-SiC within the microwave and THz range were conducted. As figure 27 indicates, they demonstrated that the possibility of low dielectric losses exists.

Further research will need to be conducted, particularly on epitaxial SiC on Si, to investigate the possibility that the direct growth of epitaxial graphene on SiC/Si [41] could offer an exciting platform for graphene applications from the microwave to THz regimes. Being bound to the SiC, the material properties would need to be understood and considered in the design of any subsequent graphene-based devices. This would be particularly true in the Reststrahlen band of SiC owing to the near-total reflection of EM waves from it and the surface plasmon-phonon coupling [100, 185].

3.2 Beamforming

Apart from using antenna arrays, beams can be generated and controlled with metamaterials or metasurfaces. For instance, a metasurface can be designed to have an incident EM wave that interacts with its individual unit cells experience an overall phase and amplitude modulation. Ideally, the EM wave would experience minimal amplitude modulation from losses in the unit cells. Moreover, each unit cell should ideally provide a complete 360 ° phase response

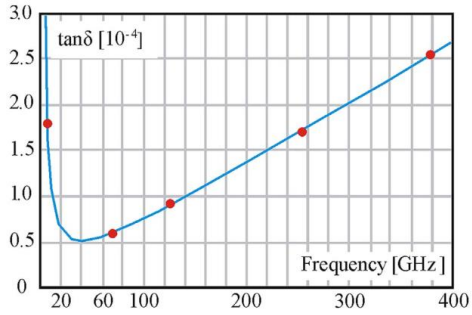

Figure 27. Experimentally measured values of the loss tangent $\tan(\delta)$ of bulk 6H-SiC at five frequency points and their curve fit. Reprinted from [184], Copyright 2017, with permission from Elsevier.

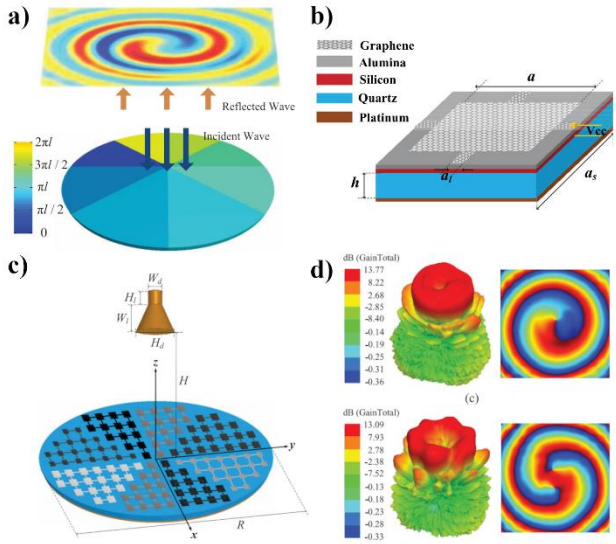

Figure 28. Vortex beam forming reflectarray based on a graphene patch metasurface with dynamic mode control. (a) Schematic representation of a general reflective surface with N-sectors of varying phase increments. (b) Graphene patch-based unit cell consisting of a platinum-backed quartz substrate. Gating circuitry is achieved with silicon and alumina dielectric. (c) Schematic representation of a horn-antenna fed circular reflectarray consisting of eight equal angular sectors. (d) Radiation pattern and phase front of (top) $l = 1$ vortex beam and (bottom) $l = -2$ vortex beam. Mode change was achieved employing electrostatic biasing. © 2016 IEEE. Reprinted, with permission, from [90]

independent of that of the neighboring unit cells [76]. The response further depends on the type of incident wave that excites it, e.g., a plane wave or a point feed. The latter will have different phase contributions at different unit cells in the metasurface due to their position relative to the source point. Various numerical and analytical approaches exist to determine the phase response of individual unit cells and/or the whole metasurface.

Graphene allows for dynamic reconfiguration of the metasurface properties by changing its Fermi level, which results in a change of its conductivity and, thus, the phase and amplitude response to an impinging EM wave. Electrostatic biasing is the most commonly used technique to control the Fermi level. Alternatives, such as optical pumping or chemical doping, are rarely considered. Biasing individual unit cells can result in highly complex biasing circuitry. Their physical dimensions will influence the modulation approach and, therefore, need to be considered in the metasurface design. The two most common graphene-based metasurfaces that are used to manipulate the shape, direction, and polarization of an impinging EM wave are reflectarrays and transmitarrays.

3.2.1 Reflectarray Antennas

Reflectarray antennas are made up of an array of unit cells in which each acts as a reflecting element. They combine the simplicity of reflector-based antennas with the versatility of array-type antennas [186]. Further, one of their main advantages when compared to phased arrays, for example, is that no complex feeding network is necessary. A feed antenna is used to radiate EM waves onto the reflectarray. The surface impedance of the individual antenna elements determines the amplitude and phase change response at each particular element. Reflectarrays are a type of aperture antenna and are most commonly used in the microwave frequency range [170].

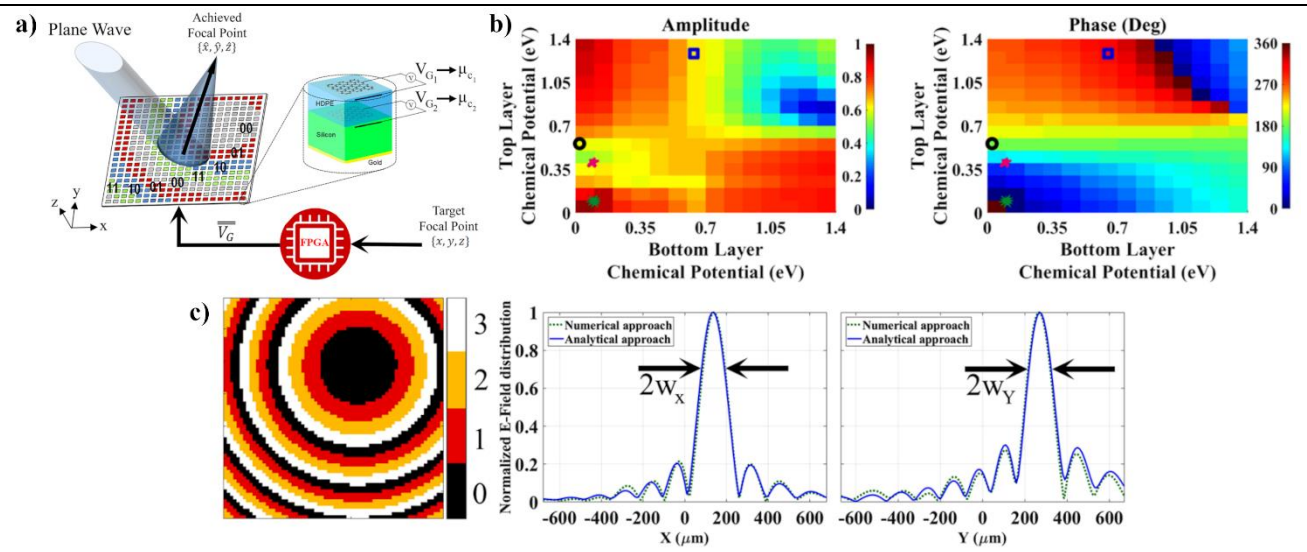

Figure 29. Reprogrammable graphene patch-based metamirror that focuses the beam it reflects when illuminated with an incident plane wave at an arbitrary point in space by means of the dynamic phase modulation at individual unit cells. (a) Schematic representation of a 2-bit FPGA-programmable metasurface with beam focussing and its Fabry-Pérot cavity-like unit cell that consists of a graphene-HPDE-graphene-silicon-gold stack. (b) Electrostatic biasing-induced change of the chemical potential of the individual graphene layer within the unit cell. (left) Amplitude and (right) phase modulation depending on the chemical potentials of top and bottom graphene patches. (c) Off-center beam focusing is achieved by (left) biasing the individual unit cells using the 2-bit coding. Axis field distributions along (middle) X and (right) Y. [106]

Metasurface-based reflectarrays would be particularly well suited in the THz range. Planar metasurfaces are easy to fabricate at micrometer dimensions due to well-defined nanofabrication technologies. Combining metasurfaces with graphene's dynamic tunability allows for dynamic reconfigurability. It can be used for various beam shaping [90, 106, 187, 188], scanning [93, 106, 189-193], polarization [187, 189], cloaking [194], and many more applications within a wide frequency range from microwave [188, 192, 193], over THz [90, 93, 106, 187, 189-191, 194], to the mid-IR [195, 196].

The possibilities of graphene-based reflectarray antennas were first explored by Carrasco et al. [190, 191] and were compared to comparable metal implementations. Their unit cells were based on simple square patches. It is important to stress that the patch dimensions have the most significant influence on the phase modulation. Because of graphene's support of SPPs in the low THz range, resonances can occur in graphene patches whose dimensions match $\sim\lambda_0/24$ [191] or $\sim\lambda_0/10$ [190]. Their frequency depends on the properties of the graphene used, whereas a gold-based unit cell inclusion resonates at $\sim\lambda_0/2$. Consequently, significant miniaturisation of the unit cell structures can be achieved with graphene. Moreover, current advancements in nanofabrication mitigate any fabrication drawbacks in the design of graphene-based metasurfaces. Dynamic tuning of the graphene's conductivity using electrostatic biasing results in changes of its surface impedance and, hence, the phase and amplitude modulation response of the individual unit cells [190]. The modulation response of the unit cells is also analyzed using equivalent circuit models and full-wave simulations. Good agreement between simulations and experiments has been achieved.

Chang et al. [90] designed a graphene-based reflectarray that can be used to create vortex beams. These beams carry orbital angular momentum (OAM) because their EM waves spiral around the axis of propagation. A vortex beam is generated from a horn antenna feed using a reflectarray by splitting its reflective surface into N sectors. Each sector introduces a phase change between 0 to $2\pi l$; a constant phase change increment occurs between neighboring sectors as shown in figure 28(a). The integer l represents the mode of operation and constitutes the number of times the wave spirals about the propagation axis per wavelength (called the twist speed), and its sign indicates the rotation direction. There were $N = 8$ sectors and modes $l = 0, \pm 1, \pm 2$ were used. This choice led to the phase increments of $0\,°, \pm 45\,°, \pm 90\,°$.

The design of a metasurface always begins with its unit cells. The graphene patch-based reflector shown in figure 28(b) was simulated using full-wave simulations. Varying the patch dimensions and the chemical potential of the graphene within $\mu_c = 0 - 1$ eV resulted in a $360\,°$ phase and amplitude modulation. Combinations of the patch dimensions and μ_c were selected to match the required phase increments with minimum attenuation and, hence, maximum radiation efficiency. A schematic representation that depicts the different sized graphene patches in the individual sections is

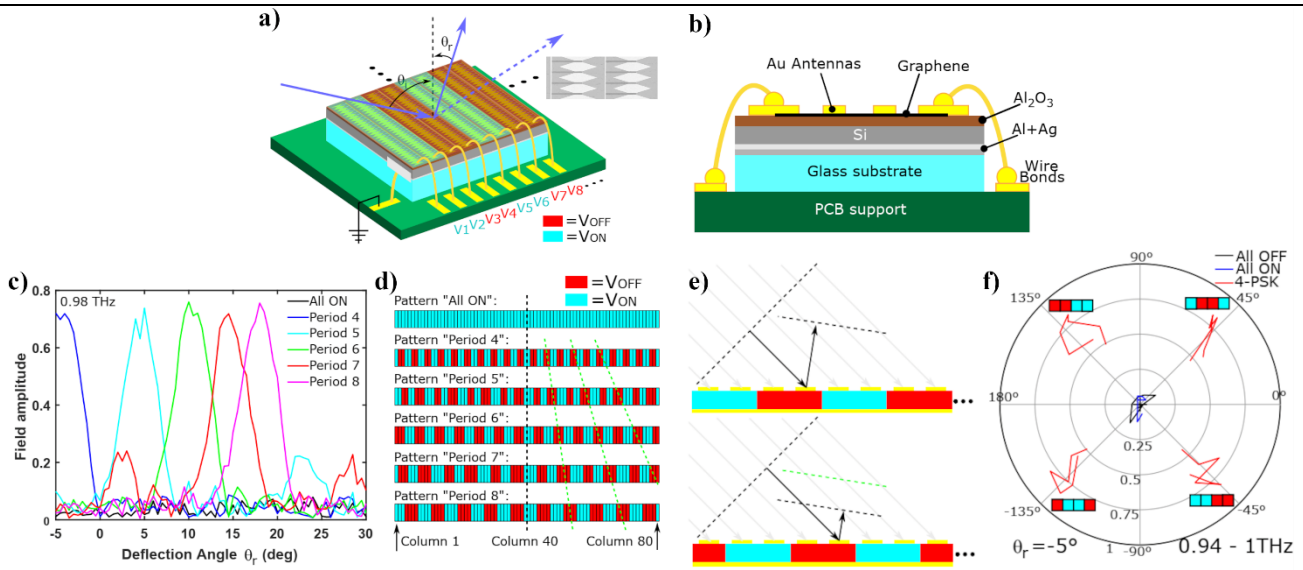

Figure 30. Experimental evaluation of the phase modulation over a graphene-based metasurface reflectarray intended for beam scanning. (a) Schematic diagram of the fabricated reflectarray, which was mounted on a printed circuit board. Inset: Bowtie-based graphene metasurface, including the interconnects for electrostatic biasing of individual columns. (b) The vertical profile of the reflectarray showing the Si in its biasing structure. (c) Measured results for beam scanning at a fixed frequency by varying the period of a column's'On' and 'Off' states. (d) Visualization of the column-based period that was used for the beam scanning results in (c). (e) Example of the phase modulation by moving the period of the 'On' and 'Off' states horizontally, perpendicular to the biasing columns. (f) Measured phase and amplitude of the 4-PSK implementation using the designed reflectarray. Reprinted with permission from [93].

shown in figure 28(c). Electrostatically biasing these individual sections allowed the dynamic selection of the mode, as figure 28(d) illustrates. Since all unit cells within a section were biased equally, the number of different biasing voltages equaled the number of sections. This choice significantly simplified the control network.

Reprogrammable metasurfaces have been designed in which their individual unit cells are independently controlled to achieve the desired response to an impinging EM field. One such design was considered by Hosseininejad et al. in [106]. They developed a metamirror that focused the beam reflected from it to an arbitrary and reconfigurable point when it was illuminated with an incident plane wave. The FPC-like unit cells of the metasurface consisted of two graphene patches with high-density polyethylene (HDPE) between them on top of a gold-backed silicon substrate. Two graphene patches were used to maximize the reflection amplitude and were independently biased to achieve a broad phase response. The system and its chemical potential distribution are shown in figures 29(a, b). Four different chemical potentials were each 2-bit coded to yield four states. They were chosen to achieve a 90 ° phase separation and an amplitude close to 0.7 to attain high focussing efficiency within the operating frequency of 1.9 – 2.1 THz [106]. The unit cells and the whole metamirror were analyzed numerically and analytically. The latter was based on a transmission line model of the unit cell to determine its response. The authors mentioned that Fresnel diffraction theory could not be applied because of the small focal-length to lens diameter ratio. Instead, Huygens' principle was invoked to model small pieces of the excited surface currents as radiation sources [106, 130]. Figure 29(c) shows how an off-center beam was focused using the proposed reflectarray. The reflected beam was elliptical because the reflectarray could not achieve an off-center circular beam with its finite size.

Much of the research on utilizing graphene in the THz frequency range has been focused on numerical and analytical studies of their designs. One of the first experimentally demonstrated CVD graphene-based metasurface reflectarray was reported by Tamagnone et al. in [93]. It is shown in figures 30(a, b) and was designed to manipulate the phase of an s-polarized beam that was incident on the metasurface with an incident angle of 45 °. The beam's reflection angle was steered, as shown in figure 30(c). The unit cell consisted of a gold bowtie antenna chosen for its wideband response and a SLG patch in its center placed on top of a Salisbury screen configuration [93, 197]. The operation of the reflectarray was based on two operating states that require a 180 ° phase change between each other while maintaining a similar amplitude modulation. They are termed 'On' and 'Off'; the 'Off' state was set to result in total absorption. Biasing was applied on a column-to-column basis. Their specific biasing voltages were chosen by considering the surface impedance-dependent reflection coefficient of the unit cell.

The reflectarray was fabricated using nanofabrication procedures and mounted on a printed circuit board (PCB). It was characterized using a THz time-domain spectroscopy (TDS) system. Figures 30(c, d) show how periodically biasing the individual columns resulted in controlled tunability of the reflection angle within $-5\,°$ to $20\,°$. The period profiles were calculated by interpreting the unit cells as discrete radiators and determining the interference pattern of their radiated fields [93]. The reflectarray was further used to demonstrate phase-shift keying (PSK). Figures 30(e, f) show how a constant phase change was introduced to the reflected beam while maintaining the reflection angle by moving the period of the biasing states along the reflectarray. The radiation efficiency of the reflectarray was determined to be ~ -12 dB $\cong 6.3$ %, while the maximum of an ideal system is limited to $-8\,dB \cong 15.8$ %. Further improving the mobility of graphene and the biasing network to achieve larger tunability is expected to increase the overall efficiency.

Most beamforming devices based on graphene are studied at THz frequencies and above as graphene acts as a variable resistor in the microwave range, and the lacking reactance complicates phase control [192]. Nevertheless, dynamically controllable examples have been demonstrated in [188, 192, 193]. Due to the limited phase control, the graphene-based unit cells are designed to operate in two states that exhibit a $180\,°$ phase change between them, as demonstrated by Tamagnone et al. While the results seem promising, graphene still suffers from high ohmic losses at microwave frequencies, i.e., the reflection amplitude of reflected EM waves of metasurface designed by Chen et al. [192] is 0.33 while the structure absorbs the rest.

Non-graphene reflectarray implementations currently focus on employing metallic or dielectric resonators [76]. The former are generally supported on low-loss dielectric materials to reduce losses. Passive implementations as a lens using aluminum resonators on polypropylene (PP) have achieved efficiencies of 80 % at 350 GHz [198] and efficiencies of $30-60\%$ at 0.7, 1.0, and 1.5 THz using silicon as the dielectric [199]. Reconfiguration has also been achieved using varactor-diodes [200], MEMS [201], liquid crystals [202], and more. However, THz implementations are rare due to the issues discussed in Section 3. Dielectric resonators have much lower ohmic dissipation and do not require separation from the ground plane. However, integration with tunable elements is not trivial [76]. Non-reconfigurable examples have achieved efficiencies of up to 90 % at $\sim$480 GHz using Si/SiO_2 resonators in an all dielectric metasurface mirror [203].

A current hot topic in the research of reflectarrays is reconfigurable intelligent surfaces (RIS) [204, 205]. Here, the phase responses of the reflectarray elements are discretized and binary coded. However, discretization can significantly impact the quality of the reflected beam. For example, a two-level phase quantization results in diffraction efficiencies below 50 % [76]. Microprogrammed control units (MCUs) or field-programmable gate arrays (FPGAs) can be used to control the metasurface and, thus, the response of the reflectarray to an impinging EM wave. The primary RIS applications have been focused on the microwave frequency range for 5G communication systems.

In summary, the concept of graphene-based metasurface reflectarrays shows great potential for dynamic beam steering and beam shaping applications in the THz frequency range. First examples of RISs have been demonstrated at microwave frequencies. However, the biasing of graphene still poses a technological challenge. Further improvements in efficiency and biasing concepts are required for practical THz reflectarray implementations.

3.2.2 Transmitarray Antennas

In contrast to reflectarrays, where an incident EM wave is modulated and then re-radiated by the metasurface, the incident EM wave incident on a transmitarray couples with its metasurface as it passes through it. Their major advantage in comparison to reflectarrays is avoidance of the feed antenna and its supporting structures blocking the fields reflected from its metasurface [186]. However, transmitarrays are more prone to losses because the incident EM wave must propagate through a lossy metasurface. Furthermore, multi-layer structures and polarization converters might be necessary to achieve the desired phase response [76], which would further increase the losses.

Researchers have applied graphene-based transmitarrays in dynamic beamforming applications by modulating the amplitude [206-208], phase [18, 107, 207], and polarization [18, 209] of the incident EM fields. Tavakol and Khavasi [107] designed a meta-coupler based on hybrid metal-graphene metasurfaces. This meta-coupler is shown in figure 31(a). It captures the incident propagating wave via a metasurface-based metamaterial and couples it into surface wave modes in an underlying waveguide. The main challenge it solved was the efficient coupling of an incident propagating wave into unidirectional surface waves. The meta-coupler accomplished this by overcoming the momentum mismatch between various modes. The meta-coupler operated in two states set by electrostatic biasing of the graphene and produced the phase modulation of the wave that was coupled to it. Depending on its state, the power of the incident field is transferred to either port of the underlying waveguide. The coupling between the incident field and the surface waves can be analyzed using the generalized form of Snells' law of refraction [89]. It requires the refraction angle θ_t to be complex to compensate for the momentum mismatch [107].

The unit cell of the transmitarray consisted of a complementary H-silver film, with a graphene patch in its cutout, placed on a SiO_2 substrate. Four layers were stacked

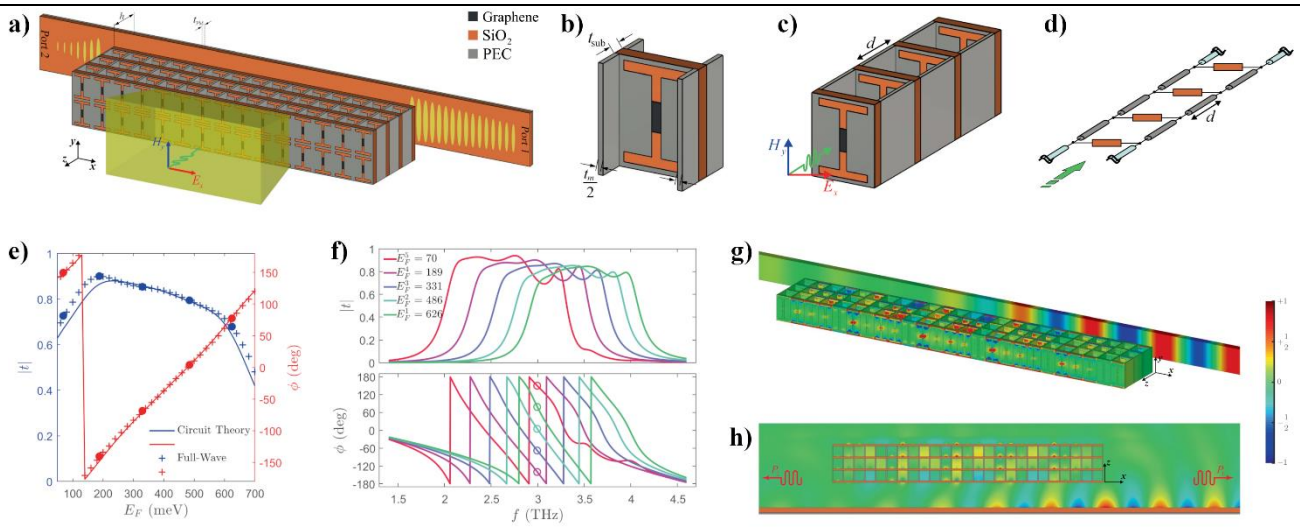

Figure 31. Meta-coupler based on hybrid metal-graphene metasurfaces. (a) Model of the graphene-based meta-coupler operating in its state 1. Incident EM fields couple into the metamaterial. Graphene's tunability is used to modulate the phase of the incident EM wave and guide it towards the appropriate port. (b) H-complementary metal and graphene patch metasurface unit cell with silver sidewall for decoupling. (c) Metamaterial supercell stack. (d) Equivalent circuit model of supercell. (e) Comparison of the amplitude (left) and phase (right) of the supercell derived from full-wave simulations and the equivalent circuit model depicted in (d). (f) Frequency dependant amplitude (top) and phase (bottom) of the supercell extracted from full-wave simulations under different biasing conditions between 70 to 626 meV. (g) 3D visualization of the y-component of the normalized magnetic field distribution for an impinging x-polarized Gaussian beam with the coupler meta-coupler operating in its state 1. (h) 2D visualization of the y-component of the normalized magnetic field distribution in the xz-plane when the coupler is operating in state 1 and a x-polarized Gaussian beam is incident upon it. [107]

and connected using silver walls to reduce the coupling between the individual cells, as illustrated in figures 31(b, c). In addition, a biasing structure was considered in the design by placing polysilicon thin polysilicon rods inside the dielectric.

The graphene-metal interactions dominated the response of the unit cell. The shunt admittance of the unit cell was extracted from full-wave simulations and used in the equivalent circuit model. The average transmission was 89 % for a chemical potential of $50 - 700$ meV. A phase shift of $\sim 70\,°$ was achieved. The separation distance between the layers in the stack was optimized to achieve a phase shift of $360\,°$. Figures 31(e, f) show the five chemical potentials chosen to achieve equally spaced phaseshifts of $360\,°/5 = 72\,°$ between them and their influence on the attenuation and phase shift of the unit cell stack. Supercells consisting of five unit cell stacks were formed, and their length needed to be equal to the wavelength of the surface wave at $f_0 = 3$ THz to meet the phase-matching condition [107]. Finally, the distance between the waveguide and the transmitarray was optimized to achieve a maximum coupling efficiency C (ratio of the surface wave's power at the target port to that delivered by the incident wave to the system) or the directivity D (ratio of the surface wave power at the target port and at the other port). Maximum values of $C = 46\,\%$ and $D = 19$ dB were achieved, although at different separation distances. It was pointed out that higher efficiencies have been achieved in the microwave and optical frequency range, yet they are not reconfigurable.

A polarization transforming graphene-based metasurface was designed by Masyukov et al. [18]. An MLG-dielectric-metal hybrid structure was employed to induce a chiroptical response, and optical pumping was used for dynamic tuning. MLG was used instead of SLG because it provides stronger interaction with the optical pumping. The individual unit cells were formed with dimensionally identical MLG and gold chiral petal ring resonators deposited on the top and bottom, respectively, of a polymethylpentene (TPX, $\epsilon_r = 2.1$) substrate, as shown in figure 32(a). The complex Jones matrix of an individual unit cell was extracted from numerical simulations and was specified in a linear-orthogonal basis. Because the resonator was rotationally symmetric, the matrix was recast in a circular basis [210] and simplified. The optical pumping changed the graphene's properties [19] and resulted in a variation of the co- and cross-polarization coefficients of that Jones matrix within the specified frequency region: 0.5 to 0.9 THz, as illustrated in figures 32(b, c).

The transmission coefficients for the RHCP and LHCP fields were represented by the co-polarization and cross-polarization coefficients. Alternatively, temporal coupled-mode theory (TCMT) [211] was employed to analytically

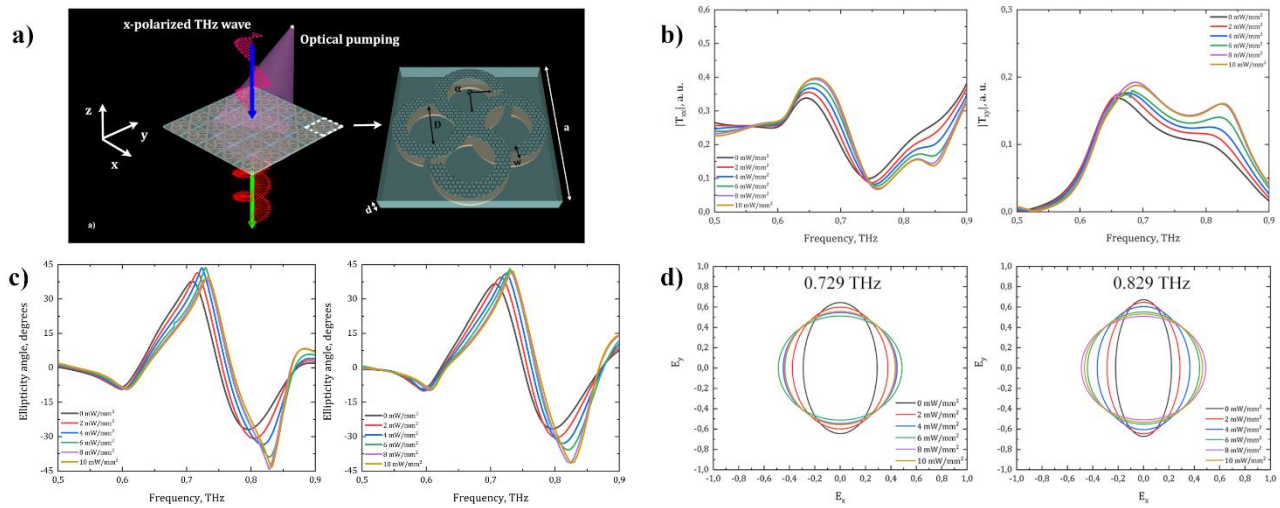

Figure 32. Graphene-based metasurface transmitarray that produced a chiroptical response to a linearly polarized incident electromagnetic field. The response of the transmitarray is tuneable using optical pumping. (a) Schematic representation of the transmitarray being optically pumped by a tuneable light source (left). The metasurface's unit cell is composed of dimensionally identical multi-layer graphene and gold chiral petal ring resonators that are deposited on the top and bottom of a polymethylpentene substrate, respectively (right). (b) Co-polarization coefficient under various optical pumping powers as extracted from numerical calculations. (c) Cross-polarization coefficient under various optical pumping powers extracted from numerical calculations. (d, e) Frequency spectra of an ellipticity angle chiral transmitarray for various optical pumping powers obtained with (d) numerical simulation and (e) temporal coupled-mode theory. (f, g) The optical pumping power-dependent polarisation ellipses at (f) 0.729 THz and (g) 0.829 THz. [18] © 2020, CC BY 4.0. To view a copy of this license, visit http://creativecommons.org/licenses/by/4.0/

determine the transmission coefficients. The outcomes of both approaches showed good agreement and facilitated the calculation of the ellipticity angle. Variation of the ellipticity angle by 20 ° was achieved as presented in figures 32(d-g).

Transmitarrays are less often considered at THz frequencies in comparison to reflectarrays. Generally, a tradeoff between the efficiency and phase control of transmitarrays and reflectarrays needs to be made. For example, a two-layer copper and benzocyclobutene (BCB) based transmitarray reported in [212] achieved a maximum transmission of 95 % and a y-polarization beam deflection of 2.4 ° for a single layer at 1.2 THz, and a maximum transmission of 70 % at 1.15 THz and y-polarization beam deflection of 6.1 °. A flexible gold and polyimide-based three-layer transmitarray achieves a maximum transmission of 44 % at 0.9 THz and a beam deflection of 35 ° [213]. However, neither systems are reconfigurable.

Reconfigurable non-graphene implementations use the same tunable elements as metasurfaces introduced in Section 3. For example, pin diode-based microwave transmitarray was developed in [214]. On the other hand, graphene's tunability can be used to reconfigure the characteristics of graphene-based transmitarrays dynamically. Their biasing architecture needs to be carefully designed as the impeding EM waves will couple to them.

3.3 Absorbers

The absorption of EM fields has a wide range of applications has a wide range of applications. They include EM interference shielding[215], cloaking [216], sensing, spectroscopy, and more.

Most absorbers can be categorized into resonant and broadband absorbers [217]. Resonant absorbers operate at a specific frequency f_0 and generally consist of multiple layers separated by $\lambda_0/4$. Notable examples of resonant absorbers are the Salisbury screen, Jaumann absorber, Dällenbach layer, crossed grating absorber, and circuit analog absorber [217]. For example, a Salisbury screen structure consists of a thin resistive sheet deposited on a ground-backed $\lambda_0/4$ thick dielectric that forms a Fabry-Perot resonator. Its main disadvantage is their sensitivity to angle of incidence of the fields [197].

If a simple vacuum embedded dielectric layer with permittivity $\epsilon = \epsilon_0\epsilon_\mathrm{r}$ and permeability $\mu = \mu_0\mu_\mathrm{r}$ is considered, where ϵ_0 and μ_0 are the vacuum permittivity and permeability and where ϵ_r and μ_r are the relative permittivity and permeability of the dielectric, the reflection coefficient r and transmission coefficient t for a normally incident plane wave can be derived by the Transfer-Matrix method [218] and are given by [217]

$$r = -\frac{\mathrm{i}}{2}\left(\frac{Z}{Z_0} - \frac{Z_0}{Z}\right)\sin(nkd)\,t \tag{31}$$

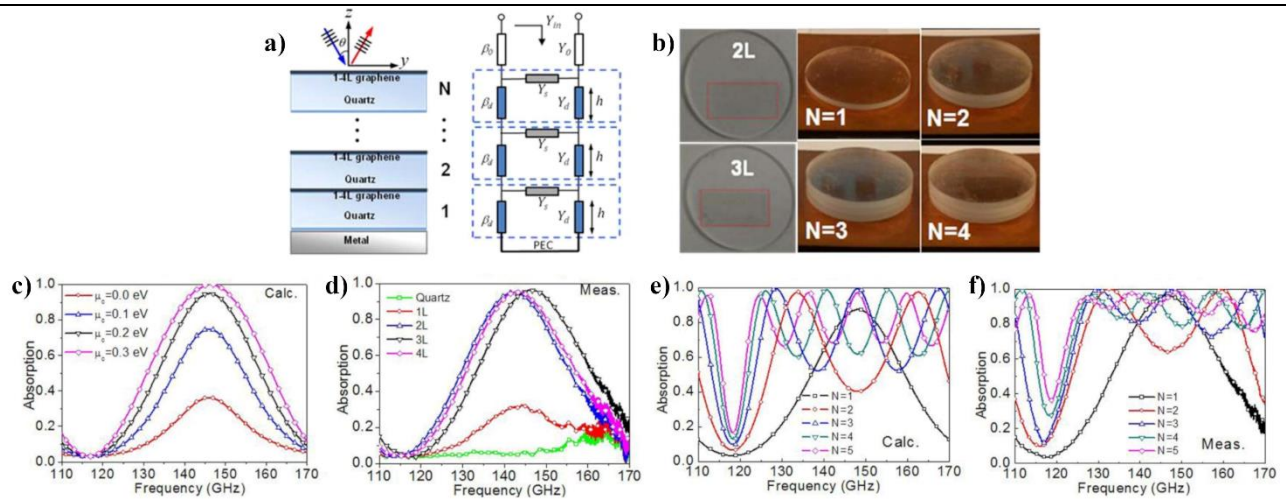

Figure 33. Salisbury screen and Jaumann stack absorbers. (a) Schematic and transmission-line model of a graphene Jaumann absorber. (b) chemical vapor deposited graphene on quartz-based Salisbury screen ($N = 1$) and Jaumann stack ($N = 2, 3,$ and 4) absorbers with varying layer count N. (c) Analytical evaluation of the dependence of the chemical potential on the absorption characteristics of a Salisbury screen absorber. (d) Measured absorption characteristics of a Salisbury screen absorber for varying numbers of graphene layers. (e) Analytical evaluation of the dependence of the absorption characteristics of a Jaumann absorber on the layer count N. (f) Measured absorption characteristics of graphene-based Jaumann absorbers with different numbers of layers N. [108] © 2014, CC BY 3.0. To view a copy of this license, visit http://creativecommons.org/licenses/by/3.0/

$$t = \left[\cos(nkd) - \frac{\mathrm{i}}{2}\left(\frac{Z}{Z_0} + \frac{Z_0}{Z}\right)\sin(nkd)\right]^{-1} \qquad (32)$$

where $Z = \sqrt{\mu/\epsilon}$ and $Z_0 = \sqrt{\mu_0/\epsilon_0}$ are, respectively, the impedances of the dielectric and the free-space, $n = \sqrt{\epsilon_\mathrm{r}\mu_\mathrm{r}}$ is the refractive angle of the dielectric, k is the wavevector in the dielectric, and d is the thickness of the layer. The reflectivity R and the transmissivity T are related to r and t via $R = |r|^2$ and $T = |t|^2$. The absorptivity, which is the relation of the absorbed and incident spectral powers ($A = Q_\mathrm{abs}/Q_\mathrm{inc}$) [219], is determined using [218]

$$A = 1 - T - R. \qquad (33)$$

It becomes obvious that it is necessary to impedance match the free-space and the dielectric in order to reduce the reflectivity and increase the absorption. It should be noted that A, R, and T are often strongly frequency-dependent, not only due to the dimension dependence of the structures but also due to frequency-dependent values of the permittivities and permeabilities of the materials used.

A Jaumann absorber is based on the same concept as the Salisbury screen, but several layers of resistive sheets and dielectrics above a ground plane are stacked [108, 197]. An example model is shown in figure 33(a). Stacking many layers results in multiple resonances and thus broadband response of the absorber [217]. Broadband absorbers operate frequency independent. Other common examples are the geometric transition absorber, well known from anechoic chambers, and the low-density absorber [217].

One of the most common applications of broadband graphene-based absorbers is solar absorbers. Solar radiation ranges from $295 - 2500$ nm, which equates to $\sim 100 - 1200$ THz and comprises IR, visible, and UV light [220]. Graphene-based devices designed to operate in that frequency range can be used as sensors and optoelectronic devices, or for energy harvesting and photovoltaic applications [219]. In particular, graphene in perovskite solar cells has found various applications, i.e., as electrode-material, carrier transporting material layer within the electron selective contact layer, and as a stabilizing material against ageing effects [221]. The use of GO has also shown promising applications due to the capability of tailoring material properties via the tuning of oxygen-containing functional groups [222, 223]. Recent developments of graphene solar absorbers focus on the design of metasurfaces and metamaterial devices where the topologies are chosen for obtaining broadband absorption, ideally close to unity, throughout the solar radiation frequency range [219, 220, 224].

Similar to the design of metasurface-based reflectarrays and transmitarrays, the operating parameters of metasurface-based absorbers strongly depend on the structures and their dimensions. Integrating graphene elements into THz absorber applications is of particular interest due to its tunability [91], compatibility with nanofabrication, broadband absorption characteristics [225], and demonstrated absorption enhancements [226]. Their tunability, in particular, offers the possibility of reconfiguring the absorption characteristics of a device. Many examples of graphene-based absorbers have been demonstrated in the microwave [108, 216, 227-230],

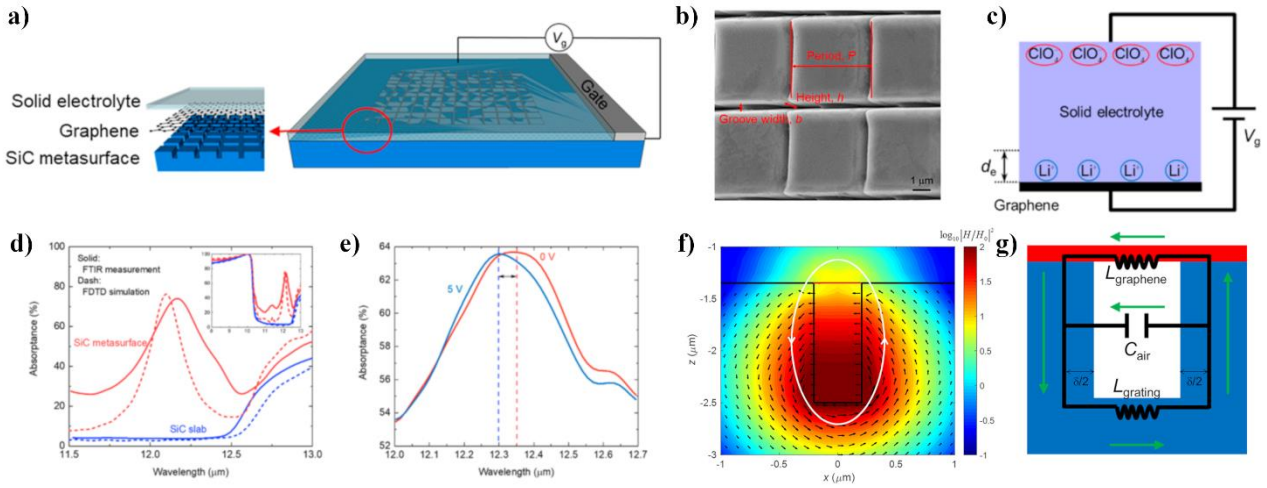

Figure 34. A THz absorber based on a graphene sheet covering a SiC metasurface. The graphene sheet is electrostatically biased using a voltage-biased solid polymer electrolyte. (a) Vertical profile and schematic representation of the designed absorber. Biasing voltage is applied between the graphene sheet and a probe stuck into the electrolyte. (b) SEM image of the SiC-based metasurface. (c) Application of a voltage to the electrolyte results in the formation of a capacitor due to the movement of free ions(Li^+ and ClO_4^-) (d) Comparison of the measured and simulated (using the finite-difference time-domain method) absorbance spectra of bare SiC (red) and SiC-based metasurface (blue). (e) Measured biasing voltage-dependent absorbance spectrum of the graphene-based absorber. (f) Numerical simulation of magnetic field distribution within the metasurface unit cell. (g) Equivalent circuit model used for the evaluation of the magnetic polariton resonance frequency. Reprinted with permission from [103]. Copyright 2019 American Chemical Society.

THz frequency ranges [91, 103, 105, 225, 231-234], and well into the infrared (IR) frequency range [226, 235]. Researchers generally aim to achieve total absorption within specified design constraints. Notable examples are given in [91, 231].

Wu et al. [108] designed a graphene-based absorber in the microwave frequency range using both Salisbury screens and Jaumann stacks. Figure 33(b) shows the fabricated absorbers. Each layer consists of numerous CVD SLGs transferred onto a quartz substrate. The Salisbury screen absorbers were considered to analyze the influence of the graphene layer count and doping on the absorption. The results of these parameter studies are shown in figures 33(c, d). As no biasing was considered in the design, the dependence of varying the chemical potential of graphene was determined using an equivalent circuit model and transmission line theory. Varying μ_c from 0 eV to 0.3 eV results in a significant increase in the absorption because the impedance of graphene becomes matched to the free-space impedance at $\mu_c = 0.3$ eV. A fabricated single-layer Salisbury screen absorber was measured using reflectometer measurements; the absorption dependence on the graphene-layer count was evaluated from 110 to 170 GHz. While SLG on quartz only showed a peak absorbance of $\sim$30 %, stacking only two layers of SLG resulted in an absorption of $\sim$95 %.

The performance of Jaumann absorbers with up to five layers ($N = 5$) was analyzed using the same approaches. Both the analytical and measurement results showed increased bandwidth with an increasing layer count. The 5-layer Jaumann stack achieved an absorption of $\sim$90 % from 125 GHz to 165 GHz with a fractional bandwidth of 28 %, as shown in figures 33(e, f). In particular, the bandwidth was strongly dependent on the thickness of the dielectric and its permittivity. It could be significantly improved if materials with lower permittivity are used. Measurement of the absorption characteristics at different angles of incidence showed that the absorber is suitable for TM-polarized waves with any incidence angle. In contrast, the absorption diminishes for TE-polarized waves with an angle of incidence larger than 30 °.

Tunable graphene-based absorbers in the microwave range generally consist of self-gated graphene-electrolyte-graphene capacitors [216, 227-230]. Similar to the example above, Balci et al. [216] designed a Salisbury screen absorber that operated at 10.5 GHz. Apllying a bias of $0 - 1.5$ V allowed for dynamic tuning of the reflection from -3 dB to -45 dB. The graphene-based capasitor itself absorbed $21 - 45$ % of the EM waves, for $V_{\text{bias}} = 0 - 3.5$ V. Zhang et al. [228] explored the possibility of exclusively using graphene-electrolyte-graphene capacitors as absorbers. A single capacitor within a rectangular waveguide absorbed between $50 - 99.79$ % of the EM waves within the spectrum of the waveguide ($3.4 - 4.9$ GHz) with a biasing voltage of $0 - 3$ V.

While the absorption of microwave fields is a common research topic, research on graphene-based absorbers has again been focused mostly on the THz and IR frequency spectrums. In particular, the THz spectrum has received

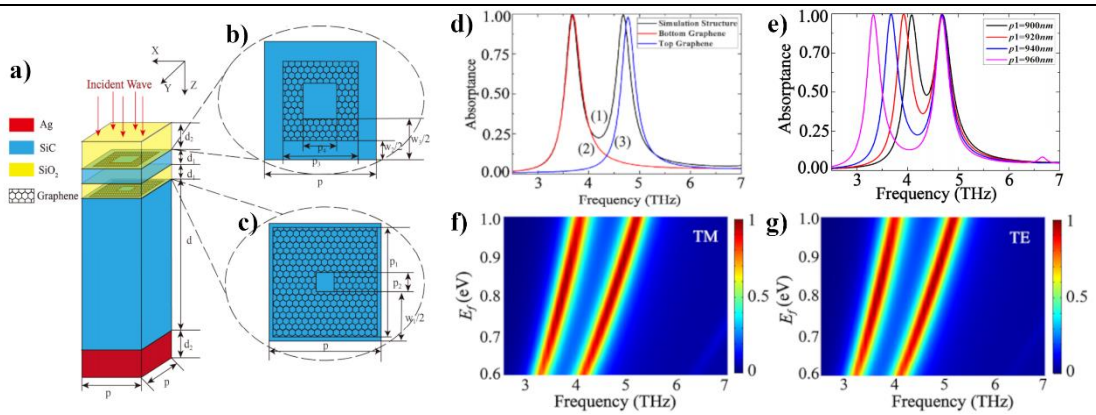

Figure 35. Tunable graphene-based multiband absorber for polarization angle independent electromagnetic wave absorption in the THz range. (a-c) Vertical profile of the absorber, consisting of two stacked SiO_2/graphene/SiC resonators, and the structure of the graphene square rings. (d) The absorption spectra of the individual resonators and the absorber stack. (e) Resonance frequency dependence on a single graphene square ring dimension. (f, g) Dependence of the absorption spectrum on the Fermi level when the absorber is excited by transverse magnetic (f) and transverse electric (g) incident waves. Reprinted by permission from [91]. © 2019 Optical Society of America.

considerable attention because of the plasmonic effects in graphene. For instance, Long et al. [103] designed and fabricated an absorber based on a graphene sheet covering a SiC-based metasurface. Figures 34(a-c) show the schematic representation of the absorber and an SEM image of its SiC-based metasurface. The metasurface was fabricated using FIB. The CVD SLG was then transferred onto the structured metasurface. The graphene was electrostatically biased. However, instead of using a typical capacitive gate, a solid polymer electrolyte made of lithium perchlorate ($LiClO_4$) and polyethylene oxide (PEO) was deposited on top of the graphene's surface [236]. Application of a voltage via a probe stuck into the electrolyte led to the formation of a capacitor resulting from the movement of free ions (Li^+ and ClO_4^-). The so-formed ionic layer at the graphene-electrolyte interface was about 1 to 5 nm thick. The increased capacitance it provided yielded a wider tuning range than capacitive biasing via a dielectric [103].

Figures 34(d, e) illustrate the absorbance spectra measured with FT-IR spectroscopy of the bare SiC, the SiC metasurface, and the graphene-based absorber. The SiC case was numerically simulated using the finite-difference time-domain (FDTD) method [87] and was compared to measurement results with reasonable agreement. Variations arose from the doping of the SiC during the FIB process. The last case showed a shift in the absorbance resonance with the application of a biasing voltage.

The unit cell of the metasurface was numerically simulated, and the magnetic field distribution was extracted to analyze the physical phenomenons within the metasurface. The results are shown in figure 34(f). The strong magnetic confinement within the grove and the counter-clockwise electrical current around the grove suggest that magnetic polaritons (MP) were excited [103, 237]. The excitation of MPs had been demonstrated previously by Wang and Zhang [237]. Long et al. [72] showed that graphene can be used to tune its resonance. The equivalent circuit model in figure 34(g) was used to determine the MP resonance's dependence on graphene's chemical potential.

Often EM fields with a specific frequency or wavelength can be targeted and absorbed. On the other hand, Wu et al. [108] experimentally demonstrated high absorption with wide bandwidth in the microwave range, with total absorption being the desired property. Another possibility was reported by Bao et al. in [91]. A graphene-based multiband absorber was developed. Figures 34(a-c)) show the vertical profile of that absorber. It consisted of two SiO_2/graphene/SiC resonator stacks layered on top of each other. Figure 35(e) illustrates how the graphene was structured as square rings, and the absorption spectra were closely linked to their dimensions. The two stacks have dedicated absorption characteristics, and by layering them, their absorption responses are superimposed. This feature is visualized in figure 35(d), where the full-wave simulation of the individual resonators and the stacked resonators are compared. The top graphene layer strongly couples to one frequency, while the bottom layer coupled to the second frequency. The coupling effects are further analyzed using coupled-mode theory (CMT) [238] and show good agreement with the numerically simulated results [91].

Changing the Fermi level of graphene significantly shifts the absorption spectrum. Figures 35(f, g) show how both absorption peaks experience a blue shift with increasing E_f. Furthermore, the absorption is enhanced. Total absorption was achieved for $E_F = 0.8$ eV. However, no biasing architecture was considered in the design.

The absorber is polarization angle independent for both TM and TE incident waves and can further be extended to cover

Table 4. Comparison of absorber implementations

Technology	Design	Frequency	Absorption [%]	Ref.
Graphene/ electrolyte/ graphene capacitor on top of varactor-based metasurface	Independently tunable graphene/ electrolyte/ graphene-capacitor and varactors metasurface absorber stack	$3.1-6.1$ GHz	-	[230]
Graphene/ electrolyte/ graphene capacitor	Tunable N-layer ($N=1-3$) graphene electrolyte capacitor-based Salisbury screen and Jaumann stack absorbers	$3.4-4.9$ GHz	$50-99.79$ ($N=1$, $V_{\text{bias}}=0-3\,V$)	[228]
Graphene/ electrolyte/ graphene capacitor	Tunable graphene electrolyte capacitor-based Salisbury screen absorber	10.5 GHz	$21-45$ ($V_{\text{bias}}=0-3.5\,V$)	[216]
CVD MLG on quartz	Salisbury screen and Jaumann stack absorbers of $N=1-5$ layers.	$125-165$ GHz	$\sim$95 ($N=2$) $\sim$90 ($N=5$)	[108]
SiO_2/Graphene/SiC	Tunable multiband absorber made of multiple layer stack ($N=2-4$) of SiO_2/ graphene-square-rings/ SiC resonators over a metal layer	3.67, 4.73, 5.9, 6.94 THz ($N=4$)	98.6 ($N=4$) 100 ($N=2$, $\mu_c=$ 0.8 eV)	[91]
Electrolyte biased CVD SLG on SiC metasurface	Tunable graphene-based metasurface absorber consisting of electrolyte/ graphene/ SiC metasurface stack	24.6 THz ($V_{\text{bias}}=0\,V$) 25.6 THz ($V_{\text{bias}}=5\,V$)	$\sim$80	[103]
Copper on Fr-4 substrate	Wide-angle TE and TM absorber based on N-blade ($N=4-12$) unit-cell metamaterial	$\sim$5 GHz	$\sim$99	[239]
Polyimide/ copper/ liquid crystal/ polyimide	Tunable wideband absorber based on liquid crystal	130 GHz (unbiased) 119 GHz (biased)	>90	[240]
VO_2/Al_2O_3	Tunable absorber based on VO_2 and optical laser pumping	$0.2-1$ THz	18.9 (no pumping) 74.7(6 mJ cm^{-2})	[241]

more frequencies by stacking additional resonators. Using this approach, an absorber was also designed in [60], in which four resonators were stacked on top of each other. Three of the resonant responses reached perfect (100 %) absorption, and one reached 98.6 %.

While the absorption region of graphene-based absorbers is closely linked to their dimensions, and they provide limited or no frequency tunability, researchers suggest combining graphene-based absorber structures with metallic metasurfaces and tunable elements [229, 230]. Zhang et al. [230] designed a graphene-electrolyte-graphene capacitor-based absorber and coupled it with a varactor-based metallic metasurface. The Absorber operates in the microwave range. The absorption frequency can be tuned from $3.1-6.1$ GHz by applying a voltage to the varactor diodes, which modifies their capacitance. On the other hand, graphene's tunability is used to modulate the absorption itself, and the reflection amplitude can be tuned from -3 dB to -30 dB.

Table 4 gives a brief comparison of several graphene and non-graphene implementations of microwave and THz absorbers.

3.4 Photodetectors

Apart from the emission and manipulation of EM fields using graphene-based devices, their detection has become a significant research area [242] owing to graphene's properties, specifically its small heat capacity [242, 243], weak electron-phonon coupling [242, 244], and large Seebeck coefficient [244]. Detectors generally find application in fields such as security, biomedical imaging, and spectroscopy [111]. Graphene, in particular, combines several photocurrent generation mechanisms useful for detecting EM waves, as illustrated in figure 36. They include the photovoltaic effect, the photo-thermoelectric effect (Seebeck effect), the bolometric effect, the photo-gating effect, and the plasma-wave assisted mechanism [245], which is often referred to as the Dyakonov-Shur mechanism after its first implementation [246].

Early adaptations of graphene-based detectors were mainly focused on the visible spectrum using metal-graphene-metal structures and were based on the photovoltaic effect [247, 248]. Designing the detector as a back-gated GFET facilitated the investigation of electrostatic biasing on graphene and exposed its influence on the detector's photoresponsitivity and photoresponse [248]. The investigation of graphene doping due to the interaction with metal contacts and edge effects showed the formation of p-type and n-type doped regions in the graphene [247]. Creating p-n junctions in graphene using

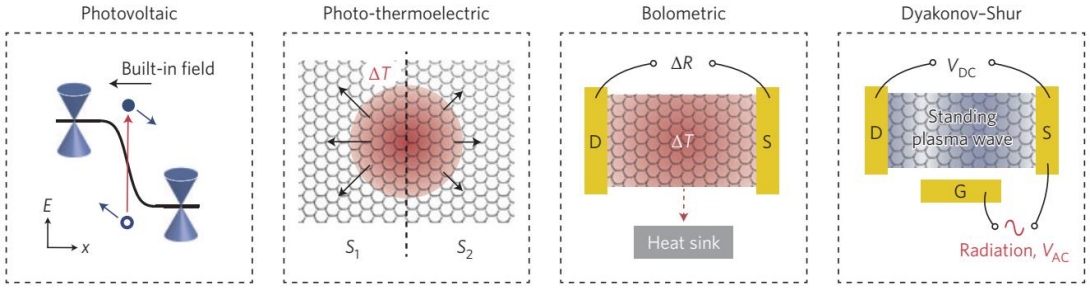

Figure 36. Main photocurrent generation mechanisms used in graphene-based detectors. Reprinted by permission from [245]. Copyright 2014 Springer Nature.

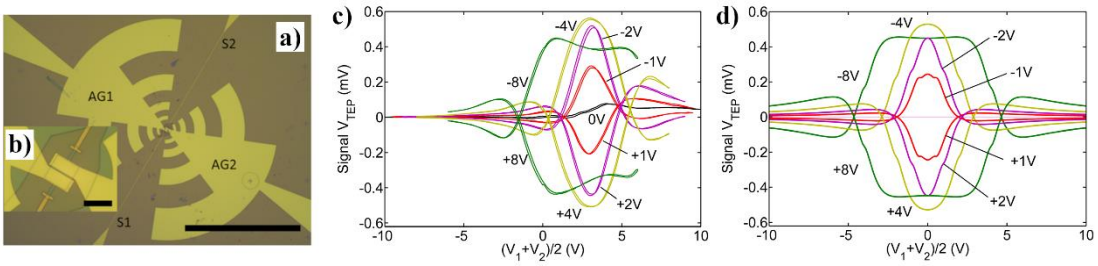

Figure 37. Log-periodic antenna-coupled graphene-based bolometer. (a) Image of the fabricated detector with read-out ports S1 & S2 and the antenna gates AG1 & AG2. (b) Close up of graphene flake, antenna gates, and read-out contacts. (c, d) The Photo-generated voltage at read-out ports S1 & S2 for different bias conditions of the antenna gates at a temperature of 50 K. (c) Measured and (d) simulated results. Reprinted from [244], with the permission of AIP Publishing.

metal contacts or gates and electrostatic biasing facilitates the formation of thermocouples in which photogenerated hot electrons result in a photovoltage due to the photo-thermoelectric effect [244, 249]. However, the thermocouples at graphene metal interfaces are subpar due to electro-cooling [244]. Over time, the significance of the photo-thermoelectric effect became apparent and has since dominated research interests.

Graphene-based detectors now cover a wide variety of frequency ranges: microwave [110, 244, 250, 251], THz [110-112, 242, 243, 250, 252, 253], IR [242, 243, 248, 249, 251, 254, 255], and visible spectrum [242, 247, 254]. There are examples even all the way into the UV frequency range [251]. Depending on the detector response time, even single photons can be detected [251]. Bolometric and antenna-coupled GFET-based detectors are mainly found in practice within the microwave and THz frequency ranges [110-112, 242-244, 250-253].

3.4.1 Bolometers

EM detectors are devices in which the incident field energy is absorbed. Calorimeters are EM detectors in which the absorption results in a temperature increase that is subsequently read out. Bolometers, in general, use the same basic working principle and are employed specifically to measure the power of incident EM fields.

Skobin et al. [244] designed a bolometer based on the thermoelectric effect in graphene. Exfoliated graphene was transferred onto a Parylene-N/SiO_2/Si substrate, and two metal contacts were added to measure the photo-generated voltage. A log-periodic antenna was used to couple incident EM fields to the graphene via two separate gates, as illustrated in figure 37(a). Parylene was used as a dielectric between the graphene and the antenna gates. These two gates were further utilized to induce a p-n junction in the graphene by applying two different voltages to the two antenna arms. The EM fields were generated with a Gunn source at a frequency of 94 GHz and a 30 mW power level. A $\sim$1 µW field power was expected to reach the device. Considering the expected received power level, a photoresponsivity of $\sim 700\ \mathrm{V\,W^{-1}}$ and a noise equivalent power (NEP) of $\sim 200\ \mathrm{pW\,Hz^{-1/2}}$ was determined at an operating temperature of 50 K. The photogenerated signal showed minimal variation, $\sim$600 µV, within the temperature range of $4 - 100$ K, but it was significantly lower at room temperature, i.e., $\sim$10 µV. Therefore, it had to be operated at cryogenic temperatures. Furthermore, the bias voltage of the antenna showed a direct effect on the photo-generated voltage. On the other hand, almost no voltage was measured when there was no bias applied as a consequence of the equivalent Seebeck coefficients in the graphene. It was noted that the impedance mismatch between the antenna and the graphene led to high power losses. It was suggested that the coupling, and with it, the responsitivity could have been significantly improved if better impedance matching had been achieved.

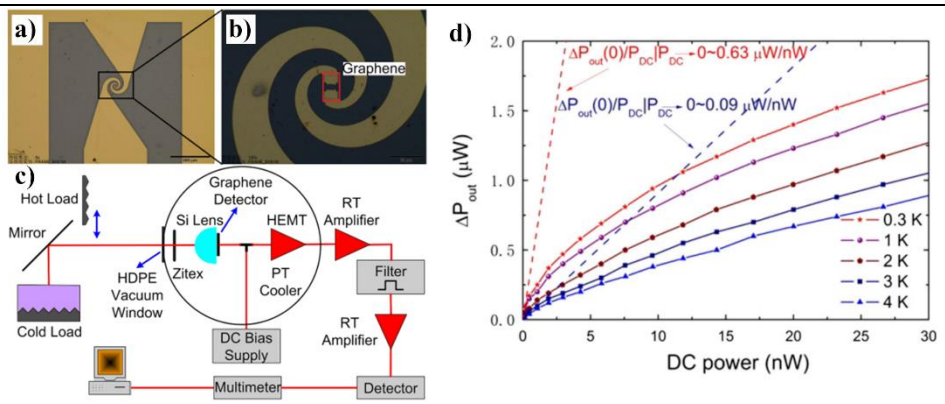

Figure 38. Graphene-based hot-electron bolometer. (a) Image of fabricated hot-electron bolometer, (b) magnification of graphene structure, and (c) schematic setup for the Johnson noise measurement of the hot-electron bolometer. (d) Measured dependence of noise power variation on dc power at different bath temperatures. Reprinted by permission from [252]. Copyright 2018 Springer Nature.

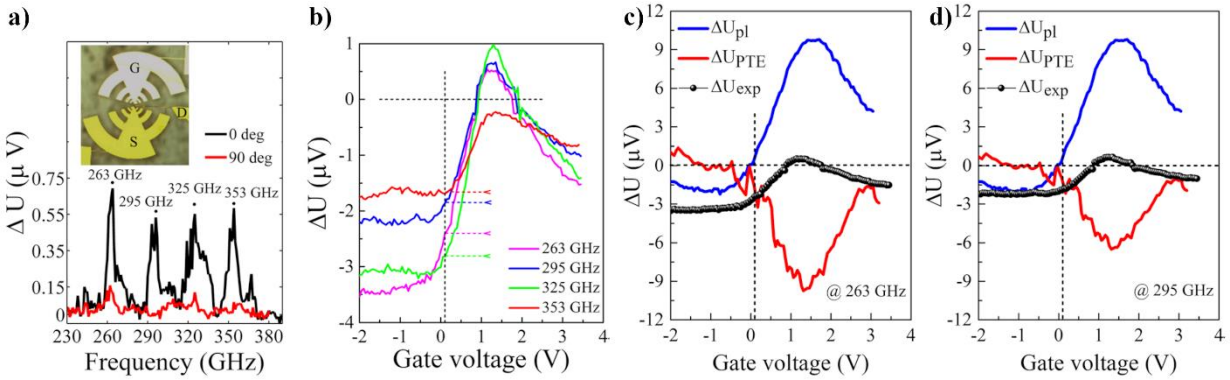

Figure 39. Photo-voltage measurement using a graphene field-effect transistor-based detector of THz fields. (a) Frequency dependence for polarizations of 0 ° and 90 ° relative to antenna axis, at $V_g = 1.2$ V and $V_{sd} = 0$ V. (b) Gate voltage dependence for a variety of frequencies, at $V_{sd} = 0$ V and 0 ° polarization. (c, d) Plasmonic (blue) and thermoelectric (red) photo-voltages analytically extracted from the measured values (black) at (c) 263 GHz, and (d) at 295 GHz, for $V_{sd} = 0$ V and 0 ° polarization. Reprinted from [110], with the permission of AIP Publishing.

Miao et al. [252] designed a hot-electron bolometer (HEB) with EG grown on 4H-SiC substrate. The graphene was integrated with a microbridge and directly connected to a log-spiral antenna that covered the frequency range from 0.1 to 1.4 THz. An elliptical Si lens was attached to the HEB. The device was mounted to a cooler that operated at bath temperatures in the range of $0.3 - 10$ K. Johnson Noise Thermometry was employed to read out the response of the detector by measuring the noise emission of the incident EM field generated from blackbody loads. This system is detailed in figure 38. Measurement of the noise power showed an increase with decreasing temperatures. The NEP was estimated to be $5.6\,\mathrm{nW\,Hz^{-1/2}}$ at 3 K. The high coupling efficiency of the HEB within the desired frequency range was determined with a fast Fourier transform (FFT) of the noise signal.

3.4.2 GFET based THz Detectors

GFET-based THz detectors exhibit different photocurrent generation mechanisms in comparison to thermal detectors/bolometers. They consist of a GFET that is mainly based on EG and a metallic antenna. Their antennas couple the incident EM fields onto the GFET. Their designs have a significant impact on the frequency range of the detectors. Consequently, they often employ bowtie antenna designs, which, as noted previously, have wideband characteristics. One of their main advantages is that they can be operated at room instead of cryogenic temperatures.

Bianco et al. [110] introduced a THz detector that consists of a log-periodic circular-toothed antenna-coupled GFET, as shown in figure 39(a). The GFET was based on EG grown on a SiC substrate (semi-insulating, 4H-SiC(0001)) via thermal sublimation. Illuminating the detector with EM fields within the 230 GHz to 375 GHz frequency range and that provided received power in the range $0.5 - 1$ mW, four distinct modes were measured as the frequency was varied.

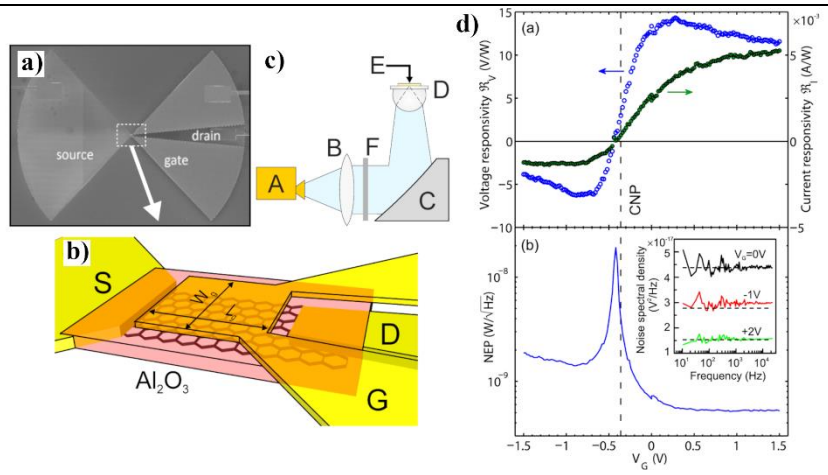

Figure 40. Chemical vapor deposited graphene field-effect transistor-based THz detector. (a) SEM picture of the device. (b) Schematic of the device. (c) Measurement setup. A: THz source, B: lens, C: paraboloid mirror, D: hyper-hemispherical silicon lens, E detector, F: power meter. (d) Measured voltage and current photoresponsitivity (top) and noise equivalent power (bottom). Reprinted with permission from [111]. Copyright 2014 American Chemical Society.

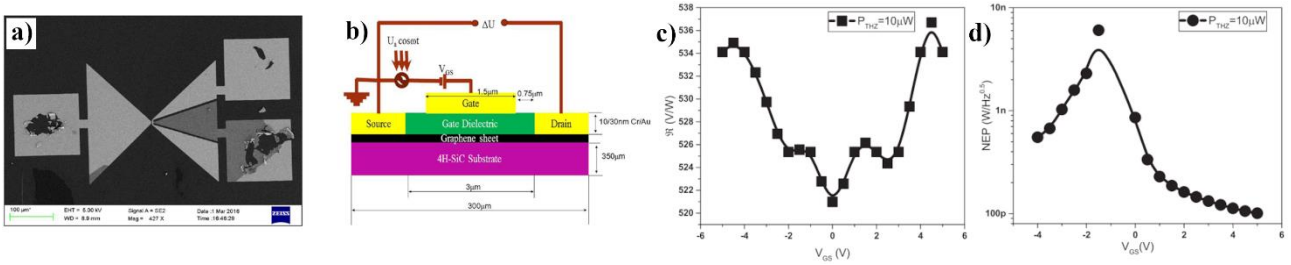

Figure 41. Epitaxial graphene field-effect transistor on SiC THz detector coupled to split bowtie antenna. (a) SEM image of the fabricated detector. (b) Schematic design and dimensions of the graphene field-effect transistor including incident THz fields $\sim Ua\cos(\omega t)$ and the photoresponse voltage ΔU. (c, d) Dependence of photo responsitivity (c) and noise equivalent power (d) on gate biasing under constant incident THz power. [112] © 2018, CC BY 4.0. To view a copy of this license, visit http://creativecommons.org/licenses/by/4.0/

It is important to note that the detector operation was sensitive to the polarization of the incident EM fields with respect to the main axis of the antenna. The configuration is shown in figure 39(a). There were two independent detection mechanisms: rectification of over-damped plasma waves (Dyakonov-Shur) and graphene's thermoelectric effect. The direct analysis of the two mechanisms and the measured induced photo-voltage showed that they competed with each other, as illustrated in figures 39(c,d). The photoresponsivity and NEP were determined to be $\sim 0.25\,\mathrm{V\,W^{-1}}$ and $\sim 80\,\mathrm{nW\,Hz^{-1/2}}$, respectively. However, further improvement was expected by decoupling the EG from SiC to improve its electrical properties.

For comparison, the CVD graphene-based photodetector introduced by Zak et al. in [111] achieved a photoresponsitivity that was two orders of magnitude higher than the EG on SiC-based device in [110]. Their detector design, shown in figure 40(a), consisted of a split bow-tie antenna coupled to a GFET made of CVD SLG transferred onto Si/SiO_2 substrates. It operated at a frequency of 0.6 THz. The photoresponsivity and NEP were determined to be $> 14\,\mathrm{V\,W^{-1}}$ and $\sim 515\,\mathrm{pW\,Hz^{-1/2}}$, respectively, when the incident EM power was 29 μW, as shown in figure 40(b). A significant improvement over the EG on SiC device introduced above was obtained.

A more recent study conducted by Murali et al. [112] analyzed the primary mechanism to improve the sensitivity of the GFET-based THz detectors. They used a split bow-tie antenna coupled to a GFET based on monolayer EG grown on a SiC substrate (semi-insulating, 4H-SiC(0001)). High resistance contacts to the source and drain of the GFET were used deliberately to study the effect of the THz energy coupled to the GFET on the detector's sensitivity. It was demonstrated that the THz coupling onto the channel and the channel control of the GFET was more important than the initial conductivity of the channel and the aforementioned contact resistances. Furthermore, a new approach for calculating the antenna coupling factor was introduced. The designed detector operated at 0.8 THz and achieved a photoresponsivity and NEP of $> 535\,\mathrm{V\,W^{-1}}$ and $< 100\,\mathrm{pW\,Hz^{-1/2}}$, respectively,

Table 5. Comparison of photodetector implementations

Technology	Design	Frequency [GHz]	Photoresponsivity [$\mathrm{V\,W^{-1}}$]	NEP [$\mathrm{pW\,Hz^{-1/2}}$]	Ref.
Exfoliated graphene on Parylene-N/SiO_2/Si substrate	Cryogenic bolometer based on log-periodic antenna	94	$\sim$700	$\sim$200	[244]
EG grown on 4H-SiC substrate	Cryogenic HEB with Johnson Noise Thermometry	100 − 1400	-	5 600	[252]
EG grown on semi-insulating, 4H-SiC(0001)	Log-periodic circular-toothed antenna-coupled GFET	230 − 375	0.25	80 000	[110]
EG grown on semi-insulating, 4H-SiC(0001)	Split bow-tie antenna coupled to a GFET	800	$>$ 535	$<$ 100	[112]
CVD SLG on	Split bow-tie antenna coupled to a GFET	600	14	515	[111]
Exfoliated bilayer graphene on SiO_2/Si	Log-periodic circular-toothed antenna coupled GFET	290 − 380	$\sim$1.2	$\sim$2 000	[253]
TSMC 0.18 μm SiO_2/Si process	Circular antenna coupled to nMOS detector	270 − 320	1 286.6	210	[258]
130 nm Si CMOS process	Bowtie antenna coupled to nMOS rectifying element	270 − 1 050	5 000	$<$ 10	[259]
Lithium tantalate Crystal on Si	Detector array with pixel readout circuit	2 520	8 600	1 500	[256]

for an incident EM field that delivered power levels from ~ 1 to 10 μW. Figures 41(c,d) illustrate how both the responsitivity and NEP were sensitive to changes in the gate bias.

Graphene-based EM field detectors are most commonly studied in the THz frequency range. They offer wideband detection that is associated with the wideband characteristics of the metallic antennas used for the coupling of the EM fields into them. Moreover, they offer a great alternative to common pyroelectric [256], micro-bolometer [257], and silicon CMOS detectors [258-260]. Graphene-based detectors have been demonstrated to cover a wide frequency spectrum and are easy to fabricate due to their planar design. The latter is important to compete with alternative designs that can already be fabricated using standard Si CMOS processes, e.g., using the Taiwan Semiconductor Manufacturing Company (TSMC) 0.18 μm process [258].

The main figures-of-merit (FOMs) for designing detectors are photoresponsitivity, NEP, and response time. While graphene-based detectors in the microwave and THz ranges already offer high photoresponsitivities of $\sim$700 $\mathrm{V\,W^{-1}}$ and NEP as little as 100 $\mathrm{pW\,Hz^{-1/2}}$, which are comparable to commercially available room temperature THz detectors [253], these FOMs are still not as attractive as systems based on alternative materials. Their FOMs are at least one order of magnitude better with photoresponsitivities of up to 8 600 $\mathrm{V\,W^{-1}}$ [256] and a NEP as little as 10 $\mathrm{pW\,Hz^{-1/2}}$ [259], see table 5. Nevertheless, many designs still lack an analysis of their response times, which is an important parameter for continuous readout in spectroscopy and imaging applications. Further improvements in the quality of graphene and decoupling it from the substrate to reduce losses are expected to improve the performance of the devices.

4. Conclusions and Prospects

In recent years, graphene has attracted significant interest for its potential use for generating, manipulating, and detecting EM fields, in particular from microwave to THz frequencies. The possibility for a dynamic tunability of graphene's electrical properties within a fabricated device is one key reason for this considerable interest. While much research around graphene devices is based on numerical and analytical simulation, particularly in the THz range, some devices such as antennas, absorbers, and detectors have been experimentally demonstrated and characterized.

Both the epitaxial growth of graphene on SiC and CVD graphene are promising candidates for integrated graphene devices in the microwave and THz frequency ranges. They offer the possibility of large-area synthesis but have distinct advantages and disadvantages. CVD graphene is the most commonly used type of graphene for both modeling and experimental validation due to its availability and low cost. Monolayer graphene with a low defect count can be grown and transferred onto a wide range of substrates. Several layers can be turbostratically stacked to achieve the desired layer count. However, the transfer process is relatively complex, introduces defects to the graphene, and is limited to planar applications. Epitaxially grown graphene on SiC wafers via thermal decomposition suffers from the requirement of UHV and extremely high temperatures. Techniques to ease the requirements for the high temperature and vacuum have been developed. SiC substrates are also costly and only available in limited sizes. EG on SiC/Si substrates, on the other hand, is

compatible with current silicon technologies and offers a versatile platform. Three-dimensional graphene-coated structures can be created by pre-structuring the SiC. Note that overall the design of electronic or EM devices with epitaxial graphene needs to take into account the silicon carbide properties. In particular, they need to be well understood in the proximity of the Reststrahlen band of SiC owing to the near-total reflection of EM waves and the surface plasmon-phonon coupling.

Graphene flake-based inks form thick graphitic films that possess metal-like conductivities and are heavily investigated in the microwave range. Various techniques, such as rolling compression, annealing, and forgoing isolating additives, such as binders, are employed to improve their electrical and mechanical properties. These include, but are not limited to, their conductivity, flexibility, and robustness.

Overall, it is essential to note that the electrical and mechanical properties of neither CVD graphene, EG grown on SiC, nor graphene inks, can compare to those of ideal graphene. These are only demonstrated for high-quality and free-standing graphene samples. The quality of graphene itself is determined by its grain size, number of defects, intrinsic doping, layer count, etc. In addition, the quality and type of the integrated graphene interfaces can sometimes play even a larger role in the performance of graphene devices.

The investigation of graphene devices heavily relies on full-wave simulation methods as graphene can easily be modeled as a surface impedance. Equivalent circuit models are commonly employed to reduce the computational burden and have demonstrated good agreement with simulation results. Nevertheless, researchers must adopt a conservative model of graphene that represents realistic samples.

Within graphene's conductivity model, its electrical properties can be tuned by changing its chemical potential. Again, conservative values for the range of chemical potentials must be chosen when modeling graphene devices. They must be physically achievable or have already been demonstrated experimentally.

The main focus of reconfigurable devices lies in the electrostatic biasing of graphene using a capacitive gate. However, electrostatic biasing can also be achieved using planar side gating, a solid polymer electrolyte, or ion gel. Alternatively, optical pumping and chemical doping can be used for tuning graphene's properties but are less often considered. New biasing architectures need to be developed and implemented to make use of graphene's dynamic tunability. However, many models of graphene-based devices do not consider biasing architectures altogether, although it is essential for manufacturability and potential experimental validation.

The dynamic tunability of the electrical properties of graphene is insignificant for practical antenna devices in the microwave range because graphene behaves as a variable resistor. Instead, the focus lies in designing flexible antennas, using graphene ink-based graphitic films on a wide range of materials, or with transparent antennas, using CVD graphene. While graphene ink leads to thick layers and has demonstrated metal-like sheet resistances, few-layer epitaxially grown graphene generally possesses a high surface impedance. It is thus dominated by losses in the microwave range. Depositing numerous layers of CVD graphene and the subsequent doping of them has significantly decreased the sheet resistance, yet the radiation efficiencies still significantly lag behind metallic implementations. However, experimental work on microwave graphene and graphitic film-based antennas has demonstrated their usability for flexible, transparent, and low-cost implementations in wearable, sensing, or communication applications.

The THz frequency range is the primary research area for graphene antenna applications. The support of SPP's at those frequencies allows for the miniaturization of antennas made of graphene, in contrast to metallic ones. Simulations confirm a size advantage of up to 20×. Further, the tunability allows for radiation pattern reconfiguration and resonance frequency tuning, paving the way for wireless communication at the nanoscale. THz graphene antennas can be easily matched to photomixers due to their high input impedance. However, because photomixers already possess low efficiencies, the total efficiency is still too low for practical THz applications.

Several graphene traveling-wave antennas, such as Yagi-Uda and leaky wave antennas, have been investigated. Simulations of graphene-based Yagi-Uda antennas have shown how graphene's dynamic tunability can be used to reconfigure their radiation patterns. In leaky wave antennas, the dynamic tunability of graphene's surface impedance enables dynamic beam scanning at fixed frequencies while maintaining their frequency scanning capabilities. However, in both applications, the directivity levels are yet too low when compared to non-graphene implementations, and the obtained reconfigurability is limited.

Metasurface devices, such as reflectarrays and transmitarrays, can easily be fabricated - with a planar design. Experimental studies have demonstrated dynamic reconfigurability of the radiation pattern and polarization utilizing graphene's tunability. Graphene's role in THz antenna applications is quite versatile as it can be used as the main radiating body, as directors, switches, perturbations, and more. However, many research efforts still lack adequate efficiency analysis, with high efficiencies being essential in the THz frequency range.

Simulations of graphene absorbers often demonstrate the tunability and enhancement of absorption, some even promising total absorption and the localization of EM fields. The tunability, however limited, and absorption enhancement have been experimentally demonstrated in the THz range, while near-total absorption and tunability have been

experimentally demonstrated in the microwave range. Furthermore, researchers suggest using graphene-metal hybrid absorbers, including non-graphene tunable elements, for simultaneous frequency and absorption modulation.

THz-detection is a prevalent research area, and many graphene-based detectors have been demonstrated. The main focus lies on detectors made of GFETs coupled to variants of metallic bowtie antennas for broadband operation. Graphene features several detection mechanisms. The performance of graphene detectors has significantly improved in recent years, and they already offer photoresponsitivities and NEPs comparable to commercially available detectors. Nonetheless, considering those FOMs, they still lack behind comparable semiconductor implementations. However, the gap is quickly shrinking.

Dynamic beamforming applications generally require a wide tunability range. The operation of graphene in the SPP region generally results in improved tunability but lower efficiencies. Therefore, a trade-off needs to be made depending on the application. Future work may explore the possibility of operating graphene beamforming devices outside of the SPP region to increase their efficiency at the cost of reconfigurability.

A large part of the published THz graphene devices are only modeled and have not been physically realized and characterized. Graphene-metal contacts have previously shown to result in high contact resistances. They are commonly omitted in simulations; however, they could significantly impact the device's performance, particularly in the THz region. There remains a strong need to demonstrate the behavior of graphene devices experimentally and connect it to the properties of the chosen graphene. The available experimental results, particularly in the THz region, demonstrate a general trend that confirms several attractive enhancements of the performance characteristics of graphene devices, i.e., their beam steering, tuning, and absorption capabilities. However, exact matching to simulation results is rarely achieved, and the achieved tuning range is generally lower than expected.

Graphene synthesis techniques have significantly improved in recent years. Yet, much work is still necessary to improve graphene's electrical properties, homogeneity, cost, and consistency for their implementation in industrial processes. Further advancements in graphene synthesis, device designs, and biasing architectures are expected in the coming years. With them, an improvement of the efficiency, range of tunability, and performance of graphene-based devices in the microwave and THz frequency ranges can be anticipated.

5. Funding

We gratefully acknowledge support from the Australian Research Council through the Centre of Excellence in Transformative Meta-Optical Systems (TMOS) CE200100010.

References

[1] Novoselov K S, Geim A K, Morozov S V, Jiang D, Zhang Y, Dubonos S V, Grigorieva I V and Firsov A A 2004 Electric field effect in atomically thin carbon films *Science* **306** 666-9

[2] Neto A C, Guinea F and Peres N M 2006 Drawing conclusions from graphene *Phys. World* **19** 33-7

[3] Castro Neto A H, Guinea F, Peres N M R, Novoselov K S and Geim A K 2009 The electronic properties of graphene *Rev. Mod. Phys.* **81** 109-62

[4] Kauling A P, Seefeldt A T, Pisoni D P, Pradeep R C, Bentini R, Oliveira R V B, Novoselov K S and Castro Neto A H 2018 The worldwide graphene flake production *Adv. Mater.* **30** 1803784

[5] Wallace P R 1947 The band theory of graphite *Phys. Rev.* **71** 622-34

[6] Chen J H, Jang C, Xiao S, Ishigami M and Fuhrer M S 2008 Intrinsic and extrinsic performance limits of graphene devices on SiO2 *Nat. Nanotechnol.* **3** 206-9

[7] Dorgan V E, Bae M-H and Pop E 2010 Mobility and saturation velocity in graphene on SiO2 *Appl. Phys. Lett.* **97** 082112

[8] Wu Y, Jenkins K A, Valdes-Garcia A, Farmer D B, Zhu Y, Bol A A, Dimitrakopoulos C, Zhu W, Xia F, Avouris P and Lin Y M 2012 State-of-the-art graphene high-frequency electronics *Nano Lett.* **12** 3062-7

[9] Kusmartsev F V, Wu W M, Pierpoint M P and Yung K C 2015 *Applied Spectroscopy and the Science of Nanomaterials*, ed P Misra (Singapore: Springer Singapore) pp 191-221

[10] Geim A K and Novoselov K S 2007 The rise of graphene *Nat. Mater.* **6** 183-91

[11] Hanson G W 2008 Dyadic Green's functions for an anisotropic, non-local model of biased graphene *IEEE Trans. Antennas Propag.* **56** 747-57

[12] Gusynin V P and Sharapov S G 2005 Unconventional integer quantum Hall effect in graphene *Phys. Rev. Lett.* **95** 146801

[13] Gusynin V P and Sharapov S G 2006 Transport of Dirac quasiparticles in graphene: Hall and optical conductivities *Phys. Rev. B* **73** 245411

[14] Falkovsky L A and Varlamov A A 2007 Space-time dispersion of graphene conductivity *Eur. Phys. J. B* **56** 281-4

[15] Gusynin V P, Sharapov S G and Carbotte J P 2007 Magneto-optical conductivity in graphene *J. Phys. Condens. Matter* **19** 026222

[16] Hanson G W 2008 Dyadic Green's functions and guided surface waves for a surface conductivity model of graphene *J. Appl. Phys.* **103** 064302

[17] Dash S and Patnaik A 2018 Performance of graphene plasmonic antenna in comparison with their

counterparts for low-terahertz applications *Plasmonics* **13** 2353-60

[18] Masyukov M, Vozianova A, Grebenchukov A, Gubaidullina K, Zaitsev A and Khodzitsky M 2020 Optically tunable terahertz chiral metasurface based on multi-layered graphene *Sci. Rep.* **10** 3157

[19] Ryzhii V, Ryzhii M and Otsuji T 2007 Negative dynamic conductivity of graphene with optical pumping *J. Appl. Phys.* **101** 083114

[20] Jablan M, Buljan H and Soljačić M 2009 Plasmonics in graphene at infrared frequencies *Phys. Rev. B* **80** 245435

[21] Rouhi N, Capdevila S, Jain D, Zand K, Wang Y Y, Brown E, Jofre L and Burke P 2012 Terahertz graphene optics *Nano Res.* **5** 667-78

[22] Vasic B, Isic G and Gajic R 2013 Localized surface plasmon resonances in graphene ribbon arrays for sensing of dielectric environment at infrared frequencies *J. Appl. Phys.* **113** 13110

[23] de Abajo F J G 2014 Graphene plasmonics: Challenges and opportunities *ACS Photonics* **1** 135-52

[24] Tamagnone M, Gómez-Díaz J S, Mosig J R and Perruisseau-Carrier J 2012 Reconfigurable terahertz plasmonic antenna concept using a graphene stack *Appl. Phys. Lett.* **101** 214102

[25] Fei Z, Rodin A S, Fogler M M, Castro A H, Lau C N, Keilmann F, Basov D N, Andreev G O, Bao W, McLeod A S, Wagner M, Zhang L M, Zhao Z, Thiemens M and Dominguez G 2012 Gate-tuning of graphene plasmons revealed by infrared nano-imaging *Nature* **487** 82-5

[26] Jianing C, Badioli M, Zurutuza Elorza A, Camara N, Garcia De Abajo F J, Hillenbrand R, Koppens F H L, Alonso-Gonzalez P, Thongrattanasiri S, Huth F, Osmond J, Spasenovic M, Centeno A, Pesquera A and Godignon P 2012 Optical nano-imaging of gate-tunable graphene plasmons *Nature* **487** 77-81

[27] Barua A, Hossain M S, Masood K I and Subrina S 2012 Thermal management in 3-D integrated circuits with graphene heat spreaders *Phys. Procedia* **25** 311-6

[28] Balandin A A, Ghosh S, Bao W, Calizo I, Teweldebrhan D, Miao F and Lau C N 2008 Superior thermal conductivity of single-layer graphene *Nano Lett.* **8** 902-7

[29] Lee C, Wei X, Kysar J W and Hone J 2008 Measurement of the elastic properties and intrinsic strength of monolayer graphene *Science* **321** 385-8

[30] Mishra N, Jiao S, Mondal A, Khan Z, Boeckl J J, Gaskill K D, Brock R E, Dauskardt R H and Iacopi F 2018 A graphene platform on silicon for the Internet of Everything. In: *2018 IEEE 2nd Electron Devices Technology and Manufacturing Conference (EDTM)*, (Kobe: IEEE) pp 211-3

[31] Grande M, Bianco G V, Laneve D, Capezzuto P, Petruzzelli V, Scalora M, Prudenzano F, Bruno G and D'Orazio A 2018 Optically transparent wideband CVD graphene-based microwave antennas *Appl. Phys. Lett.* **112** 251103

[32] Novoselov K S, Fal'ko V I, Colombo L, Gellert P R, Schwab M G and Kim K 2012 A roadmap for graphene *Nature* **490** 192-200

[33] Hosseininejad S E, Neshat M, Faraji-Dana R, Lemme M, Haring Bolivar P, Cabellos-Aparicio A, Alarcon E and Abadal S 2018 Reconfigurable THz plasmonic antenna based on few-layer graphene with high radiation efficiency *Nanomaterials* **8** 577

[34] Pradeepkumar A, Amjadipour M, Mishra N, Liu C, Fuhrer M S, Bendavid A, Isa F, Zielinski M, Sirikumara H I, Jayasekara T, Gaskill D K and Iacopi F 2020 P-Type epitaxial graphene on cubic silicon carbide on silicon for integrated silicon technologies *ACS Appl. Nano Mater.* **3** 830-41

[35] Pradeepkumar A, Gaskill D K and Iacopi F 2020 Electronic and transport properties of epitaxial graphene on SiC and 3C-SiC/Si: A review *Appl. Sci.* **10** 4350

[36] Li X, Cai W, An J, Kim S, Nah J, Yang D, Piner R, Velamakanni A, Jung I, Tutuc E, Banerjee S K, Colombo L and Ruoff R S 2009 Large-area synthesis of high-quality and uniform graphene films on copper foils *Science* **324** 1312-4

[37] Kobayashi T, Bando M, Kimura N, Shimizu K, Kadono K, Umezu N, Miyahara K, Hayazaki S, Nagai S, Mizuguchi Y, Murakami Y and Hobara D 2013 Production of a 100-m-long high-quality graphene transparent conductive film by roll-to-roll chemical vapor deposition and transfer process *Appl. Phys. Lett.* **102** 023112

[38] Xu X, Zhang Z, Dong J, Yi D, Niu J, Wu M, Lin L, Yin R, Li M, Zhou J, Wang S, Sun J, Duan X, Gao P, Jiang Y, Wu X, Peng H, Ruoff R S, Liu Z, Yu D, Wang E, Ding F and Liu K 2017 Ultrafast epitaxial growth of metre-sized single-crystal graphene on industrial Cu foil *Sci. Bull.* **62** 1074-80

[39] Forbeaux I, Themlin J M and Debever J M 1998 Heteroepitaxial graphite on 6H−SiC(0001): Interface formation through conduction-band electronic structure *Phys. Rev. B* **58** 16396-406

[40] Berger C, Song Z, Li T, Li X, Ogbazghi A Y, Feng R, Dai Z, Marchenkov A N, Conrad E H, First P N and de Heer W A 2004 Ultrathin epitaxial graphite: 2D electron gas properties and a route toward graphene-based nanoelectronics *J. Phys. Chem. B* **108** 19912-6

[41] Mishra N, Boeckl J J, Tadich A, Jones R T, Pigram P J, Edmonds M, Fuhrer M S, Nichols B M and Iacopi F 2017 Solid source growth of graphene with Ni–Cu catalysts: Towards high qualityin situgraphene on silicon *J. Phys. D* **50** 095302

[42] Juang Z-Y, Wu C-Y, Lo C-W, Chen W-Y, Huang C-F, Hwang J-C, Chen F-R, Leou K-C and Tsai C-H 2009 Synthesis of graphene on silicon carbide substrates at low temperature *Carbon* **47** 2026-31

[43] Cunning B V, Ahmed M, Mishra N, Kermany A R, Wood B and Iacopi F 2014 Graphitized silicon carbide microbeams: wafer-level, self-aligned graphene on silicon wafers *Nanotechnology* **25** 325301

[44] Wang L, Dimitrijev S, Han J, Iacopi A, Hold L, Tanner P and Harrison H B 2011 Growth of 3C–SiC on 150-mm Si(100) substrates by alternating supply epitaxy at 1000 °C *Thin Solid Films* **519** 6443-6

[45] Aristov V Y, Urbanik G, Kummer K, Vyalikh D V, Molodtsova O V, Preobrajenski A B, Zakharov A A, Hess C, Hanke T, Buchner B, Vobornik I, Fujii J, Panaccione G, Ossipyan Y A and Knupfer M 2010 Graphene synthesis on cubic SiC/Si wafers. perspectives for mass production of graphene-based electronic devices *Nano Lett.* **10** 992-5

[46] Suemitsu M and Fukidome H 2010 Epitaxial graphene on silicon substrates *J. Phys. D* **43** 374012

[47] Fukidome H, Kinoshita T, Otsuji T, Suemitsu M, Kawai Y, Handa H, Hibino H, Miyashita H, Kotsugi M, Ohkochi T, Jung M-H and Suemitsu T 2013 Site-selective epitaxy of graphene on Si wafers *Proc. IEEE* **101** 1557-66

[48] Gupta B, Notarianni M, Mishra N, Shafiei M, Iacopi F and Motta N 2014 Evolution of epitaxial graphene layers on 3C SiC/Si (111) as a function of annealing temperature in UHV *Carbon* **68** 563-72

[49] Suemitsu M, Miyamoto Y, Handa H and Konno A 2009 Graphene formation on a 3C-SiC(111) thin film grown on Si(110) substrate *E-J. Surf. Sci. Nanotechnol.* **7** 311-3

[50] Iacopi F, Mishra N, Cunning B V, Goding D, Dimitrijev S, Brock R, Dauskardt R H, Wood B and Boeckl J 2015 A catalytic alloy approach for graphene on epitaxial SiC on silicon wafers *J. Mater. Res.* **30** 609-16

[51] Moon J S, Curtis D, Hu M, Wong D, McGuire C, Campbell P M, Jernigan G, Tedesco J L, VanMil B, Myers-Ward R, Eddy C and Gaskill D K 2009 Epitaxial-graphene RF field-effect transistors on Si-face 6H-SiC substrates *IEEE Electron Device Lett.* **30** 650-2

[52] Hernandez Y, Nicolosi V, Lotya M, Blighe F M, Sun Z, De S, McGovern I T, Holland B, Byrne M, Gun'Ko Y K, Boland J J, Niraj P, Duesberg G, Krishnamurthy S, Goodhue R, Hutchison J, Scardaci V, Ferrari A C and Coleman J N 2008 High-yield production of graphene by liquid-phase exfoliation of graphite *Nat. Nanotechnol.* **3** 563-8

[53] Jiao L, Zhang L, Wang X, Diankov G and Dai H 2009 Narrow graphene nanoribbons from carbon nanotubes *Nature* **458** 877-80

[54] Huang X, Leng T, Zhu M, Zhang X, Chen J, Chang K, Aqeeli M, Geim A K, Novoselov K S and Hu Z 2015 Highly flexible and conductive printed graphene for wireless wearable communications applications *Sci. Rep.* **5** 18298

[55] Huang X, Leng T, Zhang X, Chen J C, Chang K H, Geim A K, Novoselov K S and Hu Z 2015 Binder-free highly conductive graphene laminate for low cost printed radio frequency applications *Appl. Phys. Lett.* **106** 203105

[56] Pan K, Fan Y, Leng T, Li J, Xin Z, Zhang J, Hao L, Gallop J, Novoselov K S and Hu Z 2018 Sustainable production of highly conductive multilayer graphene ink for wireless connectivity and IoT applications *Nat. Commun.* **9** 5197

[57] Lee H-H, Chou K-S and Huang K-C 2005 Inkjet printing of nanosized silver colloids *Nanotechnology* **16** 2436-41

[58] Cochrane C, Koncar V, Lewandowski M and Dufour C 2007 Design and development of a flexible strain sensor for textile structures Based on a conductive polymer composite *Sensors* **7** 473-92

[59] Song R, Liu C, Zhang J, Liu C, He D and Wu Z 2017 Flexible graphene based films for microstrip array antennas. In: *2017 Sixth Asia-Pacific Conference on Antennas and Propagation (APCAP),* (Xi'an: IEEE) pp 1-3

[60] Sa'don S N H, Kamarudin M R, Ahmad F, Jusoh M and Majid H A 2017 Graphene array antenna for 5G applications *Appl. Phys. A* **123** 1-4

[61] Yuan J, Ma L-P, Pei S, Du J, Su Y, Ren W and Cheng H-M 2013 Tuning the electrical and optical properties of graphene by ozone treatment for patterning monolithic transparent electrodes *ACS Nano* **7** 4233-41

[62] Pang S, Tsao H N, Feng X and Müllen K 2009 Patterned graphene electrodes from solution-processed graphite oxide films for organic field-effect transistors *Adv. Mater.* **21** 3488-91

[63] Prado M C, Jariwala D, Marks T J and Hersam M C 2013 Optimization of graphene dry etching conditions via combined microscopic and spectroscopic analysis *Appl. Phys. Lett.* **102** 193111

[64] Wei T, Bao L, Hauke F and Hirsch A 2020 Recent advances in graphene patterning *ChemPlusChem* **85** 1655-68

[65] Luo W, Cai W, Xiang Y, Wu W, Shi B, Jiang X, Zhang N, Ren M, Zhang X and Xu J 2017 In-plane electrical connectivity and near-field concentration of isolated graphene resonators realized by ion beams *Adv. Mater.* **29** 1701083-n/a

[66] Luo W, Cai W, Wu W, Xiang Y, Ren M, Zhang X and Xu J 2016 Tailorable reflection of surface plasmons in defect engineered graphene *2D Mater.* **3** 045001

[67] Xu X, Shi B, Zhang X, Liu Y, Cai W, Ren M, Jiang X, Rupp R A, Wu Q and Xu J 2018 Laser direct writing of graphene nanostructures beyond the diffraction limit by graphene oxidation *Opt. Express* **26** 20726-34

[68] Bobrinetskiy I I, Emelianov A V, Otero N and Romero P M 2015 Patterned graphene ablation and two-photon functionalization by picosecond laser

pulses in ambient conditions *Appl. Phys. Lett.* **107** 43104

[69] Kim K S, Ji Y J, Nam Y, Kim K H, Singh E, Lee J Y and Yeom G Y 2017 Atomic layer etching of graphene through controlled ion beam for graphene-based electronics *Sci. Rep.* **7** 2462-9

[70] Kosuga S, Suga R, Hashimoto O and Koh S 2017 Graphene-based optically transparent dipole antenna *Appl. Phys. Lett.* **110** 233102

[71] Kosuga S, Suga K, Suga R, Watanabe T, Hashimoto O and Koh S 2018 Radiation characteristics of optically transparent dipole antenna fabricated using CVD monolayer graphene. In: *2018 Asia-Pacific Microwave Conference (APMC)*, (Kyoto: IEEE) pp 168-70

[72] Shi B, Cai W, Zhang X, Xiang Y, Zhan Y, Geng J, Ren M and Xu J 2016 Tunable band-stop filters for graphene plasmons based on periodically modulated graphene *Sci. Rep.* **6** 26796-

[73] Xu X, Wang C, Liu Y, Wang X, Gong N, Zhu Z, Shi B, Ren M, Cai W, Rupp R A, Zhang X and Xu J 2019 A graphene P-N junction induced by single-gate control of dielectric structures *J. Mater. Chem. C* **7** 8796-882

[74] Vakil A and Engheta N 2011 Transformation optics using graphene *Science* **332** 1291-4

[75] Gatte M T, Soh P J, Rahim H A, Ahmad R B and Malek F 2016 The performance improvement of Thz antenna via modeling and characterization of doped graphene *Prog. Electromagn. Res. M* **49** 21-31

[76] Headland D, Monnai Y, Abbott D, Fumeaux C and Withayachumnankul W 2018 Tutorial: Terahertz beamforming, from concepts to realizations *APL Photonics* **3** 051101

[77] Wu B, Tuncer H M, Katsounaros A, Wu W, Cole M T, Ying K, Zhang L, Milne W I and Hao Y 2014 Microwave absorption and radiation from large-area multilayer CVD graphene *Carbon* **77** 814-22

[78] Chen X, Liu X, Li S, Wang W, Wei D, Wu Y and Liu Z 2020 Tunable wideband slot antennas based on printable graphene inks *Nanoscale* **12** 10949-55

[79] Yasir M, Savi P, Bistarelli S, Cataldo A, Bozzi M, Perregrini L and Bellucci S 2017 A planar antenna with voltage-controlled frequency tuning based on few-layer graphene *IEEE Antennas Wirel. Propag. Lett.* **16** 2380-3

[80] Zhang J, Song R, Zhao X, Fang R, Zhang B, Qian W, Zhang J, Liu C and He D 2020 Flexible graphene-assembled film-based antenna for wireless wearable sensor with miniaturized size and high sensitivity *ACS Omega* **5** 12937-43

[81] Faisal S N, Amjadipour M, Izzo K, Singer J A, Bendavid A, Lin C-T and Iacopi F 2021 Non-invasive on-skin sensors for brain machine interfaces with epitaxial graphene *J. Neural Eng.* **18** 066035

[82] Bai Y, Xu T and Zhang X 2020 Graphene-based biosensors for detection of biomarkers *Micromachines* **11** 60

[83] Rodrigo D, Limaj O, Janner D, Etezadi D, García de Abajo F J, Pruneri V and Altug H 2015 Mid-infrared plasmonic biosensing with graphene *Science* **349** 165-8

[84] Liu P, Cai W, Wang L, Zhang X and Xu J 2012 Tunable terahertz optical antennas based on graphene ring structures *Appl. Phys. Lett.* **100** 153111--5

[85] Hai-qiang X, Qin-Xu P, Jun H and Wen-Yan Y 2015 Design of a novel graphene terahertz antenna at 500GHz with reconfigurable radiation pattern. In: *2015 IEEE International Symposium on Antennas and Propagation & USNC/URSI National Radio Science Meeting*, (Vancouver: IEEE) pp 1462-3

[86] Gomez-Diaz J S, Esquius-Morote M and Perruisseau-Carrier J 2013 Plane wave excitation-detection of non-resonant plasmons along finite-width graphene strips *Opt. Express* **21** 24856-72

[87] Balanis C A 2008 *Modern Antenna Handbook* (Oxford: Wiley-Blackwell)

[88] Soleimani H and Oraizi H 2020 A novel 2D leaky wave antenna based on complementary graphene patch cell *J. Phys. D* **53** 255301

[89] Yu N, Genevet P, Kats M A, Aieta F, Tetienne J P, Capasso F and Gaburro Z 2011 Light propagation with phase discontinuities: Generalized laws of reflection and refraction *Science* **334** 333-7

[90] Chang Z, You B, Wu L-S, Tang M, Zhang Y-P and Mao J-F 2016 A reconfigurable graphene reflectarray for generation of vrtex THz waves *IEEE Antennas Wirel. Propag. Lett.* **15** 1537-40

[91] Bao Z, Wang J, Hu Z D, Balmakou A, Khakhomov S, Tang Y and Zhang C 2019 Coordinated multi-band angle insensitive selection absorber based on graphene metamaterials *Opt. Express* **27** 31435-45

[92] Saha S, Shah D, M. Shalaev V and Boltasseva A 2021 Tunable metasurfaces: Controlling light in space and time *Opt. Photonics News* **32** 34-41

[93] Tamagnone M, Capdevila S, Lombardo A, Wu J, Centeno A, Zurutuza A, Ionescu A M, Ferrari A C and Mosig J R 2018 Graphene reflectarray metasurface for terahertz beam steering and phase modulation. (arXiv:1806.02202

[94] Shadrivov I V and Neshev D N 2017 *World Scientific Handbook Of Metamaterials And Plasmonics*, ed E Shamonina (Singapore: World Scientific Publishing) p 387

[95] Debogovic T, Bartolic J and Perruisseau-Carrier J 2014 Dual-polarized partially reflective surface antenna with MEMS-based beamwidth reconfiguration *IEEE Trans. Antennas Propag.* **62** 228-36

[96] Li J, Yu P, Zhang S and Liu N 2020 Electrically-controlled digital metasurface device for light projection displays *Nat. Commun.* **11** 3574-

[97] Li X, Tang S, Ding F, Zhong S, Yang Y, Jiang T and Zhou J 2019 Switchable multifunctional terahertz metasurfaces employing vanadium dioxide *Sci. Rep.* **9** 5454-

[98] Ding F, Yang Y and Bozhevolnyi S I 2019 Dynamic metasurfaces using phase-change chalcogenides *Adv. Opt. Mater.* **7** 1801709

[99] Park J, Jeong B G, Kim S I, Lee D, Kim J, Shin C, Lee C B, Otsuka T, Kyoung J, Kim S, Yang K-Y, Park Y-Y, Lee J, Hwang I, Jang J, Song S H, Brongersma M L, Ha K, Hwang S-W, Choo H and Choi B L 2021 All-solid-state spatial light modulator with independent phase and amplitude control for three-dimensional LiDAR applications *Nat. Nanotechnol.* **16** 69

[100] Rufangura P, Folland T G, Agrawal A, Caldwell J D and Iacopi F 2020 Towards low- loss on-chip nanophotonics with coupled graphene and silicon carbide: a review *J. Phys. Mater.* **3** 32005

[101] Fuscaldo W, Burghignoli P, Baccarelli P and Galli A 2017 Graphene Fabry–Perot cavity leaky-wave antennas: Plasmonic versus nonplasmonic solutions *IEEE Trans. Antennas Propag.* **65** 1651-60

[102] Hähnlein B, Händel B, Pezoldt J, Töpfer H, Granzner R and Schwierz F 2012 Side-gate graphene field-effect transistors with high transconductance *Appl. Phys. Lett.* **101** 93504

[103] Long L, Ying X, Yang Y and Wang L 2019 Tuning the infrared absorption of SiC metasurfaces by electrically gating monolayer graphene with solid polymer electrolyte for dynamic radiative thermal management and sensing applications *ACS Appl. Nano Mater.* **2** 4810-7

[104] Ju L, Geng B, Horng J, Girit C, Martin M, Hao Z, Bechtel H A, Liang X, Zettl A, Shen Y R and Wang F 2011 Graphene plasmonics for tunable terahertz metamaterials *Nat. Nanotechnol.* **6** 630-4

[105] Arezoomandan S, Condori Quispe H, Chanana A, Gopalan P, Banerji S, Nahata A and Sensale-Rodriguez B 2018 Graphene–dielectric integrated terahertz metasurfaces *Semicond. Sci. Technol.* **33** 104007

[106] Hosseininejad S E, Rouhi K, Neshat M, Faraji-Dana R, Cabellos-Aparicio A, Abadal S and Alarcon E 2019 Reprogrammable graphene-based metasurface mirror with adaptive focal point for THz imaging *Sci. Rep.* **9** 2868

[107] Tavakol M R and Khavasi A 2020 Reconfigurable meta-coupler employing hybrid metal-graphene metasurfaces *Sci. Rep.* **10** 7684

[108] Wu B, Tuncer H M, Naeem M, Yang B, Cole M T, Milne W I and Hao Y 2014 Experimental demonstration of a transparent graphene millimetre wave absorber with 28% fractional bandwidth at 140 GHz *Sci. Rep.* **4** 4130

[109] Wang X-C, Zhao W-S, Hu J and Yin W-Y 2015 Reconfigurable terahertz leaky-wave antenna using graphene-based high-impedance surface *IEEE Trans. Nanotechnol.* **14** 62-9

[110] Bianco F, Perenzoni D, Convertino D, De Bonis S L, Spirito D, Perenzoni M, Coletti C, Vitiello M S and Tredicucci A 2015 Terahertz detection by epitaxial-graphene field-effect-transistors on silicon carbide *Appl. Phys. Lett.* **107** 131104

[111] Zak A, Andersson M A, Bauer M, Matukas J, Lisauskas A, Roskos H G and Stake J 2014 Antenna-integrated 0.6 THz FET direct detectors based on CVD graphene *Nano Lett.* **14** 5834-8

[112] G K R M, Deshmukh P, Prabhu S S and Basu P K 2018 Antenna coupled graphene-FET as ultra-sensitive room temperature broadband THz detector *AIP Adv.* **8** 125122--7

[113] Zu H-R, Wu B, Zhang Y-H, Zhao Y-T, Song R-G and He D-P 2020 Circularly polarized wearable antenna with low profile and low specific absorption Rate using highly conductive graphene film *IEEE Antennas Wirel. Propag. Lett.* **19** 2354-8

[114] Goyal R and Vishwakarma D K 2018 Design of a graphene-based patch antenna on glass substrate for high-speed terahertz communications *Microw. Opt. Technol. Lett.* **60** 1594-600

[115] Tripathi S K, Kumar M and Kumar A 2019 Graphene based tunable and wideband terahertz antenna for wireless network communication *Wirel. Netw.* **25** 4371-81

[116] Dragoman M, Muller A A, Dragoman D, Coccetti F and Plana R 2010 Terahertz antenna based on graphene *J. Appl. Phys.* **107** 104313

[117] Luo Y, Zeng Q, Yan X, Wu Y, Lu Q, Zheng C, Hu N, Xie W and Zhang X 2019 Graphene-based multi-beam reconfigurable THz antennas *IEEE Access* **7** 30802-8

[118] Esquius-Morote M, Gomez-Diaz J S and Perruisseau-Carrier J 2014 Sinusoidally modulated graphene leaky-wave antenna for electronic beamscanning at THz *IEEE Trans. Terahertz Sci. Technol.* **4** 116-22

[119] Katsounaros A, Cole M T, Tuncer H M, Milne W I and Hao Y 2013 Near-field characterization of chemical vapor deposition graphene in the microwave regime *Appl. Phys. Lett.* **102** 233104

[120] Huang X, Leng T, Chang K H, Chen J C, Novoselov K S and Hu Z 2016 Graphene radio frequency and microwave passive components for low cost wearable electronics *2D Mater.* **3** 025021

[121] Tung T T, Chen S J, Fumeaux C and Losic D 2016 Scalable realization of conductive graphene films for high-efficiency microwave antennas *J. Mater. Chem. C* **4** 10620-4

[122] Tang D, Wang Q, Wang Z, Liu Q, Zhang B, He D, Wu Z and Mu S 2018 Highly sensitive wearable sensor based on a flexible multi-layer graphene film antenna *Sci. Bull.* **63** 574-9

[123] Wang W, Ma C, Zhang X, Shen J, Hanagata N, Huangfu J and Xu M 2019 High-performance printable 2.4 GHz graphene-based antenna using water-transferring technology *Sci. Technol. Adv. Mater.* **20** 870-5

[124] Dragoman M, Neculoiu D, Bunea A-C, Deligeorgis G, Aldrigo M, Vasilache D, Dinescu A,

Konstantinidis G, Mencarelli D, Pierantoni L and Modreanu M 2015 A tunable microwave slot antenna based on graphene *Appl. Phys. Lett.* **106** 153101

[125] Bunea A, Neculoiu D, Dragoman M, Konstantinidis G and Deligeorgis G 2015 X band tunable slot antenna with graphene patch. In: *2015 European Microwave Conference (EuMC)*, (Paris: IEEE) pp 614-7

[126] Nunez Alvarez C, Cheung R and Thompson J S 2017 Performance analysis of hybrid metalgGraphene frequency reconfigurable antennas in the microwave regime *IEEE Trans. Antennas Propag.* **65** 1558-69

[127] Grande M, Bianco G V, Laneve D, Capezzuto P, Petruzzelli V, Scalora M, Prudenzano F, Bruno G and D'Orazio A 2019 Gain and phase control in a graphene-loaded reconfigurable antenna *Appl. Phys. Lett.* **115** 133103

[128] Wang J, Lu W-B, Liu Z-G, Zhang A-Q and Chen H 2020 Graphene-based microwave antennas with reconfigurable pattern *IEEE Trans. Antennas Propag.* **68** 2504-10

[129] Qasem N and Marhoon H M 2020 Simulation and optimization of a tuneable rectangular microstrip patch antenna based on hybrid metal-graphene and FSS superstrate for fifth-generation applications *Telkomnika* **18** 1719-30

[130] Balanis C A 2015 *Antenna Theory : Analysis and Design* (Hoboken: Wiley)

[131] Guan N, Furuya H, Delaune D and Ito K 2008 Antennas made of transparent conductive films *Prog. Electromagn. Res. Symp.* **4** 116-20

[132] Yao Y, Chen W, Chen X and Yu J 2017 Design of optically transparent antenna with directional radiation patterns *Int. J. Antennas Propag* **2017** 1-7

[133] Hong S, Kim Y and Jung C W 2017 Transparent microstrip patch antennas with multilayer and metal-mesh films *IEEE Antennas Wirel. Propag. Lett.* **16** 772-5

[134] Rani M S A, Rahim S K A, Kamarudin M R, Peter T, Cheung S W and Saad B M 2014 Electromagnetic behaviors of thin film CPW-fed CSRR loaded on UWB transparent antenna *IEEE Antennas Wirel. Propag. Lett.* **13** 1239-42

[135] Clasen G and Langley R 2004 Meshed patch antennas *IEEE Trans. Antennas Propag.* **52** 1412-6

[136] Song Y and Huang C 2021 Research on high-performance antennas based on graphene materials *J. Phys. Conf. Ser* **2138** 12006

[137] Kirtania S G, Elger A W, Hasan M R, Wisniewska A, Sekhar K, Karacolak T and Sekhar P K 2020 Flexible antennas: A review *Micromachines* **11** 847

[138] Hassan A, Ali S, Hassan G, Bae J and Lee C H 2016 Inkjet-printed antenna on thin PET substrate for dual band Wi-Fi communications *Microsyst. Technol.* **23** 3701-9

[139] Zhang Y, Li S, Yang Z Q, Qu X Y and Zong W H 2020 A coplanar waveguide-fed flexible antenna for ultra-wideband applications *Int. J. RF Microw. Comput.-Aided Eng.* **30**

[140] Lin W, Chen S-L, Ziolkowski R W and Guo Y J 2018 Reconfigurable, wideband, low-profile, circularly polarized antenna and array enabled by an artificial magnetic conductor ground *IEEE Trans. Antennas Propag.* **66** 1564-9

[141] Fan C, Wu B, Hu Y, Zhao Y and Su T 2020 Millimeter-wave pattern reconfigurable Vivaldi antenna using tunable resistor based on graphene *IEEE Trans. Antennas Propag.* **68** 4939-43

[142] Kovitz J M, Rajagopalan H and Rahmat-Samii Y 2015 Design and implementation of broadband MEMS RHCP/LHCP reconfigurable arrays using rotated E-shaped patch elements *IEEE Trans. Antennas Propag.* **63** 2497-507

[143] Awan W A, Naqvi S I, Ali W A E, Hussain N, Iqbal A, Tran H H, Alibakhshikenari M and Limiti E 2021 Design and realization of a frequency reconfigurable antenna with wide, dual, and single-band operations for compact sized wireless applications *Electronics* **10** 1321

[144] Cusati T, Fiori G, Gahoi A, Passi V, Lemme M C, Fortunelli A and Iannaccone G 2017 Electrical properties of graphene-metal contacts *Sci. Rep.* **7** 5109

[145] Neumaier D and Zirath H 2015 High frequency graphene transistors: can a beauty become a cash cow? *2D Mater.* **2** 030203

[146] Lyu H, Lu Q, Liu J, Wu X, Zhang J, Li J, Niu J, Yu Z, Wu H and Qian H 2016 Deep-submicron graphene field-effect transistors with state-of-art fmax *Sci. Rep.* **6** 35717

[147] Jiang J, Kang J, Cao W, Xie X, Zhang H, Chu J H, Liu W and Banerjee K 2017 Intercalation doped multilayer-Graphene-nanoribbons for next-generation interconnects *Nano Lett.* **17** 1482-8

[148] Qiaofeng Q, Zidong W, Yuehui J, Pei P, Xin G, Liming R and Yunyi F 2015 Impacts of dimensions, number of layers and contact structures on the loss of graphene-based coplanar waveguides through simulations. In: *2015 IEEE 16th International Conference on Communication Technology (ICCT)*, pp 255-7

[149] Nissiyah G J and Madhan M G 2018 Graphene-based photoconductive antenna structures for directional terahertz emission *Plasmonics* **14** 891-900

[150] Llatser I, Kremers C, Cabellos-Aparicio A, Jornet J M, Alarcón E and Chigrin D N 2012 Graphene-based nano-patch antenna for terahertz radiation *Photonics Nanostructures: Fundam. Appl.* **10** 353-8

[151] Tamagnone M, Gómez-Díaz J S, Mosig J R and Perruisseau-Carrier J 2012 Analysis and design of terahertz antennas based on plasmonic resonant graphene sheets *J. Appl. Phys.* **112** 114915

[152] Zhou T, Cheng Z, Zhang H, Le Berre M, Militaru L and Calmon F 2014 Miniaturized tunable terahertz

antenna based on graphene *Microw. Opt. Technol. Lett.* **56** 1792-4
[153] Anand S, Sriram Kumar D, Wu R J and Chavali M 2014 Graphene nanoribbon based terahertz antenna on polyimide substrate *Optik* **125** 5546-9
[154] Thampy A S, Darak M S and Dhamodharan S K 2015 Analysis of graphene based optically transparent patch antenna for terahertz communications *Physica E Low Dimens. Syst. Nanostruct.* **66** 67-73
[155] Dashti M and Carey J D 2018 Graphene microstrip patch ultrawide band antennas for THz communications *Adv. Funct. Mater.* **28** 1705925
[156] Dash S and Patnaik A 2019 Sub-wavelength graphene planar nanoantenna for THz application *Mater. Today: Proc.* **18** 1336-41
[157] Khan M A K, Shaem T A and Alim M A 2019 Analysis of graphene based miniaturized terahertz patch antennas for single band and dual band operation *Optik* **194** 163012
[158] Zhang B, Zhang J, Liu C, Wu Z and He D 2018 Equivalent resonant circuit modeling of a graphene-based bowtie antenna *Electronics* **7** 285
[159] Dai J, Ruan C, Ding Y and Yan Z 2021 High-power vacuum terahertz photomixer and integrated circuits based on microscale phototubes *Opt. Express* **29** 1918-31
[160] Radwan A H, Amico M D and Gentili G G 2014 Reconfigurable THz Yagi antenna based on hybrid graphene-metal layout. In: *2014 Loughborough Antennas and Propagation Conference (LAPC),* (Loughborough: IEEE) pp 671-5
[161] Wu Y, Qu M, Jiao L, Liu Y and Ghassemlooy Z 2016 Graphene-based Yagi-Uda antenna with reconfigurable radiation patterns *AIP Adv.* **6** 65308-065308-11
[162] Hosseininejad S E, Abadal S, Neshat M, Faraji-Dana R, Lemme M C, Suessmeier C, Bolivar P H, Alarcon E and Cabellos-Aparicio A 2018 MAC-oriented programmable terahertz PHY via graphene-based Yagi-Uda antennas. In: *2018 IEEE Wireless Communications and Networking Conference (WCNC),* (Barcelona: IEEE) pp 1-6
[163] Ahmad I, Ullah S, Ullah S, Habib U, Ahmad S, Ghaffar A, Alibakhshikenari M, Khan S and Limiti E 2021 Design and analysis of a photonic crystal based planar antenna for THz applications *Electronics* **10** 1941
[164] Anand S, Sriram Kumar D, Wu R J and Chavali M 2014 Analysis and design of optically transparent antenna on photonic band gap structures *Optik* **125** 2835-9
[165] Oliner A and Hessel A 1959 Guided waves on sinusoidally-modulated reactance surfaces *IEEE Trans. Antennas Propag.* **7** 201-8
[166] Chu D A, Hon P W C, Itoh T and Williams B S 2016 Feasibility of graphene CRLH metamaterial waveguides and leaky wave antennas *J. Appl. Phys.* **120** 13103
[167] Correas-Serrano D, Gomez-Diaz J S, Sounas D L, Hadad Y, Alvarez-Melcon A and Alu A 2016 Nonreciprocal graphene devices and antennas based on spatiotemporal modulation *IEEE Antennas Wirel. Propag. Lett.* **15** 1529-32
[168] Patel S K, Sorathiya V, Guo T and Argyropoulos C 2018 Graphene-based directive optical leaky wave antenna *Microw. Opt. Technol. Lett.* **61** 153-7
[169] Tianxia Z, Jackson D R, Williams J T and Oliner A A 2005 General formulas for 2-D leaky-wave antennas *IEEE Trans. Antennas Propag.* **53** 3525-33
[170] Pozar D M 2011 *Microwave Engineering* (Hoboken: Wiley)
[171] van Berkel S, Malotaux E S, De Martino C, Spirito M, Cavallo D, Neto A and Llombart N 2020 Wideband double leaky slot lens antennas in CMOS technology at submillimeter wavelengths *IEEE Trans. Terahertz Sci. Technol.* **10** 540-53
[172] Mohsen M K, Isa M S M, Isa A A M, Abdulhameed M K and Attiah M L 2019 Achieving fixed-frequency beam scanning with a microstrip leaky-wave antenna using double-gap capacitor technique *IEEE Antennas Wirel. Propag. Lett.* **18** 1502-6
[173] Chen S-L, Karmokar D K, Qin P-Y, Ziolkowski R W and Guo Y J 2020 Polarization-reconfigurable leaky-wave antenna with continuous beam scanning through broadside *IEEE Trans. Antennas Propag.* **68** 121-33
[174] Lu P, Haddad T, Sievert B, Khani B, Makhlouf S, Dulme S, Estevez J F, Rennings A, Erni D, Pfeiffer U and Stohr A 2021 InP-based THz beam steering leaky-wave antenna *IEEE Trans. Terahertz Sci. Technol.* **11** 218-30
[175] Karl N J, McKinney R W, Monnai Y, Mendis R and Mittleman D M 2015 Frequency-division multiplexing in the terahertz range using a leaky-wave antenna *Nat. Photonics* **9** 717-20
[176] Lu P, Haddad T, Tebart J, Steeg M, Sievert B, Lackmann J, Rennings A and Stöhr A 2021 Mobile THz communications using photonic assisted beam steering leaky-wave antennas *Opt. Express* **29** 21629-38
[177] Zvolensky T, Chicherin D, RÄIsÄNen A V and Simovski C 2011 Leaky-wave antenna based on micro-electromechanical systems-loaded microstrip line *IET Microw. Antennas Propag.* **5** 357-63
[178] Nguyen H V, Parsa A and Caloz C 2010 Power-recycling feedback system for maximization of leaky-wave antennas' radiation efficiency *IEEE Trans. Microwave Theory Tech.* **58** 1641-50
[179] Karacolak T, Thirumalai R V K G, Merrett J N, Koshka Y and Topsakal E 2013 Silicon carbide (SiC) antennas for high-temperature and high-power applications *IEEE Antennas Wirel. Propag. Lett.* **12** 409-12
[180] Saddow S E, Gazziro M, Frewin C L, Thomas S, Araujo Cespedes F and Bernadin E 2016 SiC for

biomedical applications *Mater. Sci. Forum* **858** 1010-4

[181] Han K, Nguyen T K, Park I and Han H 2009 Terahertz Yagi-Uda antenna for high input resistance *J. Infrared Millim. Terahertz Waves* **31** 441-54

[182] Poorgholam-Khanjari S, Zarrabi F B and Jarchi S 2020 Compact and wide-band Quasi Yagi-Uda antenna based on periodic grating ground and coupling method in terahertz regime *Optik* **203** 163990

[183] Torabi Y, Dadashzadeh G, Hadeie M, Oraizi H and Lalbakhsh A 2021 A wide-angle scanning sub-terahertz leaky-wave antenna based on a multilayer dielectric image waveguide *Electronics* **10** 2172

[184] Parshin V, Serov E, Denisov G, Garin B, Denisyuk R, V'Yuginov V, Klevtsov V and Travin N 2017 Silicon carbide for high-power applications at MM and THz ranges *Diam. Relat. Mater.* **80** 1-4

[185] Rufangura P, Khodasevych I, Agrawal A, Bosi M, Folland T G, Caldwell J D and Iacopi F 2021 Enhanced absorption with graphene-coated silicon carbide nanowires for mid-infrared nanophotonics *Nanomaterials* **11** 2339

[186] Berry D, Malech R and Kennedy W 1963 The reflectarray antenna *IEEE Trans. Antennas Propag.* **11** 645-51

[187] Deng L, Zhang Y, Zhu J and Zhang C 2018 Wide-band circularly polarized reflectarray using graphene-based Pancharatnam-Berry phase unit-cells for terahertz communication *Materials* **11** 956

[188] Zhang J, Zhang H, Yang W, Chen K, Wei X, Feng Y, Jin R and Zhu W 2020 Dynamic scattering steering with graphene-based coding metamirror *Adv. Opt. Mater.* **8** 2000683-n/a

[189] Deng L, Wu Y, Zhang C, Hong W, Peng B, Zhu J and Li S 2017 Manipulating of different-polarized reflected waves with graphene-based plasmonic metasurfaces in terahertz regime *Sci. Rep.* **7** 10558

[190] Carrasco E, Tamagnone M and Perruisseau-Carrier J 2013 Tunable graphene reflective cells for THz reflectarrays and generalized law of reflection *Appl. Phys. Lett.* **102** 104103

[191] Carrasco E and Perruisseau-Carrier J 2013 Reflectarray antenna at terahertz using graphene *IEEE Antennas Wirel. Propag. Lett.* **12** 253-6

[192] Chen H, Lu W-B, Liu Z-G and Geng M-Y 2020 Microwave programmable graphene metasurface *ACS Photonics* **7** 1425-35

[193] Chen H, Liu Z, Lu W, Zhang A, Li X and Zhang J 2018 Microwave beam reconfiguration based on graphene ribbon *IEEE Trans. Antennas Propag.* **66** 6049-56

[194] Biswas S R, Gutiérrez C E, Nemilentsau A, Lee I-H, Oh S-H, Avouris P and Low T 2018 Tunable graphene metasurface reflectarray for cloaking, illusion, and focusing *Phys. Rev. Appl.* **9** 034021

[195] Han S, Kim S, Kim S, Low T, Brar V W and Jang M S 2020 Complete complex amplitude modulation with electronically tunable graphene plasmonic metamolecules *ACS Nano* **14** 1166-75

[196] Sun Z, Huang F and Fu Y 2021 Graphene-based active metasurface with more than 330° phase tunability operating at mid-infrared spectrum *Carbon* **173** 512-20

[197] Munk B 2005 *Frequency Selective Surfaces Theory and Design* (New York: Wiley)

[198] Kuznetsov S A, Astafev M A, Beruete M and Navarro-Cía M 2015 Planar holographic metasurfaces for terahertz focusing *Sci. Rep.* **5** 7738-

[199] Hasani H, Tamagnone M, Capdevila S, Moldovan C F, Maoddi P, Ionescu A M, Peixeiro C, Mosig J R, Skrivervik A K and Perruisseau-Carrier J 2016 Tri-band, polarization-independent reflectarray at terahertz frequencies: Design, fabrication, and measurement *IEEE Trans. Terahertz Sci. Technol.* **6** 268-77

[200] Hum S V, Okoniewski M and Davies R J 2005 Realizing an electronically tunable reflectarray using varactor diode-tuned elements *IEEE Microw. Wirel. Compon. Lett.* **15** 422-4

[201] Bayraktar O, Civi O A and Akin T 2012 Beam switching reflectarray monolithically integrated with RF MEMS switches *IEEE Trans. Antennas Propag.* **60** 854-62

[202] Perez-Palomino G, Baine P, Dickie R, Bain M, Encinar J A, Cahill R, Barba M and Toso G 2013 Design and experimental validation of liquid crystal-based reconfigurable reflectarray elements with improved bandwidth in F-band *IEEE Trans. Antennas Propag.* **61** 1704-13

[203] Ma Z, Hanham S M, Albella P, Ng B, Lu H T, Gong Y, Maier S A and Hong M 2016 Terahertz all-dielectric magnetic mirror metasurfaces *ACS Photonics* **3** 1010-8

[204] Dai L, Wang B, Wang M, Yang X, Tan J, Bi S, Xu S, Yang F, Chen Z, Renzo M D, Chae C-B and Hanzo L 2020 Reconfigurable intelligent surface-based wireless communications: antenna design, prototyping, and experimental results *IEEE Access* **8** 45913-23

[205] Huang C, Zappone A, Alexandropoulos G C, Debbah M and Yuen C 2019 Reconfigurable intelligent surfaces for energy efficiency in wireless communication *IEEE Trans. Wirel. Commun.* **18** 4157-70

[206] Xu Y-L, Wei X-C and Li E-P 2015 Three-dimensional tunable frequency selective surface based on vertical graphene micro-ribbons *J. Electromagn. Waves Appl.* **29** 2130-8

[207] AbdollahRamezani S, Arik K, Farajollahi S, Khavasi A and Kavehvash Z 2015 Beam manipulating by gate-tunable graphene-based metasurfaces *Opt. Lett.* **40** 5383-6

[208] Liu Y, Xu X, Yang D, Zhang X, Ren M, Gong N, Cai W, Hassan F, Zhu Z, Drevenšek-Olenik I, Rupp R A and Xu J 2020 Multifunctional and tunable trigate

graphene metamaterial with "Lakes of Wada" topology *Opt. Express* **28** 24772-88
[209] Guo T and Argyropoulos C 2016 Broadband polarizers based on graphene metasurfaces *Opt. Lett.* **41** 5592-5
[210] Menzel C, Rockstuhl C and Lederer F 2010 Advanced Jones calculus for the classification of periodic metamaterials *Phys. Rev. A* **82** 053811
[211] Fan S, Suh W and Joannopoulos J D 2003 Temporal coupled-mode theory for the Fano resonance in optical resonators *J. Opt. Soc. Am. A* **20** 569-72
[212] Neu J, Beigang R and Rahm M 2013 Metamaterial-based gradient index beam steerers for terahertz radiation *Appl. Phys. Lett.* **103** 41109
[213] Liu S, Cheng Q, Xu Q, Wang T Q, Du L L, Luan K, Xu Y H, Bao D, Fu X J, Han J G, Zhang W L and Cui T J 2016 Free-standing metasurfaces for high-efficiency transmitarrays for controlling terahertz waves *Adv. Opt. Mater.* **4** 384-90
[214] Wang M, Xu S, Yang F, Hu N, Xie W and Chen Z 2020 A novel 1-Bit reconfigurable transmitarray antenna using a C-shaped probe-fed patch element with broadened bandwidth and enhanced efficiency *IEEE Access* **8** 120124-33
[215] Hong S K, Kim K Y, Kim T Y, Kim J H, Park S W, Kim J H and Cho B J 2012 Electromagnetic interference shielding effectiveness of monolayer graphene *Nanotechnology* **23** 455704
[216] Balci O, Polat E O, Kakenov N and Kocabas C 2015 Graphene-enabled electrically switchable radar-absorbing surfaces *Nat. Commun.* **6** 6628
[217] Watts C M, Liu X and Padilla W J 2012 Metamaterial electromagnetic wave absorbers *Adv. Mater.* **24** OP98-OP120
[218] Markoš P and Soukoulis C M 2008 *Wave Propagation: From Electrons to Photonic Crystals and Left-Handed Materials* (Princeton: Princeton University Press)
[219] Patel S K, Charola S, Parmar J, Ladumor M, Ngo Q M and Dhasarathan V 2020 Broadband and efficient graphene solar absorber using periodical array of C-shaped metasurface *Opt. Quantum Electron.* **52** 1-19
[220] Raad S H and Atlasbaf Z 2021 Solar cell design using graphene-based hollow nano-pillars *Sci. Rep.* **11** 16169-
[221] Lim E L, Yap C C, Jumali M H H, Teridi M A M and Teh C H 2017 A mini review: can graphene be a novel material for perovskite solar cell applications? *Nanomicro Lett* **10** 1-12
[222] Thakur A K, Sathyamurthy R, Sharshir S W, Kabeel A E, Elkadeem M R, Ma Z, Manokar A M, Arıcı M, Pandey A K and Saidur R 2021 Performance analysis of a modified solar still using reduced graphene oxide coated absorber plate with activated carbon pellet *Sustain. Energy Technol. Assess.* **45** 101046
[223] Wu J, Jia L, Zhang Y, Qu Y, Jia B and Moss D J 2021 Graphene oxide for integrated photonics and flat optics *Adv. Mater.* **33** e2006415-n/a
[224] Patrick R and Cumali S 2017 Graphene-based wideband metamaterial absorber for solar cells application *J. Nanophotonics* **11** 1-9
[225] Barzegar-Parizi S 2018 Realization of wide-angle and wideband absorber using metallic and graphene-based metasurface for mid-infrared and low THz frequency *Opt. Quantum Electron.* **50** 1-12
[226] Zhao B, Zhao J M and Zhang Z M 2014 Enhancement of near-infrared absorption in graphene with metal gratings *Appl. Phys. Lett.* **105** 31905
[227] Balci O, Kakenov N and Kocabas C 2017 Controlling phase of microwaves with active graphene surfaces *Appl. Phys. Lett.* **110** 161102
[228] Zhang J, Wei X, Premaratne M and Zhu W 2019 Experimental demonstration of an electrically tunable broadband coherent perfect absorber based on a graphene-electrolyte-graphene sandwich structure *Photonics Res.* **7** 868-74
[229] Huang C, Song J, Ji C, Yang J and Luo X 2021 Simultaneous control of absorbing frequency and amplitude using graphene capacitor and active frequency-selective surface *IEEE Trans. Antennas Propag.* **69** 1793-8
[230] Zhang J, Wei X, Rukhlenko I D, Chen H-T and Zhu W 2020 Electrically tunable metasurface with independent frequency and amplitude modulations *ACS Photonics* **7** 265-71
[231] Alaee R, Farhat M, Rockstuhl C and Lederer F 2012 A perfect absorber made of a graphene micro-ribbon metamaterial *Opt. Express* **20** 28017-24
[232] Andryieuski A and Lavrinenko A V 2013 Graphene metamaterials based tunable terahertz absorber: effective surface conductivity approach *Opt. Express* **21** 9144-55
[233] Ahmadivand A, Sinha R, Karabiyik M, Vabbina P K, Gerislioglu B, Kaya S and Pala N 2016 Tunable THz wave absorption by graphene-assisted plasmonic metasurfaces based on metallic split ring resonators *J. Nanopart. Res.* **19** 1-14
[234] Ghosh S K, Das S and Bhattacharyya S 2020 Graphene based metasurface with near unity broadband absorption in the terahertz gap *Int. J. RF Microw. Comput.-Aided Eng.* **30** 22436
[235] La Spada L and Vegni L 2016 Metamaterial-based wideband electromagnetic wave absorber *Opt. Express* **24** 5763-72
[236] Lu C, Fu Q, Huang S and Liu J 2004 Polymer electrolyte-gated carbon nanotube field-effect transistor *Nano Lett.* **4** 623-7
[237] Wang L P and Zhang Z M 2011 Phonon-mediated magnetic polaritons in the infrared region *Opt. Express* **19** A126-35
[238] Yariv A 1973 Coupled-mode theory for guided-wave optics *IEEE J. Quantum Electron.* **9** 919-33
[239] Amiri M, Tofigh F, Shariati N, Lipman J and Abolhasan M 2020 Wide-angle metamaterial

absorber with highly insensitive absorption for TE and TM modes *Sci. Rep.* **10** 13638-

[240] Deng G, Hu H, Mo H, Xu J, Yin Z, Lu H, Hu M, Li J and Yang J 2021 Tunable terahertz metamaterial wideband absorber with liquid crystal *Opt. Mater. Express* **11** 4026-35

[241] Ren Z, Cheng L, Hu L, Liu C, Jiang C, Yang S, Ma Z, Zhou C, Wang H, Zhu X, Sun Y and Sheng Z 2020 Photoinduced broad-band tunable terahertz absorber based on a VO2 thin film *ACS Appl. Mater. Interfaces* **12** 48811-9

[242] Yan J, Kim M H, Elle J A, Sushkov A B, Jenkins G S, Milchberg H M, Fuhrer M S and Drew H D 2012 Dual-gated bilayer graphene hot-electron bolometer *Nat. Nanotechnol.* **7** 472-8

[243] Yuan S, Yu R, Ma C, Deng B, Guo Q, Chen X, Li C, Chen C, Watanabe K, Taniguchi T, García de Abajo F J and Xia F 2020 Room temperature graphene mid-infrared bolometer with a broad operational wavelength range *ACS Photonics* **7** 1206-15

[244] Skoblin G, Sun J and Yurgens A 2018 Graphene bolometer with thermoelectric readout and capacitive coupling to an antenna *Appl. Phys. Lett.* **112** 63501

[245] Koppens F H, Mueller T, Avouris P, Ferrari A C, Vitiello M S and Polini M 2014 Photodetectors based on graphene, other two-dimensional materials and hybrid systems *Nat. Nanotechnol.* **9** 780-93

[246] Dyakonov M and Shur M 1996 Detection, mixing, and frequency multiplication of terahertz radiation by two-dimensional electronic fluid *IEEE Trans. Electron Devices* **43** 380-7

[247] Lee E J, Balasubramanian K, Weitz R T, Burghard M and Kern K 2008 Contact and edge effects in graphene devices *Nat. Nanotechnol.* **3** 486-90

[248] Xia F, Mueller T, Lin Y M, Valdes-Garcia A and Avouris P 2009 Ultrafast graphene photodetector *Nat. Nanotechnol.* **4** 839-43

[249] Gabor N M, Song J C, Ma Q, Nair N L, Taychatanapat T, Watanabe K, Taniguchi T, Levitov L S and Jarillo-Herrero P 2011 Hot carrier-assisted intrinsic photoresponse in graphene *Science* **334** 648-52

[250] Bandurin D A, Svintsov D, Gayduchenko I, Xu S G, Principi A, Moskotin M, Tretyakov I, Yagodkin D, Zhukov S, Taniguchi T, Watanabe K, Grigorieva I V, Polini M, Goltsman G N, Geim A K and Fedorov G 2018 Resonant terahertz detection using graphene plasmons *Nat. Commun.* **9** 5392

[251] El Fatimy A, Nath A, Kong B D, Boyd A K, Myers-Ward R L, Daniels K M, Jadidi M M, Murphy T E, Gaskill D K and Barbara P 2018 Ultra-broadband photodetectors based on epitaxial graphene quantum dots *Nanophotonics* **7** 735-40

[252] Miao W, Gao H, Wang Z, Zhang W, Ren Y, Zhou K M, Shi S C, Yu C, He Z Z, Liu Q B and Feng Z H 2018 A graphene-based terahertz hot electron bolometer with Johnson noise readout *J. Low Temp. Phys.* **193** 387-92

[253] Spirito D, Coquillat D, De Bonis S L, Lombardo A, Bruna M, Ferrari A C, Pellegrini V, Tredicucci A, Knap W and Vitiello M S 2014 High performance bilayer-graphene terahertz detectors *Appl. Phys. Lett.* **104** 61111

[254] Cakmakyapan S, Lu P K, Navabi A and Jarrahi M 2018 Gold-patched graphene nano-stripes for high-responsivity and ultrafast photodetection from the visible to infrared regime *Light Sci. Appl.* **7** 20

[255] Walsh E D, Jung W, Lee G H, Efetov D K, Wu B I, Huang K F, Ohki T A, Taniguchi T, Watanabe K, Kim P, Englund D and Fong K C 2021 Josephson junction infrared single-photon detector *Science* **372** 409-12

[256] Li W, Wang J, Gou J, Huang Z and Jiang Y 2015 Fabrication and characterization of linear terahertz detector arrays based on lithium tantalate crystal *J. Infrared Millim. Terahertz Waves* **36** 42-8

[257] Lee A W M, Williams B S, Kumar S, Qing H and Reno J L 2006 Real-time imaging using a 4.3-THz quantum cascade laser and a 320 /spl times/ 240 microbolometer focal-plane array *IEEE Photon. Technol. Lett.* **18** 1415-7

[258] Xu L-J, Tong F-C, Bai X and Li Q 2018 Design of miniaturised on-chip slot antenna for THz detector in CMOS *IET Microw. Antennas Propag.* **12** 1324-31

[259] Schuster F, Coquillat D, Videlier H, Sakowicz M, Teppe F, Dussopt L, Giffard B, Skotnicki T and Knap W 2011 Broadband terahertz imaging with highly sensitive silicon CMOS detectors *Opt. Express* **19** 7827-32

[260] Čibiraitė-Lukenskienė D, Ikamas K, Lisauskas T, Krozer V, Roskos H G and Lisauskas A 2020 Passive detection and imaging of human body radiation using an uncooled field-effect transistor-based THZ detector *Sensors* **20** 1-14